
000 001 *CodeBrain: TOWARDS DECOUPLED INTERPRETABILITY* 002 AND MULTI-SCALE ARCHITECTURE FOR EEG FOUN- 003 DATION MODEL 004

005
006 **Anonymous authors**
007 Paper under double-blind review
008

009 010 ABSTRACT 011

012
013 Electroencephalography (EEG) provides real-time insights into brain activity and
014 supports diverse applications in neuroscience. While EEG foundation models
015 (EFMs) have emerged to address the scalability issues of task-specific models,
016 current approaches still yield clinically uninterpretable and weakly discriminative
017 representations, inefficiently capture global dependencies, and neglect important
018 local neural events. We present *CodeBrain*, a two-stage EFM designed to fill this
019 gap. In the first stage, we introduce the **TFDual-Tokenizer**, which decouples het-
020 erogeneous temporal and frequency EEG signals into discrete tokens, quadratically
021 expanding the representation space to enhance discriminative power and offering
022 domain-specific **representation-level** interpretability by suggesting potential links to
023 neural events and spectral rhythms. In the second stage, we propose the multi-scale
024 **EEGSSM** architecture, which combines structured global convolution with sliding
025 window attention to efficiently capture both sparse long-range and local dependen-
026 cies, reflecting the brain’s small-world topology. Pretrained on the largest public
027 EEG corpus, *CodeBrain* achieves strong generalization across 8 downstream tasks
028 and 10 datasets under distribution shifts, supported by comprehensive ablations,
029 scaling-law analyses, and interpretability evaluations.

030 1 INTRODUCTION 031

032 Electroencephalography (EEG) captures brain activity via scalp electrodes (Niedermeyer & da Silva,
033 2005) and provides high temporal-resolution signals for neuroscience and cognitive research (da Silva,
034 2013). To enable automated analysis, researchers have developed various task-specific models for
035 applications such as sleep staging (Lee et al., 2025; Ma et al., 2025), emotion recognition (Jia et al.,
036 2020a; Liu et al., 2024a), motor imagery (Li et al., 2020; Jia et al., 2020b), and other applications
037 (Guerra et al., 2024; Hu et al., 2024). However, building separate models from scratch for each task
038 is resource-intensive and limits scalability, as shared knowledge across tasks cannot be effectively
039 leveraged. Moreover, variations in channel configurations and input lengths across EEG tasks further
040 hinder knowledge transfer. To tackle these issues, EEG foundation models (EFMs) are developed to
041 learn universal representations for diverse downstream tasks (Zhou et al., 2025).

042 Inspired by masked self-supervised pretraining in natural language processing (Van Den Oord et al.,
043 2017; Devlin et al., 2019), current EFMs commonly adopt patch-wise representation learning: EEG
044 signals are divided into patches, encoded into latent representations, and trained to reconstruct the
045 masked portions. While this approach offers flexibility across varying channel configurations and
046 input lengths by adjusting the patch number and arrangement, direct raw-signal reconstruction (Wang
047 et al., 2024a; 2025) remains challenging due to the inherent noise and variability of EEG. To mitigate
048 this, recent studies have introduced codebook-based tokenization (Jiang et al., 2024; Pradeepkumar
049 et al., 2025), which abstracts away low-level fluctuations and provides a more robust latent space.
050 Despite these advances, existing EFMs still face critical limitations, calling for new architectures.

051 **Failing to Decouple Heterogeneous EEG for Domain-Specific Interpretability.** Recent EFMs
052 adopt vector quantization for noise-robust representation (Jiang et al., 2024; Pradeepkumar et al.,
053 2025), following the VQ-VAE framework originally designed for images, where homogeneous visual
features make a single tokenizer sufficient (Van Den Oord et al., 2017; Mentzer et al., 2024). In

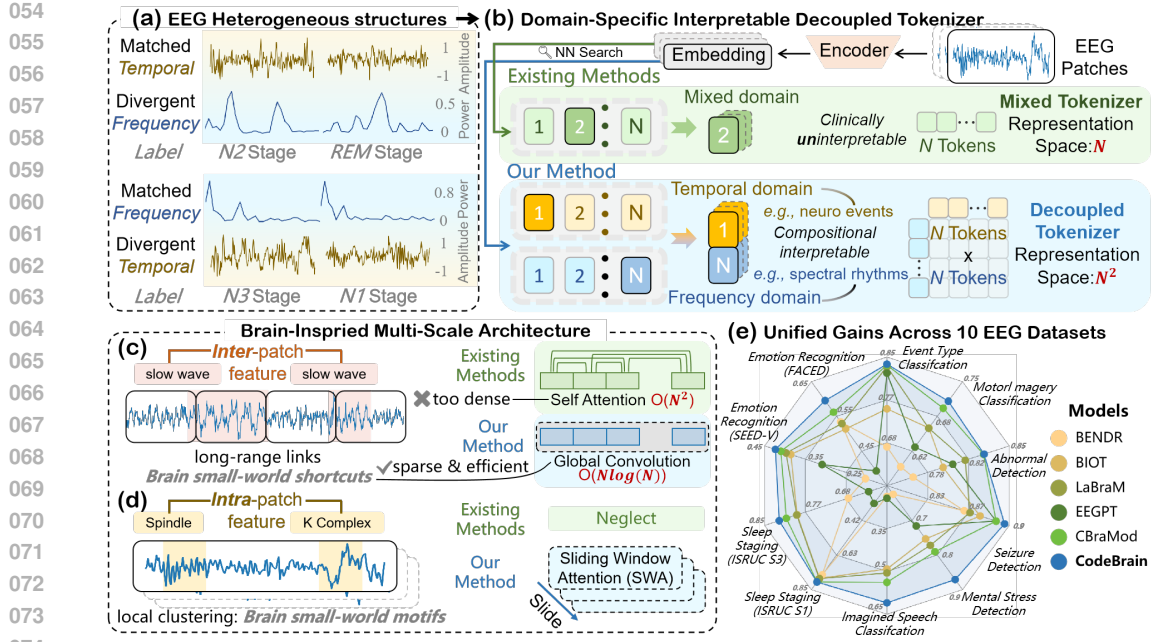


Figure 1: Rationale and overview of *CodeBrain* beyond existing EFM. (a) EEG signals are heterogeneous, as patches matched in one domain may diverge in the other. (b) We then propose a decoupled tokenizer for domain-specific interpretable representations while expanding the representation space. (c-d) Inspired by the brain’s small-world topology, a multi-scale architecture further captures inter-patch dependencies efficiently, while modeling overlooked intra-patch neural events. (e) These designs deliver performance gains across 10 EEG datasets.

contrast, EEG exhibits heterogeneous structures: temporal and frequency components reflect distinct aspects of brain activity (Miwakeichi et al., 2004). As illustrated in Fig. 1(a), signals matched in one domain may diverge in the other. Therefore, a mixed tokenizer can conflate domain-specific patterns (Liu et al., 2024b), weakening representation capacity and producing tokens difficult to align with clinically interpretable neural events or spectral rhythms.

Struggling with Efficiently Modeling Global Brain Dependencies. EEG signals exhibit sparse global dependencies and strong local correlations, reflecting the brain’s small-world topology (Bullmore & Sporns, 2009; Bassett & Bullmore, 2006; He et al., 2009). Efficient modeling of such structure requires capturing relationships in a scalable way. However, most EFM (Yang et al., 2023; Jiang et al., 2024; Wang et al., 2024a; 2025) adopt Transformer architectures with fully connected self-attention (Vaswani et al., 2017). This over-connected design is misaligned with the brain’s sparse structure and struggles to efficiently capture global dependencies due to its quadratic complexity with sequence length (Tay et al., 2021; Hong et al., 2025; Tegon et al., 2025).

Neglecting Local Dependencies within EEG Patches. EEG signals exhibit rich local waveform structures over short temporal windows, reflecting crucial transient neural events (e.g., sleep waveforms in Fig. 1(d)) (Tatum IV, 2021). However, most existing EFM represent each EEG patch as a single token and apply attention mechanisms only at the patch level (Wang et al., 2025; Jiang et al., 2024), thereby ignoring important local dependencies within patches.

To address the above challenges, we propose *CodeBrain*, a novel EEG foundation model that integrates a decoupled tokenizer for domain-specific **representation-level** interpretability with a brain-inspired multi-scale architecture. *CodeBrain* is trained in two stages. In the first stage, we introduce the **TFDual-Tokenizer** (Fig. 1(b)), which decouples temporal and frequency EEG components into discrete tokens. In the second stage, we develop **EEGSSM**, a masked self-supervised framework inspired by the brain’s small-world topology. **EEGSSM** adopts a structured global convolution backbone, conceptually related to recent state-space sequence models (Smith et al., 2023; Li et al., 2022; Gu et al., 2022a), for sparse and efficient global modeling with a sliding window attention

(SWA) mechanism for capturing local neural events overlooked by prior studies (Fig. 1(c–d)). Our detailed contributions are summarized as follows:

- **Decoupled Tokenizer for Domain-Specific Representation-Level Interpretability.** We propose the **TFDual-Tokenizer**, which decouples temporal and frequency EEG components into discrete tokens. This design quadratically expands the representation space, and qualitative analyzes suggest that **some tokens correspond to** neural events and spectral rhythms. A contrastive objective is further applied to the temporal branch to stabilize training. To the best of our knowledge, this is the first tokenizer in EFM to provide domain-specific **representation-level** interpretability.
- **Brain Small-World Topology Inspired Multi-Scale Architecture.** We design **EEGSSM**, a patch-wise self-supervised framework for EEG. Guided by the brain’s small-world topology, it employs structured global convolution to capture sparse long-range temporal dependencies and sliding window attention to model local neural events. In addition, dynamic positional embeddings are used to flexibly learn spatial channel correlations.
- **Strong Generalization and Comprehensive Validation.** Pretrained on the largest publicly available EEG corpus, TUEG (Obeid & Picone, 2016), CodeBrain achieves strong performance on 8 downstream tasks across 10 datasets (Fig. 1(e)) with distribution shifts in cohorts and channel configurations. This suggests the model design plays a central role in generalization. Comprehensive ablations, scaling-law analyses, together with visualization and quantitative analyses, further confirm its robustness, scalability, and provide domain-specific **representation-level** interpretability.

2 METHODOLOGY

2.1 MODEL ARCHITECTURE

We introduce *CodeBrain*, a two-stage pretraining framework designed to learn interpretable and universal EEG representations (Fig. 2). The model is motivated by complementary goals: 1) **domain-specific interpretability** via decoupled tokenization of heterogeneous temporal and frequency information, achieved by the proposed **TFDual-Tokenizer**, and 2) **multi-scale modeling** of EEG sequences inspired by the brain’s small-world topology, addressed by the **EEGSSM** framework. This design lets Stage 1 learn a tokenizer of patch-level codes, while Stage 2 leverages it for EEG representations. We next provide a formal definition of the two stages to clarify their respective roles.

Stage 1: Decoupled Tokenization. Given a normalized EEG patch $\mathbf{x} \in \mathbb{R}^L$, where L is the patch length, our goal is to discretize \mathbf{x} into temporal and frequency tokens, enabling domain-specific representation learning. Specifically, let $Vt \in \mathbb{R}^{K \times D}$ and $Vf \in \mathbb{R}^{K \times D}$ denote the temporal and frequency codebooks, where K is the vocabulary size and D is the embedding dimension of each token. The tokenizer function is defined as: $vt, vf = f_{\text{tokenizer}}(\mathbf{x}), \quad vt, vf \in \mathbb{R}^D$.

Stage 2: EEG Representation Learning. Given unlabeled EEG sequences $\mathcal{X} = \{X_m\}_{m=1}^N$, where each $X_m \in \mathbb{R}^{C \times f \times T}$ consists of C channels, sampling rate f , and T seconds. We divide each sequence into n non-overlapping patches of t seconds, so each patch length is $L = f \cdot t$. The goal is to train an encoder $f_{\text{enc}} : \mathbb{R}^{C \times n \times L} \rightarrow \mathbb{R}^{C \times n \times D}$ that produces latent representations $Z_m = f_{\text{enc}}(X_m)$.

2.2 TFDUAL-TOKENIZER PRETRAINING

Our TFDual-Tokenizer includes a shared *neural encoder*, a *dual tokenizer* with separate codebooks, and two *decoders*. The *neural encoder* extracts joint time-frequency embeddings from EEG patches, which are then discretized into temporal and frequency tokens by the *dual tokenizer*. Each token stream is reconstructed by a decoder to supervise codebook learning in its respective domain.

Neural Encoder For each patch $\mathbf{x}_i \in \mathbb{R}^L$, we apply the Discrete Fourier Transform (DFT) (Cooley & Tukey, 1965) to obtain its frequency representation:

$$\mathbf{x}_i[k] = DFT(\mathbf{x}_i) \quad (1)$$

where $\mathbf{x}_i[k]$ denotes the k -th frequency component. $\mathbf{x}_i[k]$ and the \mathbf{x}_i are fed into the **TFConv module**, where they are processed in parallel through stacks of convolutional, batch normalization, and ReLU layers. The temporal representation $e_i^t = TFConv(\mathbf{x}_i)$ and frequency representation $e_i^f = TFConv(\mathbf{x}_i[k])$ are concatenated to form a time-frequency embedding $e_i^p = \text{Concat}\{e_i^t, e_i^f\}$.

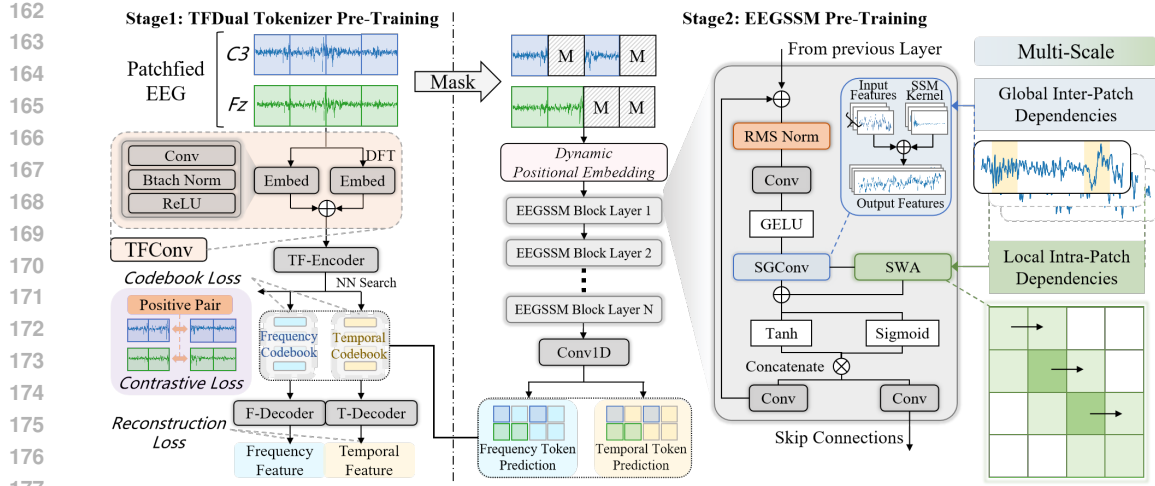


Figure 2: Overview of the *CodeBrain* framework. **Left:** *TFDual-Tokenizer* learns to discretize EEG signals into temporal and frequency tokens using two separate codebooks, by reconstructing both the temporal waveforms and the frequency-domain magnitude and phase. **Right:** *EEGSSM* learns representations by predicting the discrete tokens of masked patches generated by *TFDual-Tokenizer*.

To get patch representation \tilde{e}_i , we then add a positional embedding e_{pos} and feed it into **TF-Encoder**:

$$\tilde{e}_i = \text{Encoder}(e_i^p + e_{\text{pos}}). \quad (2)$$

We choose a Transformer encoder here since this stage is *patch-to-token*, where its ability to model local contextual relations makes it well-suited for capturing patch-level patterns. To keep the tokenizer channel-agnostic, e_{pos} is shared temporal embeddings without channel-specific identities.

Dual Tokenizer We use two separate tokenizers with distinct codebooks for the temporal and frequency domains, denoted as $vt_j, vf_j \in \mathbb{R}^D$, where $j = 1, \dots, K$. Given the patch representation \tilde{e}_i from the neural encoder, each tokenizer independently selects the nearest code from its codebook:

$$pt_i = \arg \min_j \|\tilde{e}_i - vt_j\|^2, \quad pf_i = \arg \min_j \|\tilde{e}_i - vf_j\|^2, \quad (3)$$

where pt_i and pf_i denote the closest positions for the embeddings in the temporal and frequency domain codebook. The effectiveness of the Dual Tokenizer is based on the following proposition:

Proposition 2.1 *Decoupling temporal and frequency codebooks yields representations that are no less effective than those from a joint codebook.*

Proof. See Appendix D.

For this Proposition, we provide empirical validation in Sections 3.4, 3.5 and analysis of Dual Tokenizer's interpretable structure in Appendix B.

Frequency Codebook Training To train the frequency codebook, we reconstruct amplitude and phase from the code embeddings. For each EEG patch, we apply the DFT to obtain the frequency representation: $\mathbf{x}_i[k] = \text{Re}\{\mathbf{x}_i[k]\} + j \cdot \text{Im}\{\mathbf{x}_i[k]\}$ where $\text{Re}\{\mathbf{x}_i[k]\}$ and $\text{Im}\{\mathbf{x}_i[k]\}$ are the real part and imaginary part respectively, then the amplitude and phase can be calculated as:

$$A_i = \sqrt{\text{Re}(\mathbf{x}_i[k])^2 + \text{Im}(\mathbf{x}_i[k])^2}, \quad \phi_i = \arctan 2(\text{Im}(\mathbf{x}_i[k]), \text{Re}(\mathbf{x}_i[k])). \quad (4)$$

We use z-score normalization to ensure stable training. The code embedding vf_i , retrieved from the frequency codebook, is passed through the **F-Decoder**, which consists of a Transformer encoder followed by two linear layers:

$$y_i^A = \text{Encoder}(\text{MLP}(\tilde{e}_i)), \quad y_i^P = \text{Encoder}(\text{MLP}(\tilde{e}_i)). \quad (5)$$

where y_i^A and y_i^P are the predicted amplitude and phase, respectively. The frequency codebook's training objective is the mean squared error (MSE) loss:

$$\mathcal{L}_i^f = \|y_i^A - A_i\|_2^2 + \|y_i^P - \phi_i\|_2^2. \quad (6)$$

216 **Temporal Codebook Training** Direct reconstruction of temporal features might lead to non-
 217 convergence (Jiang et al., 2024). To address this, we combine contrastive loss with reconstruction
 218 loss to train a temporal codebook. Inspired by studies on physiological signals (Kiyasseh et al., 2021),
 219 we assume temporal dependencies exist between EEG segments, especially within the same channel.
 220 For an EEG segment $X_m \in \mathbb{R}^{C \times n \times L}$, we split it into two halves of length $n/2$. We use **TF-Encoder**
 221 in Eq. (2) to obtain the representations of these two parts $X_{m1}, X_{m2} \in \mathbb{R}^{C \times \frac{n}{2} \times L}$ separately:
 222

$$e_{mi}^h = \text{Encoder}(X_{mi}), i \in \{1, 2\}. \quad (7)$$

224 We encourage the latent representations of different parts within a single segment e_{m1}^h and e_{m2}^h to
 225 be similar, while making those of the same part across different segments e_{mi}^h and e_{sk}^h as distinct as
 226 possible, where $X_s \in \mathbb{R}^{C \times n \times L}, s \neq m, k \neq i$. SimCLR loss (Chen et al., 2020) is used for training:
 227

$$\mathcal{L}_m^{CL} = -\log \frac{\exp(\text{sim}(e_{m1}^h, e_{m2}^h)/\tau)}{\sum_{k=1}^{2N} \mathbb{1}_{[k \neq i]} \exp(\text{sim}(e_{mi}^h, e_{sk}^h)/\tau)}, \quad (8)$$

232 where $\text{sim}(e_{m1}^h, e_{m2}^h)$ is the cosine similarity, $\tau > 0$ is the temperature parameter, and $\mathbb{1}_{[k \neq i]}$ is
 233 an indicator function used to exclude itself. We introduce a **T-Decoder** to reconstruct raw signals
 234 from the temporal code embedding \tilde{e}_i , which consists of a Transformer encoder followed by a linear
 235 projection. Let y_t be the Transformer output from Eq. (2); the overall training objective is:
 236

$$\mathcal{L}_i^t = \mathcal{L}_{CL} + \|y_i^t - \mathbf{x}_i\|_2^2, \quad y_i^t = \text{Encoder}(MLP(\tilde{e}_i)). \quad (9)$$

238 Finally, the training objective for the TFDual-Tokenizer can be defined as:
 239

$$\mathcal{L}_{\text{tokenizer}} = \sum_{X_m \in \mathcal{X}} \mathcal{L}_m^{CL} + \sum_{X_m \in \mathcal{X}} \sum_{i=0}^n \mathcal{L}_i^f + \underbrace{\| \text{sg}(\tilde{e}_i) - vt_{pti} \|^2 + \| \text{sg}(\tilde{e}_i) - vf_{pf_i} \|^2}_{\text{codebook loss}} + \underbrace{\| \tilde{e}_i - \text{sg}(vt_{pti}) \|^2 + \| \tilde{e}_i - \text{sg}(vf_{pf_i}) \|^2}_{\text{commitment loss}}, \quad (10)$$

246 where $\text{sg}(\cdot)$ denotes stop-gradient to avoid updating encoder parameters.
 247

248 2.3 EEGSSM PRETRAINING

250 In this stage, we introduce a novel convolutional structured state space model framework, called
 251 **EEGSSM**, composed of multiple *EEGSSM blocks*. To adapt to unseen channels, we first learn
 252 dynamic positional embeddings using a single depthwise 2D convolution with an asymmetric kernel,
 253 following the ACPE design (Wang et al., 2025), enabling the model to learn relative inter-channel
 254 structures and generalize across heterogeneous EEG channel layouts. The resulting features are
 255 processed by EEGSSM blocks. Another 1D convolutional layer then maps the output back to the
 256 token space for reconstructing the indices of masked tokens produced by the TFDual-Tokenizer.
 257

258 **EEGSSM Block** Our EEGSSM block is composed of several blocks, which are integrated together
 259 through a residual connection mechanism. An EEGSSM block consists of a Layer Normalization,
 260 SGConv layer, SWA layer, and a gating component. Afterward, we feed the intermediate variables
 261 into the SGConv layer to obtain a global receptive field through convolution SSM.
 262

263 *SGConv Layer.* SGConv is a structured SSM model (see Appendix C) using convolution architecture,
 264 and its convolution structure can be represented as a DFT formula:
 265

$$y = F_N^{-1} D_k F_N u, D_k = \text{diag}(\bar{K} F_N), \quad (11)$$

266 where F_N denotes the DFT matrix of size N , and the convolution can be computed in $O(N \log N)$
 267 via FFT. As a type of convolutional SSM, SGConv improves the convolution kernel \bar{K} in Eq. (22) by
 268 introducing two features: sparse parameterization and kernel decay, making SGConv easier and more
 269 efficient to compute compared to the traditional S4 kernel. Let L be the length of the input sequence.
 The convolution kernel \bar{K} of SGConv is composed of several sub-kernels. Assuming the size of the

270 first sub-kernel is d , with parameters $w_i \in \mathbb{R}^{d \times d}$, then the number of sub-kernels can be expressed as
 271 $N = \log_2(\frac{L}{d}) + 1$. The convolution kernel \bar{K} in Eq. (22) can thus be initialized as:
 272

$$273 \quad \bar{K} = \frac{1}{Z} [k_0, k_1, \dots, k_{N-1}], k_i = \alpha^i \text{Upsample}_{2^{\max[i-1, 0]} d}(w_i), \quad (12)$$

275 where α denotes the decay coefficient, usually chosen to be 0.5, inducing the decaying structure, and
 276 $\text{Upsample}(x)$ denotes upsample x to length l . We also introduce the normalization constant Z to
 277 ensure that the convolution operation does not change the scale of the input.

278 *Sliding Window Attention Layer.* We included a sliding window attention (SWA) layer to capture
 279 fine-grained local temporal dependencies. We apply a small fixed-length window, allowing the model
 280 to directly access the content within the context of the window through an attention mechanism
 281 by sliding it across the entire sequence, thereby addressing previous models' neglect of intra-patch
 282 temporal information. Furthermore, SWA maintains linear computational complexity to ensure
 283 training speed remains largely unaffected.

284 *Gate Mechanism.* we use a gating mechanism to control the output of the block. We employ a gated
 285 unit similar to Wavenet (Obeid & Picone, 2016), which can suppress useless or irrelevant features
 286 and help stabilize training in deep networks. We concatenate the global features output y_{sg} by the
 287 SGConv layer with the local features output y_{swa} by SWA and feed them into a gated unit:

$$288 \quad z = \tanh(W_f \times \text{Concat}(y_{sg}, y_{swa})) \odot \sigma(W_g \times \text{Concat}(y_{sg}, y_{swa})), \quad (13)$$

$$289 \quad y_1 = \text{Conv}(z), y_2 = \text{Conv}(z) \quad (14)$$

290 where $\tanh(\cdot)$ and $\sigma(\cdot)$ are tanh function and sigmoid function, \odot denotes an element-wise multiplication
 291 operator, W_f and W_g are learnable convolution filters. y_1 becomes the input to the next block,
 292 while y_2 will be aggregated to the output of SSM blocks through a skip connection.
 293

294 **Pre-Training Objective** To help the EEGSSM model learn general EEG representations, we use
 295 a Masked Autoencoder (MAE) for self-supervised pre-training. For a patched sample $X = \{x_i \mid$
 296 $i \in [1, 2, \dots, C]\}$, we randomly generate a mask $\mathcal{M} = \{m_i \mid i \in [1, 2, \dots, C]\}$ from a Bernoulli
 297 distribution of r proportion, where $m_i \in \{0, 1\}$. We reconstruct the token indices of masked EEG
 298 patches from the TFDual-Tokenizer by cross-entropy loss. Let y_i denotes the output of the EEGSSM
 299 block, the probability that the EEG signal matches the corresponding token v_i in the codebooks:
 300

$$301 \quad p(v_i|x_i) = \text{softmax}(\text{Conv1D}(y_i)). \quad (15)$$

303 Suppose the size of the pre-training set is N , the final cross-entropy loss is:

$$304 \quad \mathcal{L}_p = - \sum_{j=0}^N \sum_{n \in \{m_i=1\}}^C p(v_{nj}|x_{nj}). \quad (16)$$

3 EXPERIMENTS

3.1 DATASETS

311 **Pre-Training.** We pretrain CodeBrain on the TUH EEG Corpus (Obeid & Picone, 2016), the largest
 312 publicly available EEG dataset to date. Data processing follows a standardized pipeline: recordings
 313 shorter than 5 minutes are excluded, and the first and last minute of each segment is removed. We
 314 retain 19 commonly used EEG channels (C3, C4, Cz, F3, F4, Fp1, Fp2, F7, F8, Fz, O1, O2, P3, P4,
 315 Pz, T3, T4, T5, T6), selected based on the international 10–20 system for electrode placement (HH,
 316 1958). We apply band-pass filtering (0.3–75 Hz), and notch filtering at 60 Hz to remove noise. The
 317 data is resampled to 200 Hz and divided into 30-second non-overlapping segments. Segments with
 318 absolute amplitudes over 100 μ V are filtered out. To normalize the signals, each value is divided by
 319 100. Each segment is split into 1-second windows, resulting in 570 EEG patches per sample. After
 320 preprocessing, 1,109,545 samples (about 9,246 hours) are retained for pretraining.

321 **Downstream Tasks.** We evaluate CodeBrain on 8 downstream tasks across 10 public EEG datasets,
 322 which span diverse applications and exhibit distribution shifts from the pretraining dataset, to assess
 323 generalizability. Detailed dataset configurations are in Table 3.1. We perform cross-subject or cross-
 session splits with strict separation between training, validation, and test sets. For **FACE**D, we use 80

324 subjects for training, 20 for validation, and the remaining 23 for testing. In **SEED-V**, each session
 325 consists of 15 trials, which are evenly divided into training, validation, and test sets. **ISRUC_S3**
 326 consists of 10 subjects, for which we apply an 8:1:1 cross-subject split. **MentalArithmetic** consists
 327 of 36 subjects, and we use a 7:1:1 cross-subject split. **BCIC2020-T3** follows the official competition
 328 protocol. In **CHB-MIT**, we use recordings from 19 subjects for training, and from 2 subjects each
 329 for validation and testing. Additional dataset details are provided in the Appendix G.

330

331

332

333 Table 1: Summary of Downstream Tasks and Associated EEG Datasets.

334 Downstream Tasks	335 Datasets	336 #Channels	337 Length	338 #Samples	339 Class
335 Emotion Recognition	336 FACED (Chen et al., 2023)	337 32	338 10s	339 10,332	340 9-class
	341 SEED-V (Liu et al., 2021)	342 62	343 1s	344 117,744	345 5-class
346 Sleep Staging	347 ISRUC_S1 (Khalighi et al., 2016)	348 6	349 30s	350 86,320	351 5-class
	352 ISRUC_S3 (Khalighi et al., 2016)	353 6	354 30s	355 8,500	356 5-class
357 Imagined Speech Classification	358 BCIC 2020-T3 (Jeong et al., 2022)	359 64	360 3s	361 6,000	362 5-class
363 Mental Stress Detection	364 Mental Arithmetic (Mumtaz, 2016)	365 20	366 5s	367 1,707	368 2-class
369 Seizure Detection	370 CHB-MIT (Shoeb, 2009)	371 16	372 10s	373 326,993	374 2-class
375 Motor Imagery Classification	376 SHU-MI (Goldberger et al., 2000)	377 32	378 4s	379 11,988	380 2-class
381 Event Type Classification	382 TUEV (Obeid & Picone, 2016)	383 16	384 5s	385 112,491	386 6-class
387 Abnormal Detection	388 TUAB (Obeid & Picone, 2016)	389 16	390 10s	391 409,455	392 2-class

393

394

395

396 3.2 EXPERIMENT SETTINGS

397

398 **Experiment Setup.** (1) Pretraining Setup. All experiments are conducted on NVIDIA A100
 399 GPUs. The **TFDual-Tokenizer** is trained with temporal and frequency codebooks of 4096 codes (32
 400 dimensions) for 20 epochs, using a batch size of 256 and a learning rate of 1e-4, across six A100
 401 GPUs for approximately ten hours. An 8-layer EEGSSM backbone (15.17M) with a masking ratio of
 402 0.5 is trained for 10 epochs, using a batch size of 256 on two A100 GPUs for about 24 hours.

403

404 (2) Finetuning Strategy. We evaluate the quality of the pretrained representations under full finetuning.
 405 All downstream task datasets are resampled to 200 Hz to match the pretraining configuration. A
 406 three-layer MLP is applied to aggregate channel information, compress the x -second sequence, and
 407 map the representation to the target class, with activation and dropout between layers.

408

409 **Baselines.** We compare our model with a comprehensive set of baseline models that include widely
 410 used task-specific models, as well as publicly available EFMIs that have released pretrained weights.
 411 Among the non-foundation baselines, **EEGNet** (Lawhern et al., 2018) and **EEGConformer** (Song
 412 et al., 2022) represent compact architectures designed for efficient EEG decoding. **ContraWR**
 413 (Yang et al., 2021) is a contrastive-learning-based small model, while **ST-Transformer** (Song et al.,
 414 2021) provides a transformer backbone. These models serve as representative lightweight baselines
 415 commonly adopted across EEG classification tasks.

416

417 For EEG foundation models with publicly available pretrained weights, we include five representative
 418 methods that cover diverse pretraining paradigms. **BENDR** (Kostas et al., 2021) adopts a contrastive
 419 learning framework. **BIOT** (Yang et al., 2023) uses patch-based continuous tokenization. **LaBraM**
 420 introduces discrete neural tokens through vector quantization (Jiang et al., 2024). **EEGPT** (Wang
 421 et al., 2024a) and **CBraMod** (Wang et al., 2025) rely on the masked reconstruction of raw EEG
 422 signals.

423

424 **Evaluation Metric.** For multi-class classification, we report **Cohen’s Kappa**, **Weighted F1 score**,
 425 and **Balanced Accuracy**, with Kappa based on validation performance for testing. For binary
 426 classification, we use Area Under the ROC Curve (**AUROC**), Area Under the Precision-Recall Curve
 427 (**AUC-PR**), and **Balanced Accuracy**, with AUROC based on validation performance for testing.
 428 **Balanced Accuracy** is included to mitigate potential class imbalance effects. All experiments are
 429 repeated with five random seeds, and we report the mean and standard deviation.

430

431 More details about hyperparameters, baselines, and evaluation metrics are provided in Appendix I, H.

Table 2: Comparison results of different methods on downstream tasks.

Methods	FACED (9-Class)			SEED-V (5-Class)		
	Cohen's Kappa	Weighted F1	Balanced Acc	Cohen's Kappa	Weighted F1	Balanced Acc
EEGNet	0.3342 \pm 0.0251	0.4124 \pm 0.0141	0.4090 \pm 0.0122	0.1006 \pm 0.0143	0.2749 \pm 0.0098	0.2961 \pm 0.0102
EEGConformer	0.3858 \pm 0.0186	0.4514 \pm 0.0107	0.4559 \pm 0.0125	0.1772 \pm 0.0174	0.3487 \pm 0.0136	0.3537 \pm 0.0112
ContraWR	0.4231 \pm 0.0151	0.4887 \pm 0.0078	0.4887 \pm 0.0078	0.1905 \pm 0.0188	0.3544 \pm 0.0121	0.3546 \pm 0.0105
ST-Transformer	0.4137 \pm 0.0133	0.4795 \pm 0.0096	0.4810 \pm 0.0079	0.1083 \pm 0.0121	0.2833 \pm 0.0105	0.3052 \pm 0.0072
BENDR	0.4716 \pm 0.0095	0.5340 \pm 0.0086	0.5320 \pm 0.0083	0.0335 \pm 0.0062	0.2026 \pm 0.0330	0.2231 \pm 0.0059
BIOT	0.4476 \pm 0.0254	0.5136 \pm 0.0112	0.5118 \pm 0.0118	0.2261 \pm 0.0262	0.3856 \pm 0.0203	0.3837 \pm 0.0187
LaBraM	0.4698 \pm 0.0102	0.5288 \pm 0.0188	0.5273 \pm 0.0107	0.2386 \pm 0.0209	0.3974 \pm 0.0111	0.3976 \pm 0.0138
EEGPT	0.4639 \pm 0.0023	0.3924 \pm 0.0017	0.4607 \pm 0.0014	0.1323 \pm 0.0062	0.3090 \pm 0.0052	0.3061 \pm 0.0044
CBraMod	0.5041 \pm 0.0122	0.5618 \pm 0.0093	0.5509 \pm 0.0089	0.2569 \pm 0.0143	0.4101 \pm 0.0108	0.4091 \pm 0.0097
CodeBrain	0.5406 \pm 0.0084	0.5953 \pm 0.0113	0.5941 \pm 0.0098	0.2735 \pm 0.0032	0.4235 \pm 0.0022	0.4137 \pm 0.0023
Methods	ISRUC_S3 (5-Class)			BCIC 2020-T3 (5-Class)		
	Cohen's Kappa	Weighted F1	Balanced Acc	Cohen's Kappa	Weighted F1	Balanced Acc
EEGNet	0.7396 \pm 0.0155	0.7407 \pm 0.0184	0.7121 \pm 0.0134	0.4413 \pm 0.0102	0.3016 \pm 0.0123	0.4413 \pm 0.0096
EEGConformer	0.7482 \pm 0.0164	0.7501 \pm 0.0211	0.7212 \pm 0.0181	0.4488 \pm 0.0154	0.3133 \pm 0.0183	0.4506 \pm 0.0133
ContraWR	0.7493 \pm 0.0150	0.7513 \pm 0.0185	0.7226 \pm 0.0164	0.4407 \pm 0.0182	0.3078 \pm 0.0218	0.4257 \pm 0.0162
ST-Transformer	0.7388 \pm 0.0195	0.7399 \pm 0.0223	0.7116 \pm 0.0197	0.4247 \pm 0.0138	0.2941 \pm 0.0159	0.4126 \pm 0.0122
BENDR	0.5995 \pm 0.0151	0.6789 \pm 0.0142	0.6352 \pm 0.0095	0.0607 \pm 0.0093	0.2379 \pm 0.0165	0.2485 \pm 0.0075
BIOT	0.7168 \pm 0.0119	0.7834 \pm 0.0096	0.7598 \pm 0.0109	0.3650 \pm 0.0176	0.4917 \pm 0.0079	0.4920 \pm 0.0086
LaBraM	0.7194 \pm 0.0162	0.7843 \pm 0.0189	0.7617 \pm 0.0122	0.3800 \pm 0.0242	0.5054 \pm 0.0205	0.5060 \pm 0.0155
EEGPT	0.6160 \pm 0.0856	0.6375 \pm 0.0632	0.6650 \pm 0.0311	0.0567 \pm 0.0164	0.2441 \pm 0.0105	0.2453 \pm 0.0131
CBraMod	0.7407 \pm 0.0251	0.8056 \pm 0.0219	0.7844 \pm 0.0126	0.4216 \pm 0.0163	0.5383 \pm 0.0096	0.5373 \pm 0.0108
CodeBrain	0.7671 \pm 0.0091	0.8202 \pm 0.0071	0.7856 \pm 0.0031	0.5127 \pm 0.0065	0.6101 \pm 0.0053	0.6101 \pm 0.0052
Methods	Mental Arithmetic (2-Class)			CHB-MIT (2-Class)		
	AUROC	AUC-PR	Balanced Acc	AUROC	AUC-PR	Balanced Acc
EEGNet	0.7321 \pm 0.0108	0.5763 \pm 0.0102	0.6770 \pm 0.0116	0.8048 \pm 0.0136	0.1914 \pm 0.0182	0.5658 \pm 0.0106
EEGConformer	0.7424 \pm 0.0128	0.5829 \pm 0.0134	0.6805 \pm 0.0123	0.8226 \pm 0.0170	0.2209 \pm 0.0215	0.5976 \pm 0.0141
ContraWR	0.7332 \pm 0.0082	0.5787 \pm 0.0164	0.6631 \pm 0.0097	0.8103 \pm 0.0144	0.2279 \pm 0.0183	0.6351 \pm 0.0122
ST-Transformer	0.7132 \pm 0.0174	0.5672 \pm 0.0259	0.6631 \pm 0.0173	0.8237 \pm 0.0491	0.1422 \pm 0.0094	0.5915 \pm 0.0195
BENDR	0.6248 \pm 0.0765	0.3661 \pm 0.0672	0.5681 \pm 0.0448	0.8632 \pm 0.0526	0.3071 \pm 0.1240	0.5609 \pm 0.0432
BIOT	0.7536 \pm 0.0144	0.6004 \pm 0.0195	0.6875 \pm 0.0186	0.8761 \pm 0.0284	0.3277 \pm 0.0460	0.7068 \pm 0.0457
LaBraM	0.7721 \pm 0.0093	0.5999 \pm 0.0155	0.6909 \pm 0.0125	0.8679 \pm 0.0199	0.3287 \pm 0.0402	0.7075 \pm 0.0358
EEGPT	0.7162 \pm 0.0171	0.5081 \pm 0.0275	0.5597 \pm 0.0171	0.8892 \pm 0.0066	0.3073 \pm 0.0641	0.5481 \pm 0.0151
CBraMod	0.7905 \pm 0.0073	0.6267 \pm 0.0099	0.7256 \pm 0.0132	0.8892 \pm 0.0154	0.3689 \pm 0.0382	0.7398 \pm 0.0284
CodeBrain	0.8707 \pm 0.0209	0.7177 \pm 0.0421	0.7514 \pm 0.0203	0.8961 \pm 0.0174	0.4377 \pm 0.0288	0.7273 \pm 0.0240

3.3 COMPARISON WITH BASELINES

We ensure consistent data splits across all baselines. Results are reported on six representative downstream datasets, with additional results provided in Appendix J. As shown in Table 2, CodeBrain achieves consistent performance gains compared to baselines. For multi-class classification, it achieves the largest gain of +0.0911 in Cohen's Kappa (21.6%), +0.0718 in Weighted F1 score (13.3%), +0.0728 in Balanced Acc (13.5%) on *BCIC 2020-T3* over the strongest baseline (Wang et al., 2025). For binary classification, it achieves the largest gain of +0.0802 in AUROC (10.1%), +0.0910 in AUC-PR (14.5%) and +0.0258 in Balanced Acc (3.6%) on *Mental Arithmetic* over the strongest baseline. These results demonstrate the superior generalizability of CodeBrain.

We conduct ablation studies on three datasets with the same five seeds as in the main experiments to evaluate the key components of CodeBrain (Table 3.3). Below is the detailed analysis:

(1) *Tokenizer configuration*: we compare the proposed *TFDual-Tokenizer (Dual)* with variants using a single domain codebook (**Temporal** or **Frequency**) or a shared codebook that jointly reconstructs both domains (**Mixed**). Across all datasets, the Dual codebook consistently yields superior performance.

432

433

Table 3: The results of ablation studies for tokenizer configurations and module components.

434

Dataset	Codebook	CL	SWA	SGConv	Gate	Cohen's Kappa	Weighted F1	Balanced Accuracy
FACED 9-Class	Dual	✓	✓	✓	✓	0.5406 ± 0.0084	0.5953 ± 0.0113	0.5941 ± 0.0098
	Temporal	✓	✓	✓	✓	0.4618 ± 0.0072	0.5277 ± 0.0067	0.5217 ± 0.0056
	Frequency	✓	✓	✓	✓	0.5006 ± 0.0224	0.5607 ± 0.0201	0.5580 ± 0.0187
	Mixed	✓	✓	✓	✓	0.4676 ± 0.0061	0.5319 ± 0.0052	0.5281 ± 0.0049
	Dual	✗	✓	✓	✓	0.5222 ± 0.0082	0.5811 ± 0.0084	0.5765 ± 0.0074
	Dual	✓	✗	✓	✓	0.5192 ± 0.0092	0.5792 ± 0.0093	0.5736 ± 0.0075
	Dual	✓	✓	✗	✓	0.1936 ± 0.1637	0.2627 ± 0.1824	0.2858 ± 0.1467
SEED-V 5-Class	Dual	✓	✓	✓	✗	0.2578 ± 0.0340	0.3363 ± 0.0270	0.3431 ± 0.0316
	Dual	✓	✓	✓	✓	0.2735 ± 0.0032	0.4235 ± 0.0022	0.4137 ± 0.0023
	Temporal	✓	✓	✓	✓	0.2633 ± 0.0116	0.4152 ± 0.0092	0.4068 ± 0.0074
	Frequency	✓	✓	✓	✓	0.2665 ± 0.0208	0.4186 ± 0.0177	0.4098 ± 0.0147
	Mixed	✓	✓	✓	✓	0.2708 ± 0.0047	0.4214 ± 0.0044	0.4124 ± 0.0032
	Dual	✗	✓	✓	✓	0.2589 ± 0.0065	0.4129 ± 0.0056	0.4029 ± 0.0042
	Dual	✓	✗	✓	✓	0.2561 ± 0.0051	0.4106 ± 0.0042	0.4019 ± 0.0034
ISRU.S3 5-Class	Dual	✓	✓	✗	✓	0.2062 ± 0.0099	0.3707 ± 0.0075	0.3620 ± 0.0083
	Dual	✓	✓	✓	✗	0.2212 ± 0.0076	0.3826 ± 0.0057	0.3757 ± 0.0052
	Dual	✓	✓	✓	✓	0.7671 ± 0.0091	0.8202 ± 0.0071	0.7856 ± 0.0031
	Temporal	✓	✓	✓	✓	0.7314 ± 0.0210	0.7916 ± 0.0181	0.7565 ± 0.0244
	Frequency	✓	✓	✓	✓	0.7390 ± 0.0601	0.7986 ± 0.0514	0.7728 ± 0.0361
	Mixed	✓	✓	✓	✓	0.7400 ± 0.0217	0.7999 ± 0.0171	0.7673 ± 0.0157
	Dual	✗	✓	✓	✓	0.7558 ± 0.0333	0.8130 ± 0.0264	0.7801 ± 0.0132

452

453

454

(2) *Contrastive learning (CL)*: We evaluate the impact of contrastive learning in TFDual-Tokenizer pretraining. It leads to consistent gains, indicating a better capture of temporal patterns. Moreover, the CL facilitates the convergence of the temporal codebook, with detailed analyzes provided in Appendix F.

(3) *Components of EEGSSM*: Evaluating the **SWA**, **SGConv**, and **Gate** modules, which demonstrate improvements in EEG representation learning. **Including the SWA module consistently improves performance, confirming its regularization effect in capturing local dependencies. The gating mechanism also shows large impact, as it effectively stabilizes fine-tuning and prevents overfitting.**

(4) *Scaling Laws*: Prior works (Wang et al., 2025; Jiang et al., 2024) explored scaling with 1-1000 hours of EEG data for pretraining. We extend to 1k-9k hours and 3M-150M models, **ranging from a 3.86M 3-layer model with a hidden size of 128 to a 146.75M 12-layer model with hidden size of 384, enabling a systematic exploration of scaling laws across depth and width**. As shown in Figure 3, Kappa consistently improves with more data and parameters. These results confirm that larger models yield consistent but diminishing returns. **Detailed results and efficiency analysis are provided in Appendix N. These findings indicate that the 8-layer (15.17M) model is a balanced choice between performance and computational efficiency.**

We further investigate several key design choices, including mask ratio, SWA window size, codebook size, patch size, **SGConv kernel parameters, and subband contributions** in Appendix K. We report robustness experiments in Appendix M and computational efficiency in Appendix L. We also provide low-resource comparisons (Appendix O) and pretraining curves (Appendix E), showing stable VQ convergence and efficient EEGSSM training.

476

477

478

479

480

481

482

483

484

485

FACED

SEED-V

ISRU_S3

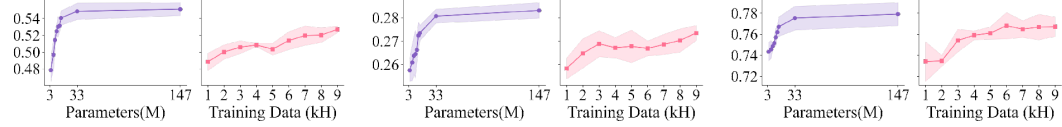
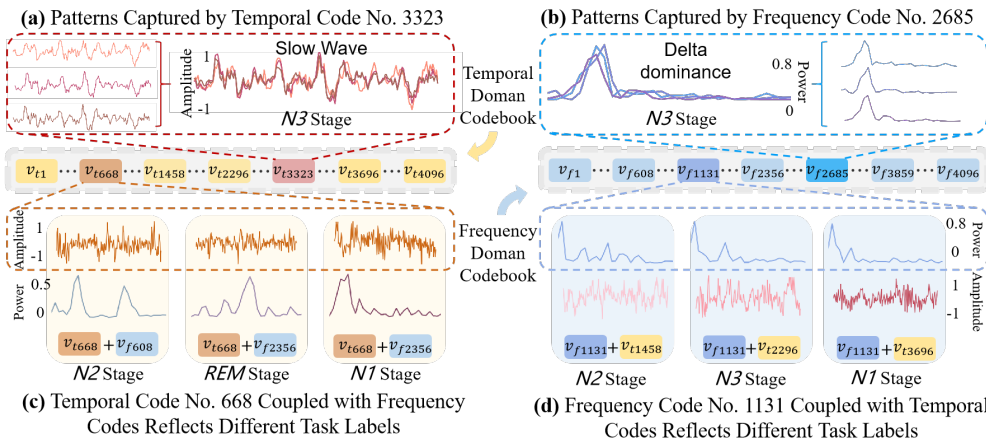


Figure 3: Model and training data scaling laws of CodeBrain across three datasets on Cohen's Kappa.

486 3.5 VECTOR VISUALIZATION
487

488 To demonstrate how the **TFDual-Tokenizer** models heterogeneous EEG, we visualize its learned
489 temporal and frequency codes on the ISRUC_S3 dataset **by mapping individual code indices back to**
490 **their corresponding raw signals**. As shown in Figure 4(a)(b), each domain-specific codebook captures
491 meaningful **representation-level** structures: temporal codes align with neural events (e.g., slow waves),
492 while frequency codes highlight spectral rhythms such as dominant delta activity, **both of which are**
493 **informative** for sleep staging. However, in many cases, **neither domain alone is sufficient**, and richer
494 **structure emerges only from their composition**, as in Figure 4(c)(d), where the same temporal code
495 can pair with different frequency codes, and vice versa, to yield complementary representations. This
496 decoupled design expands the representation space and enhances **representation-level** interpretability,
497 with additional **meaningful tokens** to neurophysiological features and quantitative analyzes provided
498 in Appendix B.
499

514 Figure 4: Decoupled time-frequency codes visualization on ISRUC_S3 dataset.
515
516

517 4 CONCLUSION
518

519 In this paper, we present *CodeBrain*, an EEG foundation model that unifies interpretable tokenization
520 with a brain-inspired multi-scale architecture. The TFDual-Tokenizer decouples heterogeneous
521 EEG signals, expanding the representation space while suggesting domain-specific **representation-**
522 **level** interpretability, and the EEGSSM architecture integrates structured global convolution with
523 sliding-window attention to efficiently capture both long-range and local dependencies. Pretrained
524 on the large-scale TUEG corpus, CodeBrain demonstrates strong generalization across 8 tasks and
525 10 datasets under distribution shifts, with comprehensive ablations, scaling-law analyses confirming
526 robustness and scalability. These results establish CodeBrain as a strong foundation for neural
527 time-series representation learning.
528
529
530
531
532
533
534
535
536
537
538
539

540 **ETHICS STATEMENT**
541

542 This research adheres to the ICLR Code of Ethics and Responsible Research Guidelines. We confirm
543 that all aspects of the study conform to these guidelines. The work preserves anonymity requirements
544 and does not deviate from the ethical principles set by ICLR. This paper does not involve human
545 subjects, crowdsourcing, or sensitive user data. No Institutional Review Board (IRB) approval was
546 required. The work does not release models or datasets with a high risk of misuse, and it poses no
547 privacy, security, or legal compliance concerns. Furthermore, it does not contain potentially harmful
548 insights, discrimination or bias issues, or conflicts of interest. All experiments are conducted on
549 publicly available EEG datasets, following research integrity and responsible research practices as
550 required by the ICLR Code of Ethics. In addition, disclosures regarding the use of LLM are in the
551 Appendix R.
552

553 **REPRODUCIBILITY STATEMENT**
554

555 We have made extensive efforts to ensure the reproducibility of our work. The complete imple-
556 mentation and training scripts are provided in the anonymous code repository (Appendix Q). For
557 theoretical results, all assumptions and complete proofs of the claims are included in Appendix D.
558 For experimental reproducibility, we provide a detailed description of the datasets, preprocessing
559 procedures, and evaluation protocols in Section G, as well as comprehensive hyperparameter settings
560 in Appendix I. These materials together ensure that both the theoretical and empirical results can be
561 independently verified.
562

563 **REFERENCES**
564

565 Josh Achiam, Steven Adler, Sandhini Agarwal, Lama Ahmad, Ilge Akkaya, Florencia Leoni Aleman,
566 Diogo Almeida, Janko Altenschmidt, Sam Altman, Shyamal Anadkat, et al. Gpt-4 technical report.
567 *arXiv preprint arXiv:2303.08774*, 2023.

568 Danielle Smith Bassett and ED Bullmore. Small-world brain networks. *The neuroscientist*, 12(6):
569 512–523, 2006.

570 Richard B Berry, Rita Brooks, Charlene E Gamaldo, Susan M Harding, Carole Marcus, Bradley V
571 Vaughn, et al. The aasm manual for the scoring of sleep and associated events. *Rules, Terminology
572 and Technical Specifications, Darien, Illinois, American Academy of Sleep Medicine*, 176(2012):7,
573 2012.

574 Ed Bullmore and Olaf Sporns. Complex brain networks: graph theoretical analysis of structural and
575 functional systems. *Nature reviews neuroscience*, 10(3):186–198, 2009.

577 Mathilde Caron, Hugo Touvron, Ishan Misra, Hervé Jégou, Julien Mairal, Piotr Bojanowski, and
578 Armand Joulin. Emerging properties in self-supervised vision transformers. In *Proceedings of the
579 IEEE/CVF international conference on computer vision*, pp. 9650–9660, 2021.

581 Chi-Sheng Chen, Ying-Jung Chen, and Aidan Hung-Wen Tsai. Large cognition model: Towards
582 pretrained eeg foundation model. *arXiv preprint arXiv:2502.17464*, 2025a.

583 Jingjing Chen, Xiaobin Wang, Chen Huang, Xin Hu, Xinkle Shen, and Dan Zhang. A large finer-
584 grained affective computing eeg dataset. *Scientific Data*, 10(1):740, 2023.

586 Ting Chen, Simon Kornblith, Mohammad Norouzi, and Geoffrey Hinton. A simple framework for
587 contrastive learning of visual representations. In *International conference on machine learning*, pp.
588 1597–1607. PmLR, 2020.

589 Zheng Chen, Yasuko Matsubara, Yasushi Sakurai, and Jimeng Sun. Long-term eeg partitioning
590 for seizure onset detection. In *Proceedings of the AAAI Conference on Artificial Intelligence*,
591 volume 39, pp. 14221–14229, 2025b.

593 James W Cooley and John W Tukey. An algorithm for the machine calculation of complex fourier
594 series. *Mathematics of computation*, 19(90):297–301, 1965.

594 Fernando Lopes da Silva. Eeg and meg: relevance to neuroscience. *Neuron*, 80(5):1112–1128, 2013.
595

596 Tri Dao, Daniel Y Fu, Khaled K Saab, Armin W Thomas, Atri Rudra, and Christopher Ré.
597 Hungry hungry hippos: Towards language modeling with state space models. *arXiv preprint*
598 *arXiv:2212.14052*, 2022.

599 Jacob Devlin, Ming-Wei Chang, Kenton Lee, and Kristina Toutanova. Bert: Pre-training of deep
600 bidirectional transformers for language understanding. In *Proceedings of the 2019 conference of*
601 *the North American chapter of the association for computational linguistics: human language*
602 *technologies, volume 1 (long and short papers)*, pp. 4171–4186, 2019.
603

604 Daniel Y Fu, Elliot L Epstein, Eric Nguyen, Armin W Thomas, Michael Zhang, Tri Dao, Atri Rudra,
605 and Christopher Ré. Simple hardware-efficient long convolutions for sequence modeling. In
606 *International Conference on Machine Learning*, pp. 10373–10391. PMLR, 2023.

607 Ary L Goldberger, Luis AN Amaral, Leon Glass, Jeffrey M Hausdorff, Plamen Ch Ivanov, Roger G
608 Mark, Joseph E Mietus, George B Moody, Chung-Kang Peng, and H Eugene Stanley. Physiobank,
609 physiotoolkit, and physionet: components of a new research resource for complex physiologic
610 signals. *Circulation*, 101(23):e215–e220, 2000.

611 Albert Gu, Tri Dao, Stefano Ermon, Atri Rudra, and Christopher Ré. Hippo: Recurrent memory
612 with optimal polynomial projections. *Advances in neural information processing systems*, 33:
613 1474–1487, 2020.
614

615 Albert Gu, Karan Goel, and Christopher Ré. Efficiently modeling long sequences with structured
616 state spaces. *arXiv preprint arXiv:2111.00396*, 2021.

617 Albert Gu, Karan Goel, Ankit Gupta, and Christopher Ré. On the parameterization and initialization
618 of diagonal state space models. *Advances in Neural Information Processing Systems*, 35:35971–
619 35983, 2022a.
620

621 Albert Gu, Karan Goel, and Christopher Re. Efficiently modeling long sequences with structured
622 state spaces. In *The Tenth International Conference on Learning Representations*, 2022b.

623 Michele Guerra, Roberto Milanese, Michele Deodato, Madalina G Ciobanu, and Fausto Fasano.
624 Exploring the diagnostic potential of llms in schizophrenia detection through eeg analysis. In *2024*
625 *IEEE International Conference on Bioinformatics and Biomedicine (BIBM)*, pp. 6812–6819. IEEE,
626 2024.

627 Yiyu Gui, MingZhi Chen, Yuqi Su, Guibo Luo, and Yuchao Yang. Eegmamba: Bidirectional
628 state space model with mixture of experts for eeg multi-task classification, 2024. URL <https://arxiv.org/abs/2407.20254>.
629

630 Yong He, Jinhui Wang, Liang Wang, Zhang J Chen, Chaogan Yan, Hong Yang, Hehan Tang, Chaozhe
631 Zhu, Qiyong Gong, Yufeng Zang, et al. Uncovering intrinsic modular organization of spontaneous
632 brain activity in humans. *PloS one*, 4(4):e5226, 2009.

633 JASPER HH. The ten-twenty electrode system of the international federation. *Electroenceph clin*
634 *Neurophysiol*, 10:367–380, 1958.

635 Jiazhen Hong, Geoffrey Mackellar, and Soheila Ghane. Eegm2: An efficient mamba-2-based
636 self-supervised framework for long-sequence eeg modeling. *arXiv preprint arXiv:2502.17873*,
637 2025.

638 Yongquan Hu, Shuning Zhang, Ting Dang, Hong Jia, Flora D Salim, Wen Hu, and Aaron J Quigley.
639 Exploring large-scale language models to evaluate eeg-based multimodal data for mental health.
640 In *Companion of the 2024 on ACM International Joint Conference on Pervasive and Ubiquitous*
641 *Computing*, pp. 412–417, 2024.

642 Ji-Hoon Jeong, Jeong-Hyun Cho, Young-Eun Lee, Seo-Hyun Lee, Gi-Hwan Shin, Young-Seok
643 Kweon, José del R Millán, Klaus-Robert Müller, and Seong-Whan Lee. 2020 international
644 brain–computer interface competition: A review. *Frontiers in human neuroscience*, 16:898300,
645 2022.

648 Ziyu Jia, Youfang Lin, Xiyang Cai, Haobin Chen, Haijun Gou, and Jing Wang. Sst-emotionnet:
649 Spatial-spectral-temporal based attention 3d dense network for eeg emotion recognition. In
650 *Proceedings of the 28th ACM international conference on multimedia*, pp. 2909–2917, 2020a.
651

652 Ziyu Jia, Youfang Lin, Jing Wang, Kaixin Yang, Tianhang Liu, and Xinwang Zhang. Mmcnn: A
653 multi-branch multi-scale convolutional neural network for motor imagery classification. In *Joint*
654 *European Conference on Machine Learning and Knowledge Discovery in Databases*, pp. 736–751.
655 Springer, 2020b.

656 Ziyu Jia, Youfang Lin, Jing Wang, Ronghao Zhou, Xiaojun Ning, Yuanlai He, and Yaoshuai Zhao.
657 Graphsleepnet: Adaptive spatial-temporal graph convolutional networks for sleep stage classifica-
658 tion. In *Ijcai*, volume 2021, pp. 1324–1330, 2020c.

659 Weibang Jiang, Liming Zhao, and Bao-liang Lu. Large brain model for learning generic represen-
660 tations with tremendous eeg data in bci. In *The Twelfth International Conference on Learning*
661 *Representations*, 2024.

662 Weibang Jiang, Yansen Wang, Bao-liang Lu, and Dongsheng Li. Neurolm: A universal multi-task
663 foundation model for bridging the gap between language and eeg signals. In *The Thirteenth*
664 *International Conference on Learning Representations*, 2025.

665 Sirvan Khalighi, Teresa Sousa, José Moutinho Santos, and Urbano Nunes. Isruc-sleep: A comprehen-
666 sive public dataset for sleep researchers. *Computer methods and programs in biomedicine*, 124:
667 180–192, 2016.

668 Dani Kiyasseh, Tingting Zhu, and David A Clifton. Clocs: Contrastive learning of cardiac signals
669 across space, time, and patients. In *International Conference on Machine Learning*, pp. 5606–5615.
670 PMLR, 2021.

671 Demetres Kostas, Stephane Aroca-Ouellette, and Frank Rudzicz. Bendl: Using transformers and a
672 contrastive self-supervised learning task to learn from massive amounts of eeg data. *Frontiers in*
673 *Human Neuroscience*, 15:653659, 2021.

674 Taku Kudo and John Richardson. Sentencepiece: A simple and language independent subword
675 tokenizer and detokenizer for neural text processing. In *Proceedings of the 2018 Conference on*
676 *Empirical Methods in Natural Language Processing: System Demonstrations*, pp. 66–71, 2018.

677 Vernon J Lawhern, Amelia J Solon, Nicholas R Waytowich, Stephen M Gordon, Chou P Hung, and
678 Brent J Lance. Eegnet: a compact convolutional neural network for eeg-based brain–computer
679 interfaces. *Journal of neural engineering*, 15(5):056013, 2018.

680 Hyojin Lee, You Rim Choi, Hyun Kyung Lee, Jaemin Jeong, Joopyo Hong, Hyun-Woo Shin, and
681 Hyung-Sin Kim. Explainable vision transformer for automatic visual sleep staging on multimodal
682 psg signals. *npj Digital Medicine*, 8(1):55, 2025.

683 Yuhong Li, Tianle Cai, Yi Zhang, Deming Chen, and Debadeepa Dey. What makes convolutional
684 models great on long sequence modeling? *arXiv preprint arXiv:2210.09298*, 2022.

685 Zhenqi Li, Jing Wang, Ziyu Jia, and Youfang Lin. Learning space-time-frequency representation
686 with two-stream attention based 3d network for motor imagery classification. In *2020 IEEE*
687 *International Conference on Data Mining (ICDM)*, pp. 1124–1129. IEEE, 2020.

688 Chenyu Liu, Xinliang Zhou, Zhengri Zhu, Liming Zhai, Ziyu Jia, and Yang Liu. Vbh-gnn: Variational
689 bayesian heterogeneous graph neural networks for cross-subject emotion recognition. In *The*
690 *Twelfth International Conference on Learning Representations*, 2024a.

691 Qijiong Liu, Xiaoyu Dong, Jiaren Xiao, Nuo Chen, Hengchang Hu, Jieming Zhu, Chenxu Zhu,
692 Tetsuya Sakai, and Xiao-Ming Wu. Vector quantization for recommender systems: a review and
693 outlook. *arXiv preprint arXiv:2405.03110*, 2024b.

694 Wei Liu, Jie-Lin Qiu, Wei-Long Zheng, and Bao-Liang Lu. Comparing recognition performance
695 and robustness of multimodal deep learning models for multimodal emotion recognition. *IEEE*
696 *Transactions on Cognitive and Developmental Systems*, 14(2):715–729, 2021.

702 Jingying Ma, Qika Lin, Ziyu Jia, and Mengling Feng. St-usleepnet: A spatial-temporal coupling
703 prominence network for multi-channel sleep staging. In *Proceedings of the Thirty-Fourth Interna-*
704 *tional Joint Conference on Artificial Intelligence*, pp. 4182–4190, 2025.

705 Fabian Mentzer, David Minnen, Eirikur Agustsson, and Michael Tschanne. Finite scalar quantization:
706 Vq-vae made simple. In *The Twelfth International Conference on Learning Representations*, 2024.

708 Fumikazu Miwakeichi, Eduardo Martínez-Montes, Pedro A Valdés-Sosa, Nobuaki Nishiyama, Hi-
709 roaki Mizuhara, and Yoko Yamaguchi. Decomposing eeg data into space–time–frequency compo-
710 nents using parallel factor analysis. *NeuroImage*, 22(3):1035–1045, 2004.

711 Navid Mohammadi Foumani, Geoffrey Mackellar, Soheila Ghane, Saad Irtza, Nam Nguyen, and
712 Mahsa Salehi. Eeg2rep: enhancing self-supervised eeg representation through informative masked
713 inputs. In *Proceedings of the 30th ACM SIGKDD Conference on Knowledge Discovery and Data
714 Mining*, pp. 5544–5555, 2024.

716 Wajid Mumtaz. MDD Patients and Healthy Controls EEG Data (New). Figshare, November 2016.
717 URL https://figshare.com/articles/dataset/EEG_Data_New/4244171.

718 Ernst Niedermeyer and FH Lopes da Silva. *Electroencephalography: basic principles, clinical
719 applications, and related fields*. Lippincott Williams & Wilkins, 2005.

721 Iyad Obeid and Joseph Picone. The temple university hospital eeg data corpus. *Frontiers in
722 neuroscience*, 10:196, 2016.

723 Jathurshan Pradeepkumar, Xihao Piao, Zheng Chen, and Jimeng Sun. Single-channel eeg tokenization
724 through time-frequency modeling. *arXiv preprint arXiv:2502.16060*, 2025.

726 Aniruddh Raghu, Payal Chandak, Ridwan Alam, John Guttag, and Collin M. Stultz. Sequential
727 multi-dimensional self-supervised learning for clinical time series, 2023.

728 Syama Sundar Rangapuram, Matthias W Seeger, Jan Gasthaus, Lorenzo Stella, Yuyang Wang, and
729 Tim Januschowski. Deep state space models for time series forecasting. *Advances in neural
730 information processing systems*, 31, 2018.

731 Rico Sennrich, Barry Haddow, and Alexandra Birch. Neural machine translation of rare words with
732 subword units. In *54th Annual Meeting of the Association for Computational Linguistics*, pp.
733 1715–1725. Association for Computational Linguistics (ACL), 2016.

735 Ali Hossam Shoeb. *Application of machine learning to epileptic seizure onset detection and treatment*.
736 PhD thesis, Massachusetts Institute of Technology, 2009.

737 Jimmy TH Smith, Andrew Warrington, and Scott W Linderman. Simplified state space layers for
738 sequence modeling. *arXiv preprint arXiv:2208.04933*, 2022.

740 Jimmy TH Smith, Andrew Warrington, and Scott W Linderman. Simplified state space layers for
741 sequence modeling. In *ICLR*, 2023.

742 Yonghao Song, Xueyu Jia, Lie Yang, and Longhan Xie. Transformer-based spatial-temporal feature
743 learning for eeg decoding. *arXiv preprint arXiv:2106.11170*, 2021.

745 Yonghao Song, Qingqing Zheng, Bingchuan Liu, and Xiaorong Gao. Eeg conformer: Convolutional
746 transformer for eeg decoding and visualization. *IEEE Transactions on Neural Systems and
747 Rehabilitation Engineering*, 31:710–719, 2022.

748 William O Tatum IV. *Handbook of EEG interpretation*. Springer Publishing Company, 2021.

750 Yi Tay, Mostafa Dehghani, Samira Abnar, Yikang Shen, Dara Bahri, Philip Pham, Jinfeng Rao,
751 Liu Yang, Sebastian Ruder, and Donald Metzler. Long range arena : A benchmark for efficient
752 transformers. In *The Ninth International Conference on Learning Representations*, 2021. URL
753 <https://openreview.net/forum?id=qVyeW-grC2k>.

754 Anna Tegon, Thorir Mar Ingolfsson, Xiaying Wang, Luca Benini, and Yawei Li. Femba: Effi-
755 cient and scalable eeg analysis with a bidirectional mamba foundation model. *arXiv preprint
arXiv:2502.06438*, 2025.

756 Xuan-The Tran, Linh Le, Quoc Toan Nguyen, Thomas Do, and Chin-Teng Lin. Eeg-ssm: Leveraging
757 state-space model for dementia detection. *arXiv preprint arXiv:2407.17801*, 2024.

758

759 Aaron Van Den Oord, Oriol Vinyals, et al. Neural discrete representation learning. In *Advances in*
760 *neural information processing systems*, volume 30, 2017.

761

762 Ashish Vaswani, Noam Shazeer, Niki Parmar, Jakob Uszkoreit, Llion Jones, Aidan N Gomez, Łukasz
763 Kaiser, and Illia Polosukhin. Attention is all you need. In *Advances in neural information*
764 *processing systems*, volume 30, 2017.

765

766 Guangyu Wang, Wenchao Liu, Yuhong He, Cong Xu, Lin Ma, and Haifeng Li. Eegpt: Pretrained
767 transformer for universal and reliable representation of eeg signals. In *Advances in Neural*
768 *Information Processing Systems*, volume 37, pp. 39249–39280, 2024a.

769

770 Jiquan Wang, Sha Zhao, Haiteng Jiang, Yangxuan Zhou, Zhenghe Yu, Tao Li, Shijian Li, and Gang
771 Pan. Caresleepnet: a hybrid deep learning network for automatic sleep staging. *IEEE Journal of*
772 *Biomedical and Health Informatics*, 2024b.

773

774 Jiquan Wang, Sha Zhao, Zhiling Luo, Yangxuan Zhou, Haiteng Jiang, Shijian Li, Tao Li, and Gang
775 Pan. Cbramod: A criss-cross brain foundation model for eeg decoding. In *The Third International*
776 *Conference on Learning Representations*, 2025.

777

778 Wenhai Wang, Jifeng Dai, Zhe Chen, Zhenhang Huang, Zhiqi Li, Xizhou Zhu, Xiaowei Hu, Tong Lu,
779 Lewei Lu, Hongsheng Li, et al. Internimage: Exploring large-scale vision foundation models with
780 deformable convolutions. In *Proceedings of the IEEE/CVF conference on computer vision and*
781 *pattern recognition*, pp. 14408–14419, 2023.

782

783 Chaoqi Yang, Danica Xiao, M Brandon Westover, and Jimeng Sun. Self-supervised eeg representation
784 learning for automatic sleep staging. *arXiv preprint arXiv:2110.15278*, 2021.

785

786 Chaoqi Yang, M Westover, and Jimeng Sun. Biot: Biosignal transformer for cross-data learning in
787 the wild. In *Advances in Neural Information Processing Systems*, volume 36, pp. 78240–78260,
788 2023.

789

790 Zhizhang Yuan, Daoze Zhang, Junru Chen, Gefei Gu, and Yang Yang. Brant-2: Foundation model
791 for brain signals. *CoRR*, 2024.

792

793 Daoze Zhang, Zhizhang Yuan, Yang Yang, Junru Chen, Jingjing Wang, and Yafeng Li. Brant:
794 Foundation model for intracranial neural signal. *Advances in Neural Information Processing*
795 *Systems*, 36:26304–26321, 2023.

796

797 Daoze Zhang, Zhizhang Yuan, Junru Chen, Kerui Chen, and Yang Yang. Brant-x: A unified
798 physiological signal alignment framework. In *Proceedings of the 30th ACM SIGKDD Conference*
799 *on Knowledge Discovery and Data Mining*, pp. 4155–4166, 2024.

800

801 Ruizhe Zheng, Daoze Zhang, Zhizhang Yuan, Junru Chen, Yang Yang, et al. Beatrix: Out-of-
802 distribution generalization of large eeg model via invariant contrastive fine-tuning.

803

804 Ruizhe Zheng, Jun Li, Yi Wang, Tian Luo, and Yuguo Yu. Scatterformer: locally-invariant scat-
805 tering transformer for patient-independent multispectral detection of epileptiform discharges. In
806 *Proceedings of the AAAI Conference on Artificial Intelligence*, volume 37, pp. 148–158, 2023.

807

808 Ruizhe Zheng, Lingyan Mao, Dingding Han, Tian Luo, Yi Wang, Jing Ding, and Yuguo Yu. Fapex:
809 Fractional amplitude-phase expressor for robust cross-subject seizure prediction. *arXiv preprint*
arXiv:2511.03263, 2025.

810

811 Linqi Zhou, Michael Poli, Winnie Xu, Stefano Massaroli, and Stefano Ermon. Deep latent state
812 space models for time-series generation. In *International Conference on Machine Learning*, pp.
813 42625–42643. PMLR, 2023.

814

815 Xinliang Zhou, Chenyu Liu, Zhisheng Chen, Kun Wang, Yi Ding, Ziyu Jia, and Qingsong Wen. Brain
816 foundation models: A survey on advancements in neural signal processing and brain discovery.
817 *arXiv preprint arXiv:2503.00580*, 2025.

810	Appendix Contents	
811		
812	A Related Work	17
813		
814	B Interpretability Analyses of TFDUAL-TOKENIZER Representations	17
815	B.1 Exploring Frequency Token Patterns in Relation to Spectral Rhythms	18
816	B.2 Exploring Temporal Token Patterns in Relation to Neural Events	19
817	B.3 Class-Specific Token Ratio Analysis for TFDUAL-TOKENIZER	20
818	B.4 Additional Ablations on Codebook Contribution	21
819	C Structure State Space Model	21
820		
821	D Theoretical Analysis of Decoupled Codebook Training	23
822		
823	E Pretraining Results	24
824	E.1 TFDUAL-TOKENIZER Pretraining Results	24
825	E.2 EEGSSM Pretraining Results	25
826	F Improving Temporal Codebook Learning via Contrastive Loss	25
827		
828	G Dataset Description	26
829		
830	H Baselines and Metrics Description	28
831	H.1 Metrics	28
832	H.2 Baselines	28
833	I Hyperparameter Setting	29
834	I.1 Pretraining Settings	29
835	I.2 Parameters of EEGSSM	29
836	I.3 Fine-tuning Settings on Downstream Tasks	29
837		
838	J Additional Evaluation on Other BCI Tasks	30
839		
840	K Ablation on Design Choices	33
841	K.1 Ablation on Mask Ratio	33
842	K.2 Ablation on SWA Window Size	36
843	K.3 Ablation on Codebook Size	36
844	K.4 Ablation on Patch Size	37
845	K.5 Ablation on SGConv Kernel Parameters	37
846	K.6 Ablation on Subband	38
847	L Backbone Efficiency Comparison	40
848		
849	M Model Robustness	41
850	M.1 Random Channel Dropout	41
851	M.2 Brain-Region Channel Dropout	41
852	M.3 Non-stationary Robustness	43
853	N Detailed Results on Scaling Laws	44
854	N.1 Scaling Laws with Respect to Training Data Volume	44
855	N.2 Scaling Laws with Respect to Model Size	44
856	N.3 Computational Analysis Across Scales.	47
857		
858	O Low-Resource Comparison With Existing Methods	50
859		
860	P Limitations and Future Work	51
861		
862	Q Code Access	51
863	R Use of LLM	51

864 **A RELATED WORK**
865

866 **EEG Foundation Models.** Inspired by foundation models in vision and language (Wang et al.,
867 2023; Achiam et al., 2023), EEG research is shifting from task-specific models (Jia et al., 2020c; Wang
868 et al., 2024b; Chen et al., 2025b) (Zheng et al., 2023) to EFM s for learning expressive representations.
869 Current EFM s can be divided into two categories. 1) Contrastive learning-based (CL) (Chen et al.,
870 2025a): BENDER (Kostas et al., 2021) first showed the ability of CL for EEG representations. Then,
871 the Brant series (Zhang et al., 2023; Yuan et al., 2024; Zhang et al., 2024) enables joint representation
872 learning across physiological signals using CL. 2) Reconstruction-based: BIOT (Yang et al., 2023)
873 pioneers cross-modal pretraining for biosignals, including EEG. Subsequent models focus specifically
874 on EEG, learning representations by predicting masked discrete tokens (Jiang et al., 2024; 2025)
875 or reconstructing raw signals (Wang et al., 2024a; Mohammadi Foumani et al., 2024; Wang et al.,
876 2025). Most existing EFM s adopt Transformer architecture, which is suboptimal for EEG due to poor
877 handling of sparse dependencies, quadratic complexity, and ignoring local dependencies by treating
878 each patch as a token.

879
880 **EEG Tokenization.** Tokenization has been key in NLP for generating generalizable and inter-
881 pretable input representations (Sennrich et al., 2016; Kudo & Richardson, 2018). Inspired by this,
882 early EFM s used patch-based continuous tokenization (Yang et al., 2023; Yuan et al., 2024) to handle
883 EEG noise and variability, but without quantization, leading to unbounded and less interpretable
884 representations. LaBraM (Jiang et al., 2024) introduced vector quantization to learn discrete EEG
885 tokens, following the VQ-VAE design from vision tasks (Van Den Oord et al., 2017). However, this
886 direct transfer overlooks EEG’s heterogeneous structure, limiting representation capacity. Moreover,
887 the tokenizer of LaBraM is trained only on frequency-domain reconstruction due to convergence
888 issues with raw signals reconstruction. Later efforts (Pradeepkumar et al., 2025; Jiang et al., 2025)
889 (Zheng et al.) adopted a single codebook under a **frequency-dominant pretraining paradigm**, limiting
890 the representation space and interpretability.

891
892 **State Space Model.** Recent works have focused on enhancing classic State-Space Models (SSM)
893 to more efficiently model sequential data using deep learning. For example, Rangapuram et al. (2018)
894 used recurrent neural networks to learn parameters in SSM. However, the most significant progress
895 came from Gu et al. (2021) with the introduction of the structured state space model (S4), which
896 reduces the computational complexity of SSM in modeling long sequences using a special state
897 transition matrix (Gu et al., 2020). These low-rank and normal matrices enable SSM to compute
898 global convolution kernels efficiently through fast Fourier transform across the entire sequence.
899 Subsequently, some works have further improved the shortcomings of S4 in areas such as model
900 architecture (Smith et al., 2022) and convolution (Raghu et al., 2023), and have started applying
901 it to tasks such as natural language processing (Dao et al., 2022) and time series analysis (Zhou
902 et al., 2023). Recently, some works have also been applied to the EEG data, Tran et al. (Tran et al.,
903 2024) leveraging SSMs to detect dementia. They extract temporal information from EEG signals
904 through the Mamba architecture and combine it with frequency domain features to better manage
905 the complexity of multivariate EEG. In the work of Gui et al. (2024) Zheng et al. (2025), SSM has
906 also become the backbone network of the EEG foundation model. This further highlights the fast
907 reasoning speed and efficient memory usage of the SSM model when processing EEG signals.

908 **B INTERPRETABILITY ANALYSES OF TFDUAL-TOKENIZER**
909 **REPRESENTATIONS**
910

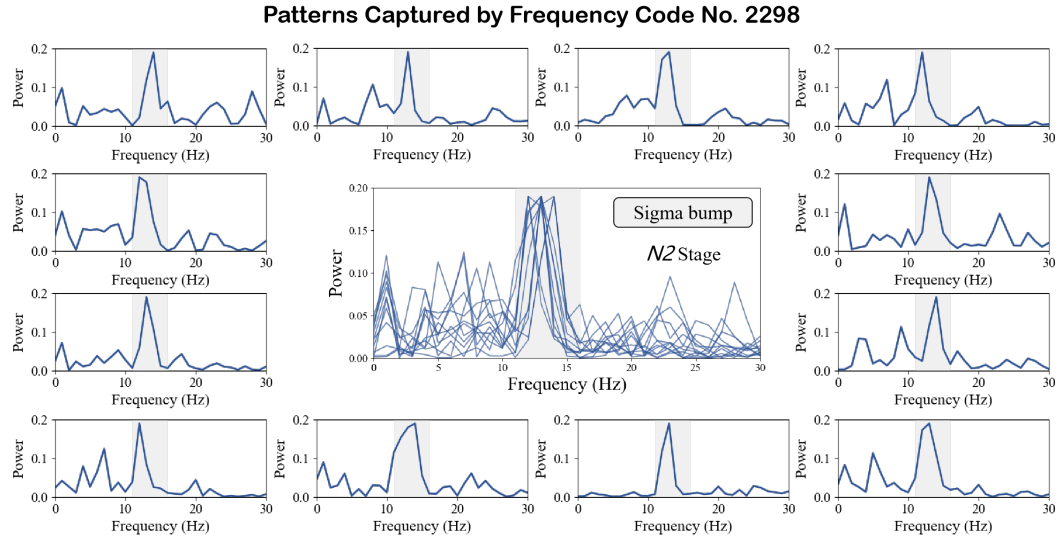
911
912 We conduct representation-level interpretability analyses of the decoupled TFDUAL-TOKENIZER.
913 As case studies, we visualize selected tokens alongside well-established physiological patterns, il-
914 lustrating that frequency codes reflect spectral rhythms and temporal codes align with characteristic
915 waveform events. These qualitative examples show that the tokenizer does not discretize signals
916 arbitrarily but organizes them into domain-relevant structures. We further complement these visual-
917 izations with a quantitative analysis of class-specific token usage across four datasets, demonstrating
918 that the learned codebooks induce structured representation patterns.

918
919

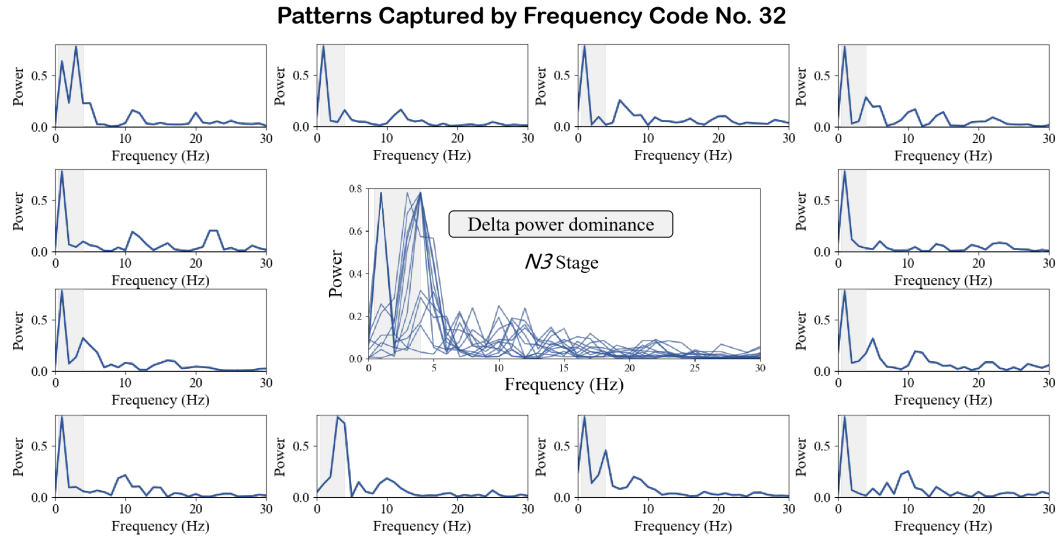
920 B.1 EXPLORING FREQUENCY TOKEN PATTERNS IN RELATION TO SPECTRAL RHYTHMS 921

922 To illustrate the [interpretable structure](#) of the learned frequency tokens, we take sleep staging as an
923 downstream dataset. We focus on N2 and N3 stages, since they are characterized by the
924 most distinctive spectral rhythms in clinical sleep scoring: *spindle* in the sigma band (11-16 Hz) for
925 N2, and *slow wave* in the delta band (0.5-4 Hz) for N3. [Using token-activation statistics from the
926 ISRUC_S3 test set, we select the most frequently activated class-specific frequency tokens.](#)
927

928 As shown in Figure 5, [frequency code No. 2298 tends to capture a sigma bump, with prominent peaks
929 localized in the spindle range. This is similar to N2 spindles \(Berry et al., 2012\).](#) Quantitatively, this
930 code exhibited a clear sigma peak in approximately 15.4% of its assigned patches. Similarly, Figure 6
931 shows that frequency code No. 32 predominantly encodes delta dominance, a typical frequency
932 feature of N3 sleep. This code displayed clear delta dominance in about 18.3% of its assigned
933 segments. Taken together, these findings suggest that our frequency-branch tokenizer helps establish
934 a frequency vocabulary for EEG.



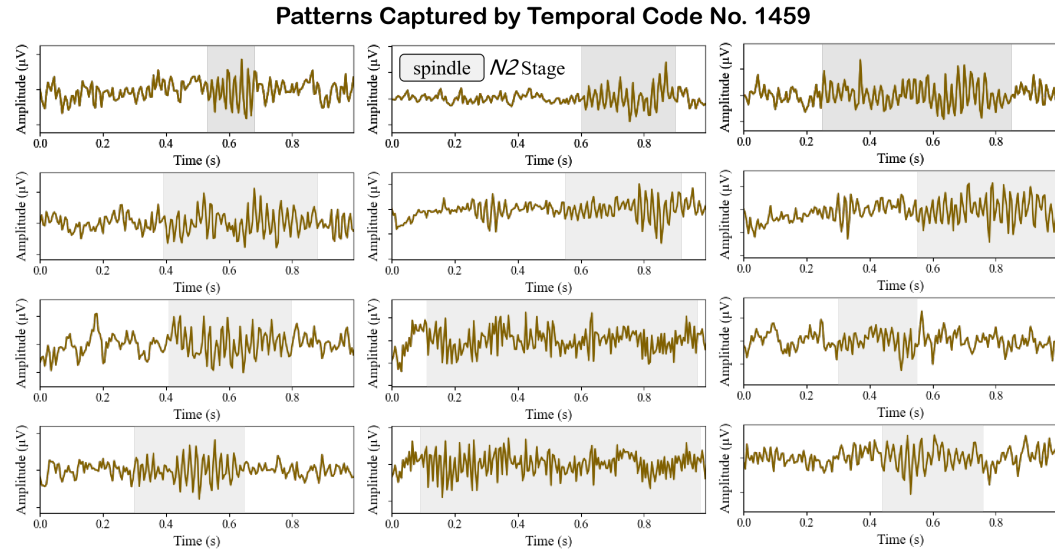
950 Figure 5: Frequency code capturing sigma bump, a typical spectral rhythm of N2 stage.
951



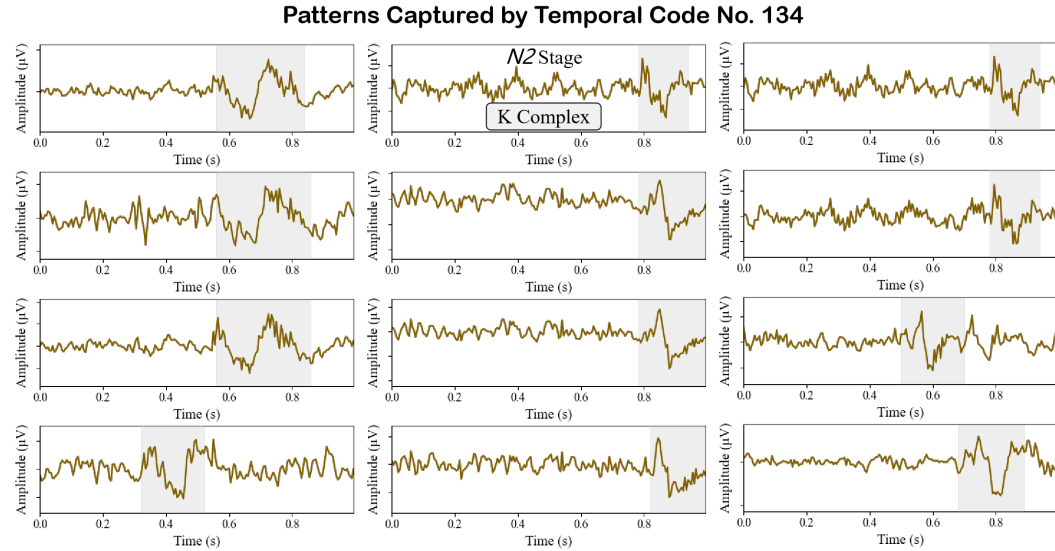
970 Figure 6: Frequency code capturing delta dominance, a typical spectral rhythm of N3 stage.
971

972 B.2 EXPLORING TEMPORAL TOKEN PATTERNS IN RELATION TO NEURAL EVENTS 973

974 In addition to spectral rhythms, we applied the same token-activation-based selection procedure to
975 the temporal codes on ISRUC_S3 to examine whether the tokenizer captures coherent and clinically
976 recognizable structures in the raw EEG waveforms. Figure 8 and Figure 7 show that certain codes
977 align with K-complexes and sleep spindles, the hallmark waveforms of N2 sleep. Quantitatively,
978 $\approx 5.34\%$ of the assigned patches contained K-complexes and $\approx 7.01\%$ contained spindles. These
979 rates are consistent with clinical expectations (1–2 K-complexes and 2–5 spindles per minute in N2
980 Berry et al. (2012)) and, when considering the overall prevalence of N2 in five-class sleep staging,
981 still substantially exceed what would be expected from random token usage.



1001 Figure 7: Temporal code capturing sleep spindle, a typical neural events of N2 stage.



1021 Figure 8: Temporal code capturing K complex, a typical neural events of N2 stage.

1022 Figure 9 shows that temporal code No. 1537 corresponds to slow waves, the defining feature of N3
1023 sleep, occurring in $\approx 40.4\%$ of its assigned patches. This exceeds the 20% per-epoch criterion for N3
1024 scoring Berry et al. (2012) and, given the overall prevalence of N3, indicates that this token provides
1025 a meaningful link to neural events.

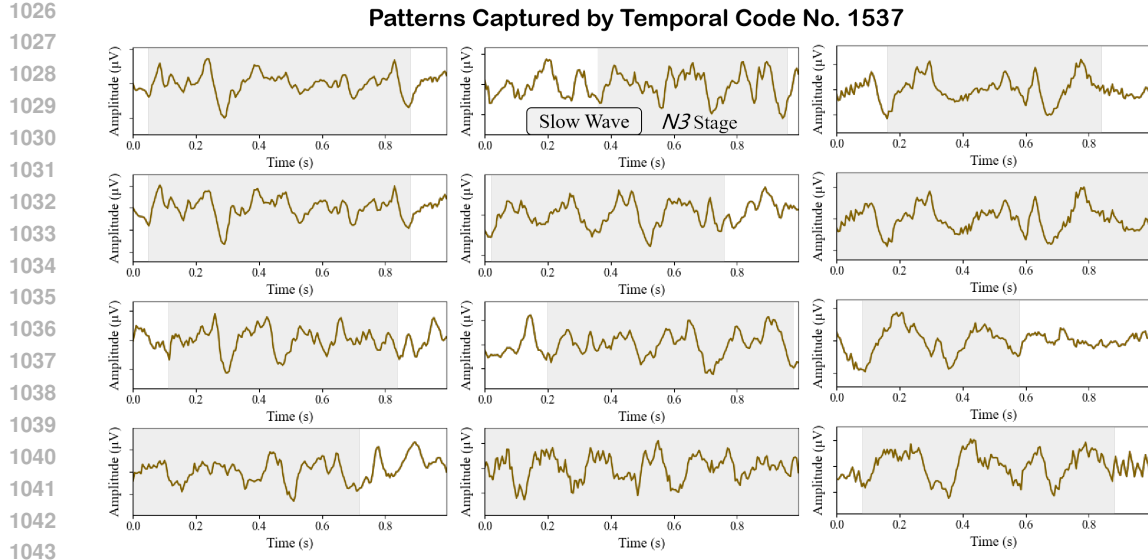


Figure 9: Temporal code capturing slow wave, a typical neural events of N3 stage.

Taken together, these observations suggest that the temporal branch of our tokenizer contributes to establishing a vocabulary of neurophysiological events, complementing the frequency-domain findings. While temporal waveforms are often noisier and harder to model than spectral rhythms (Jiang et al., 2024), our decoupled design allows temporal tokens to emerge with meaningful associations to critical neural events. This indicates that the temporal branch offers useful [insights](#) to clinically relevant waveforms and demonstrates the effectiveness of our approach in capturing complementary structure.

B.3 CLASS-SPECIFIC TOKEN RATIO ANALYSIS FOR TFDUAL-TOKENIZER

To further characterize the representation structure learned by the TFDUAL-TOKENIZER, we analyze the distribution of token usage across classes on unseen downstream datasets. This analysis aims to examine whether the decoupled tokenizer induces more structured and class-consistent token activation patterns, which would support our motivation for separating temporal and frequency domains at the representation level.

A token (code) is considered class-specific if it predominantly appears in samples of a single class. Formally, for a given token c , let $N_c^{(y)}$ denote the number of times c appears in class y . The dominance ratio is defined as:

$$\text{Dominance}(c) = \frac{\max_y N_c^{(y)}}{\sum_y N_c^{(y)}} \quad (17)$$

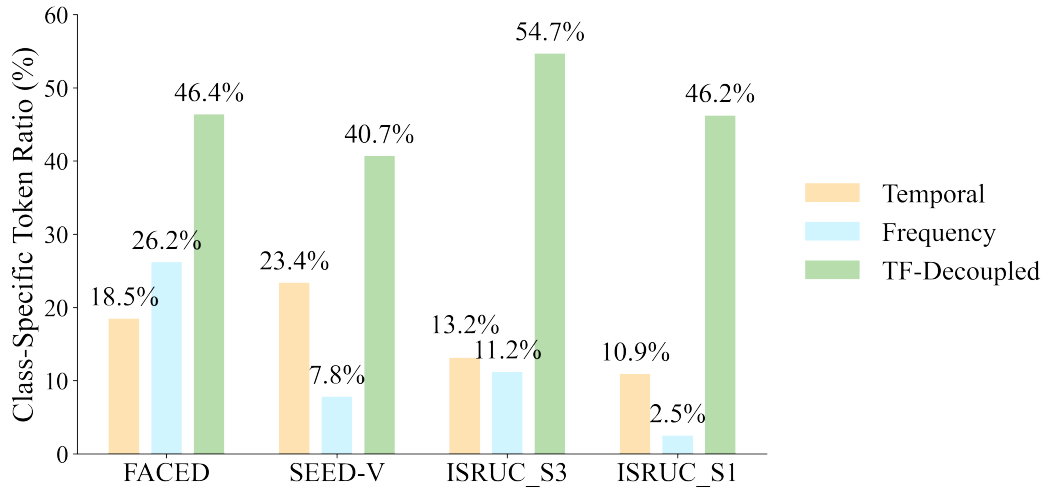
If $\text{Dominance}(c) \geq \tau$ (we use $\tau = 1$), the token is deemed class-specific. The class-specific ratio for a codebook is then computed as:

$$\text{Class-Specific Token Ratio} = \frac{\# \text{ class-specific tokens}}{\text{Total tokens in codebook}} \quad (18)$$

Figure 10 illustrates the proportion of class-specific tokens derived from three configurations: using only the temporal codebook, only the frequency codebook, and a combination of both (TF-Decoupled). We employ two independent codebooks to capture complementary information via the proposed TFDUAL-TOKENIZER module.

Across all four datasets, including two for emotion recognition (FACED and SEED-V) and two for sleep staging (ISRUC_S3 and ISRUC_S1), the decoupled codebook consistently achieves the highest class-specific token ratios, reaching 54.7% on ISRUC_S3 and 46.4% on FACED. These

1080
1081 results confirm that decoupling temporal and frequency domain information significantly enhances
1082 the model’s ability to capture **structured** representation.



1099
1100 Figure 10: Class-Specific Code Ratio Across Different Codebooks.
1101
1102

1103 B.4 ADDITIONAL ABLATIONS ON CODEBOOK CONTRIBUTION 1104

1105 To further examine the role of the tokenizer in pretraining, we provide additional exploratory evidence
1106 on how the the codebooks influence representation learning. These analyses extend the comparisons
1107 in Table 3.3, where the decoupled design outperforms temporal-only, frequency-only, and mixed
1108 codebooks. Specifically, we compare the following two ablations on the ISRUC_S3 dataset:

- 1109 • **Raw-signal reconstruction.** We remove the tokenizer entirely and train the EEGSSM
1110 backbone directly to reconstruct raw waveforms, thereby eliminating the discretization step.
- 1111 • **Masked codebook.** We identify the top 50% most frequently activated tokens across both
1112 codebooks on ISRUC_S3. During pretraining, whenever a segment is assigned one of these
1113 tokens, we replace it with a placeholder, effectively masking half of the vocabulary and
1114 preventing the model from relying on these high-activation codes.

1115 Table 4 reports downstream performance on ISRUC_S3 under these settings.
1116
1117

1118 Table 4: Ablations of the codebook contribution on ISRUC_S3.
1119

Setting	Cohen’s κ	Weighted F1	Balanced Acc
TFDual.tokenizer (ours)	0.7671 \pm 0.0091	0.8202 \pm 0.0071	0.7856 \pm 0.0031
Raw-signal Reconstruction	0.7503 \pm 0.0087	0.8014 \pm 0.0079	0.7763 \pm 0.0048
Masked Codebook	0.7426 \pm 0.0102	0.7931 \pm 0.0084	0.7690 \pm 0.0063

1124 These experiments do not suggest that specific interpretable codes directly determine task outcomes.
1125 However, they provide supporting evidence that the decoupled tokenizer imparts useful structure
1126 during pretraining, and that entirely removing or partially disabling the codebooks leads to consistently
1127 degraded downstream performance. These observations reinforce the contribution of the tokenizer at
1128 the representation level.
1129

1130 C STRUCTURE STATE SPACE MODEL 1131

1132 The state-space model is a classic model in control theory, and it represents the operational state of a
1133 system using first-order differential equations (ODE). A continuous state-space model can be defined

1134 in the following form:

$$1135 \quad x'(t) = Ax(t) + Bu(t), y(t) = Cx'(t) + Du(t), \quad (19)$$

1136 where $u(t)$ is a vector that represents the input of the system, while $y(t)$ is a vector that represents the
 1137 output of the system. $x(t)$ and its derivative $x'(t)$ represent the latent states of the system, typically
 1138 in the form of an N-D vector. And A, B, C, D here are the state, input, output, and feedforward
 1139 matrices, defining the relationship between the input, output, and state vector. Following Gu et al.
 1140 (Gu et al., 2022b), \bar{D} is set equal to 0 since it can be replaced by the residual connection. Now,
 1141 Equation 20 resembles an architecture similar to RNN, allowing us to recurrently compute x_k . Let
 1142 the initial state be $x_{k-1} = 0$, and we can unroll Eq 20 as follows:

$$1143 \quad y_k = \bar{C}A^k\bar{B}u_0 + \bar{C}A^{k-1}\bar{B}u_1 + \dots + \bar{C}A\bar{B}u_{k-1} + \bar{C}\bar{B}u_k \quad (20)$$

$$1144 \quad y = \bar{K}u, \quad \bar{K} = (\bar{C}\bar{B}, \bar{C}A^1\bar{B}, \dots, \bar{C}A^k\bar{B}). \quad (21)$$

1145 Therefore, SSM can be transformed from the form of a recurrent neural network to a convolutional
 1146 neural network. During training, the \bar{K} can be considered as a 1-D globe convolution kernel, so
 1147 the y can be calculated via the "long" convolution, allowing us to use the fast Fourier transform to
 1148 efficiently compute the SSM convolutional kernel \bar{K} . However, directly computing the convolution
 1149 in Equation 21 can be very expensive for long sequences. We can use the Fast Fourier Transform to
 1150 accelerate it. The form of this convolution can be written as:

$$1151 \quad y = F_N^{-1}D_kF_Nu, D_k = \text{diag}(\bar{K}F_N), \quad (22)$$

1152 where F_N denotes the DFT matrix of size N . This FFT convolution has a computational complexity
 1153 of $O(n \log(n))$. Following (Li et al., 2022; Fu et al., 2023), we hope to parameterize K directly rather
 1154 than through $\{A, B, C\}$ because we can eliminate complex parameterization and accelerate the entire
 1155 convolution.

1156 While Eq. 22 shows that the SSM can be computed using FFT-based convolution, it is important to
 1157 formalize the complexity guarantee. We now state the following proposition.

1158 **Proposition 1.** *Let (A, B, C, D) denote the discretized state-space matrices of an S4 layer, with input
 1159 sequence $u \in \mathbb{R}^N$. The output $y \in \mathbb{R}^N$ can be written as a linear convolution $y = k * u$ with kernel*

$$1160 \quad k_0 = D, \quad k_n = CA^{n-1}B, \quad n \geq 1.$$

1161 *Using the convolution theorem and the FFT, this convolution can be computed in time $\Theta(N \log N)$.*

1162 *Proof.* This proof follows the proof in *Lemma C.2* of Gu et al. (2021):

1163 Expanding the recurrence

$$1164 \quad x_{n+1} = Ax_n + Bu_n, \quad y_n = Cx_n + Du_n, \quad (23)$$

1165 yields

$$1166 \quad y_n = Du_n + \sum_{t=0}^{n-1} CA^{n-1-t}B u_t = \sum_{t=0}^n k_{n-t} u_t, \quad (24)$$

1167 where $k_0 = D$ and $k_n = CA^{n-1}B$. Thus $y = k * u$.

1168 Let \mathcal{F}_N denote the N -point DFT. By the convolution theorem,

$$1169 \quad \mathcal{F}_N(y) = \mathcal{F}_N(k) \odot \mathcal{F}_N(u), \quad (25)$$

1170 so that

$$1171 \quad y = \mathcal{F}_N^{-1}(\mathcal{F}_N(k) \odot \mathcal{F}_N(u)). \quad (26)$$

1172 The cost of forward FFT, element-wise product, and inverse FFT is $\Theta(N \log N)$.

1173 The S4 parameterization ensures A admits a diagonal-plus-low-rank (DPLR) structure, so the kernel
 1174 takes the form

$$1175 \quad k_n = \sum_{j=1}^r \alpha_j \lambda_j^{n-1}, \quad r \ll N. \quad (27)$$

1176 Each exponential sequence can be generated recursively in $\mathcal{O}(N)$, yielding all k_0, \dots, k_{N-1} in linear
 1177 time.

1178 Combining the above,

$$1179 \quad T(N) = \underbrace{\Theta(N \log N)}_{\text{FFT convolution}} + \underbrace{\mathcal{O}(N)}_{\text{kernel generation}} = \Theta(N \log N). \quad (28)$$

1188 D THEORETICAL ANALYSIS OF DECOUPLED CODEBOOK TRAINING 1189

1190 **Proposition 2.1.** *Let $X = (X_t, X_f)$ denote the temporal and frequency representations of an
1191 EEG segment, assumed approximately independent. Consider an additive reconstruction distortion
1192 $d(x, \hat{x}) = d_t(x_t, \hat{x}_t) + d_f(x_f, \hat{x}_f)$. Under a fixed total codebook size $K = 2^R$, a product codebook
1193 $\mathcal{C}_t \times \mathcal{C}_f$ with $|\mathcal{C}_t| = 2^{R_t}$ and $|\mathcal{C}_f| = 2^{R_f}$, $R_t + R_f = R$, achieves a minimum expected distortion*

$$1195 D_{\text{prod}}^*(R) = \min_{R_t + R_f = R} (D_t^*(R_t) + D_f^*(R_f)), \quad (29)$$

1197 which satisfies

$$1198 D_{\text{mix}}^*(R) \geq D_{\text{prod}}^*(R), \quad (30)$$

1199 where $D_{\text{mix}}^*(R)$ is the minimum distortion of a single mixed codebook $\mathcal{C}_{\text{mix}} \subset \mathbb{R}^{d_t+d_f}$ of size 2^R .

1200 *Proof.* The argument combines the separability of the rate–distortion (R–D) function for independent
1201 sources under additive distortion and the high-rate quantization approximation to the Shannon R–D
1202 limit.

1204 Let $X = (X_t, X_f)$ with $X_t \perp X_f$, and distortion

$$1205 d(x, \hat{x}) = d_t(x_t, \hat{x}_t) + d_f(x_f, \hat{x}_f). \quad (31)$$

1207 Then the Shannon R–D function satisfies

$$1208 R(D) = \min_{D_t + D_f = D} (R_t(D_t) + R_f(D_f)), \quad (32)$$

1209 where $R_t(\cdot)$ and $R_f(\cdot)$ are the marginal R–D functions for X_t and X_f . By convex duality, the optimal
1210 test channel factorizes:

$$1213 p(\hat{x}_t, \hat{x}_f | x_t, x_f) = p(\hat{x}_t | x_t) p(\hat{x}_f | x_f), \quad (33)$$

1214 and the optimal distortion allocation solves

$$1216 \min_{D_t, D_f} R_t(D_t) + R_f(D_f) \quad \text{s.t. } D_t + D_f = D, \quad (34)$$

1217 with KKT condition $R'_t(D_t^*) = R'_f(D_f^*)$.

1219 At rate R_t bits for X_t and R_f bits for X_f (with $R_t + R_f = R$), the minimal achievable distortions are
1220 $D_t^*(R_t)$ and $D_f^*(R_f)$. In the high-rate regime, practical vector quantizers approach these Shannon
1221 limits, yielding

$$1222 D_{\text{prod}}(R_t, R_f) \approx D_t^*(R_t) + D_f^*(R_f). \quad (35)$$

1223 Optimizing over all feasible splits gives

$$1225 D_{\text{prod}}^*(R) = \min_{R_t + R_f = R} (D_t^*(R_t) + D_f^*(R_f)). \quad (36)$$

1227 Any mixed codebook $\mathcal{C}_{\text{mix}} \subset \mathbb{R}^{d_t+d_f}$ with $|\mathcal{C}_{\text{mix}}| = 2^R$ cannot beat the Shannon R–D limit, so

$$1229 D_{\text{mix}}^*(R) \geq D^*(R). \quad (37)$$

1230 But from (34)–(35),

$$1232 D^*(R) = \min_{R_t + R_f = R} (D_t^*(R_t) + D_f^*(R_f)) = D_{\text{prod}}^*(R). \quad (38)$$

1233 Therefore,

$$1235 D_{\text{mix}}^*(R) \geq D_{\text{prod}}^*(R), \quad (39)$$

1236 *Remark.* We acknowledge that theoretically, X_t and X_f are coupled via the Fourier Transform.
1237 However, within the context of Neural Vector Quantization, they behave as heterogeneous sources of
1238 information. For example, topological features in waveforms (e.g., K-complexes) and frequency den-
1239 sities in frequency (e.g., Alpha rhythms) impose orthogonal constraints on the codebook optimization
1240 landscape. Therefore, the “approximate independence” in Proposition 2.1 should be interpreted as
1241 the functional independence of semantic distortions in the latent representation space, rather than the
1242 statistical independence of the raw signals.

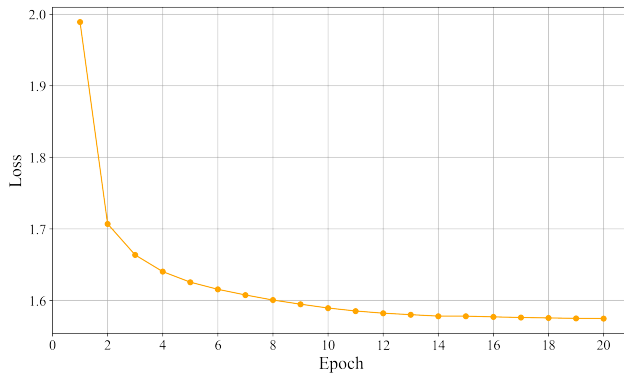
1242 E PRETRAINING RESULTS 1243

1244 Our model follows a two-stage pretraining framework. In the first stage, we train the TFDUAL-
1245 TOKENIZER, which independently tokenizes EEG signals in both the temporal and frequency domains.
1246 This tokenizer is optimized to reconstruct the original raw EEG signals, amplitude, and phase
1247 components, thereby producing discrete code representations with structural interpretability. In the
1248 second stage, we pretrain the EEGSSM encoder using a masked modeling objective: given the
1249 original EEG signals as input, the model learns to predict the corresponding masked tokens generated
1250 from the TFDUAL-TOKENIZER.

1251 This section reports the pretraining results of both stages, including loss convergence, reconstruction
1252 dynamics, and codebook utilization patterns.
1253

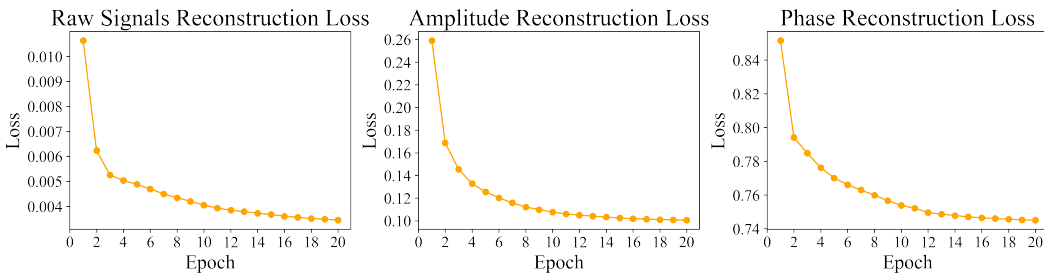
1254 E.1 TFDUAL-TOKENIZER PRETRAINING RESULTS 1255

1256 **Total Training Loss** The total pretraining loss curve of the TFDUAL-TOKENIZER is shown in
1257 Figure 11. The model demonstrates a rapid initial decrease in loss during the first few epochs,
1258 followed by a slower but consistent decline.



1272 Figure 11: Pretraining Loss Curve of TFDUAL-TOKENIZER.
1273

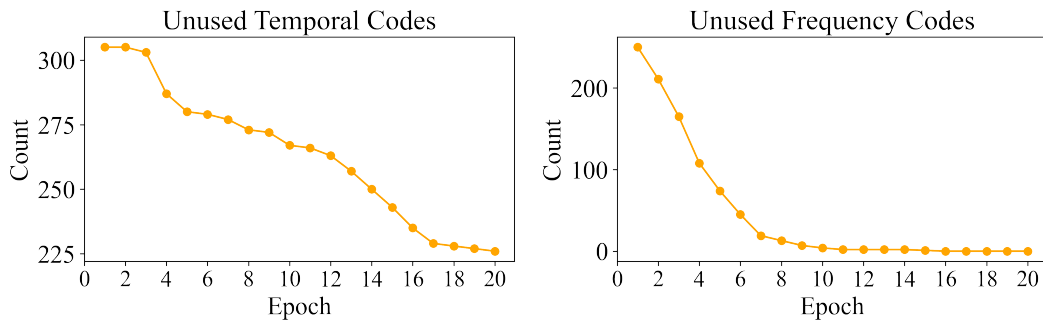
1274 **Reconstruction Loss.** We report the pretraining reconstruction loss of the TFDUAL-TOKENIZER in
1275 Figure 12. The temporal codebook is trained to reconstruct raw EEG signals in the time domain, while
1276 the frequency codebook is trained to reconstruct the corresponding amplitude and phase components
1277 in the frequency domain. All three loss curves exhibit a sharp initial decline, followed by a gradual
1278 convergence, indicating stable optimization.
1279



1291 Figure 12: Pretraining Loss Curve of TFDUAL-TOKENIZER.
1292

1293 **Unused Codes Analysis.** During pretraining, we track the number of unused codes in both the
1294 temporal and frequency codebooks of the TFDUAL-TOKENIZER, each with a size of 4096. As shown
1295 in Figure 13, the frequency codebook demonstrates a rapid decrease in unused codes, while the

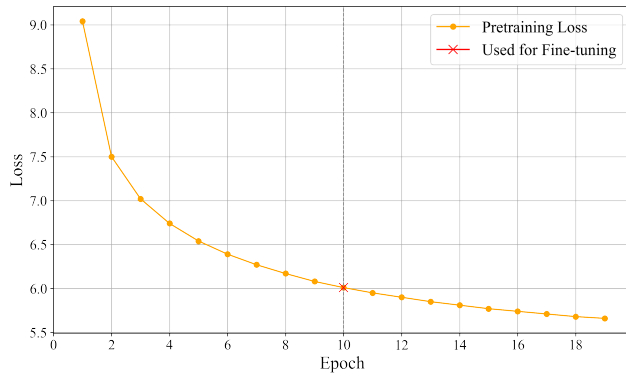
1296 temporal codebook shows a slower and more incremental reduction. A more detailed analysis of the
 1297 temporal-frequency complementarity is provided in Section B.3.
 1298



1300
 1301
 1302
 1303
 1304
 1305
 1306
 1307
 1308
 1309
 1310 Figure 13: Unused code dynamics of the TFDUAL-TOKENIZER.
 1311
 1312

1313 E.2 EEGSSM PRETRAINING RESULTS 1314

1315 We plot the pretraining loss curve of EEGSSM in Figure 14. We select epoch 10 as the checkpoint
 1316 for downstream fine-tuning. We observe that the pretraining loss of EEGSSM decreases rapidly
 1317 from epoch 1 to 6 (9.04 → 6.39), then flattens gradually after epoch 10 (6.01 → 5.66). Using epoch
 1318 10 for fine-tuning is a balance between representation strength and generalization. Overtraining on
 1319 EEG, prone to noise and inter-subject variability, can reduce transferability. Epoch 10 serves as a
 1320 conservative yet effective checkpoint. This practice is consistent with trends in foundation models
 1321 from NLP (Devlin et al., 2019) and vision (Caron et al., 2021), where mid-training checkpoints often
 1322 lead to better downstream performance than final ones due to reduced overfitting to the pretext task.
 1323



1324
 1325
 1326
 1327
 1328
 1329
 1330
 1331
 1332
 1333
 1334 Figure 14: Pretraining Loss Curve of EEGSSM.
 1335
 1336
 1337
 1338

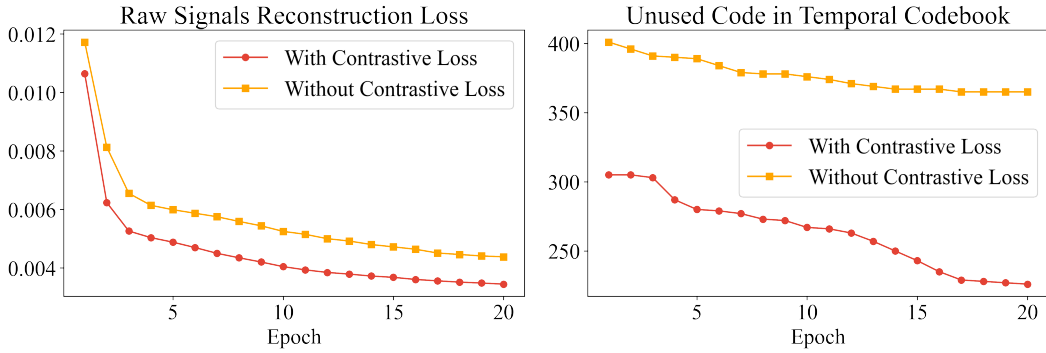
1339 F IMPROVING TEMPORAL CODEBOOK LEARNING VIA CONTRASTIVE LOSS 1340

1341 To improve the learning of the temporal codebook in our TFDUAL-TOKENIZER, we introduce a
 1342 contrastive loss as one of the objectives during pretraining. This design is motivated by observations
 1343 from prior work LaBraM (Jiang et al., 2024), where the authors report that reconstructing raw EEG
 1344 signals leads to unconvergence, and thus omit the temporal reconstruction objective entirely.

1345 To better understand this limitation, we first implemented a baseline reconstruction of raw signals
 1346 within the LaBraM framework and observed that the training loss plateaued at a high value (between
 1347 0.128 and 0.131), showing no convergence over training epochs. To mitigate this, we introduce a *TF-*
 1348 *Conv* module before the Transformer encoder, designed to extract temporal-frequency representations
 1349 before tokenization. While this stabilizes training to some extent, we still observe significant issues
 with code utilization and loss convergence. Therefore, we incorporate a lightweight contrastive loss,

1350 applied over temporal representations before quantization, to encourage the model to organize similar
1351 input patterns closer in the latent space. As shown in Figure 15, this improves the optimization of the
1352 reconstruction loss and reduces the number of unused temporal codes during training.

1353 These results demonstrate that contrastive regularization acts as an effective prior for stabilizing
1354 discrete token learning, particularly when reconstructing raw signals. It both improves convergence
1355 and mitigates codebook collapse in the temporal branch of the tokenizer.



1369
1370 Figure 15: Effect of Contrastive Loss on Temporal Codebook Learning.
1371

1372 G DATASET DESCRIPTION 1373

1374 We evaluate the CODEBRAIN across eight diverse downstream tasks covering ten publicly available
1375 EEG datasets. Notably, these datasets exhibit substantial variability in channel configurations
1376 (ranging from 6 to 64), sequence lengths (from 1s to 30s), and task complexities (2-class to 9-class),
1377 highlighting the versatility and robustness of CODEBRAIN across different EEG applications. The
1378 following sections describe each dataset in detail, including its task objective and data split strategy.
1379 A comprehensive analysis of each dataset is provided below.

1380 **Emotion Recognition.** We conduct emotion recognition experiments on two widely used EEG
1381 datasets: FACED (Chen et al., 2023) and SEED-V (Liu et al., 2021).

1382 The **FACED** dataset (Finer-Grained Affective Computing EEG Dataset) is a large-scale EEG dataset
1383 proposed by Chen et al. (Chen et al., 2023) for emotion recognition tasks. It consists of 32-channel
1384 EEG recordings sampled at 250 Hz from 123 participants, each exposed to 28 video clips designed to
1385 elicit nine distinct emotional states: *amusement, inspiration, joy, tenderness, anger, fear, disgust,*
1386 *sadness, and neutral*. These cover both positive and negative affective categories. Each EEG trial
1387 is 10 seconds long and is subsequently resampled to 200 Hz, resulting in a total of 10,332 clean
1388 EEG segments. For fair comparison, we adopt the same subject-wise split as in (Wang et al., 2025):
1389 subjects 1–80 are used for training, 81–100 for validation, and 101–123 for testing, ensuring no
1390 subject overlap across splits and enabling evaluation of cross-subject generalization.

1391 The **SEED-V** (Liu et al., 2021) is an EEG dataset designed for emotion recognition, covering five
1392 emotional categories: *happy, sad, neutral, disgust, and fear*. It consists of 62-channel EEG recordings
1393 collected at 1000 Hz from 16 subjects, each participating in three sessions. Each session includes 15
1394 trials, which are evenly divided into training, validation, and test sets (5 trials each). The EEG signals
1395 are segmented into 1-second windows, yielding a total of 117,744 samples, and resampled to 200 Hz
1396 for consistency. The dataset provides rich temporal structure and inter-subject variability, making it a
1397 strong benchmark for evaluating generalization in emotion-related EEG modeling.

1398 **Sleep Staging.** We use two datasets, **ISRU****C_S1** and **ISRU****C_S3** (Khalighi et al., 2016), for sleep
1399 stage classification. Both datasets are annotated according to the American Academy of Sleep
1400 Medicine (AASM) standard (Berry et al., 2012), with five sleep stages: *Wake, NREM1 (N1), NREM*
1401 (*N2*), *NREM (N3)*, and *REM*. Each EEG segment corresponds to a 30-second epoch.

1402 **ISRU****C_S1** includes EEG recordings from 100 subjects using six channels at a sampling rate of
1403 200 Hz. We adopt a subject-wise split, with 80 subjects for training, 10 for validation, and 10 for
1404 testing. As the transition rules between sleep stages carry important temporal patterns, we follow

1404 prior work (Wang et al., 2024a; 2025) and insert a Transformer layer on top of the projection head
1405 during fine-tuning to better capture sequence-level dependencies. We set the input sequence length to
1406 20, and discard segments that cannot be evenly divided. In total, 86,320 labeled samples are retained.
1407 **ISRUC-S3** is a smaller dataset comprising recordings from 10 subjects, also sampled at 200 Hz with
1408 six channels, totaling 8,500 labeled segments. We follow an 8:1:1 subject-wise split for training,
1409 validation, and testing.

1410
1411 **Imagined Speech Classification.** The **BCIC2020-T3** dataset (Jeong et al., 2022) was released
1412 as part of the 2020 International Brain–Computer Interface Competition and focuses on imagined
1413 speech decoding. It contains EEG recordings from 15 participants who were instructed to silently
1414 imagine speaking five specific words or phrases, “hello”, “help me”, “stop”, “thank you”, and
1415 “yes”. EEG signals were collected using 64 scalp channels at a sampling rate of 256 Hz and were
1416 subsequently resampled to 200 Hz for preprocessing consistency. Each subject completed 80 trials
1417 per class, resulting in a total of 6,000 trials. The dataset provides predefined training, validation, and
1418 test splits, with 60, 10, and 10 trials per class, respectively, facilitating fair model evaluation like
1419 existing baselines (Wang et al., 2025).
1420

1421 **Mental Stress Detection.** The **Mental Arithmetic** dataset (Mumtaz, 2016) supports the task of
1422 mental stress detection using EEG signals. It contains recordings from 36 subjects under two distinct
1423 cognitive conditions: *resting* and *active engagement* in mental arithmetic. EEG data labeled as “no
1424 stress” correspond to resting periods prior to the task, while “stress” labels are assigned to recordings
1425 during task performance. The signals were acquired using 20 electrodes placed according to the
1426 international 10–20 system, with an original sampling rate of 500 Hz. For consistency, the signals are
1427 resampled to 200 Hz and band-pass filtered between 0.5–45 Hz to suppress noise. Each recording is
1428 segmented into 5-second windows, yielding a total of 1,707 samples. We adopt a subject-wise split
1429 for fair evaluation with existing baselines (Wang et al., 2025): subjects 1–28 for training, 29–32 for
1430 validation, and 33–36 for testing.

1431 **Seizure Detection.** The **CHB-MIT** dataset (Shoeb, 2009) is a widely used benchmark for seizure
1432 detection from EEG signals. It contains long-term EEG recordings from 23 patients diagnosed with
1433 intractable epilepsy, collected at the Children’s Hospital Boston. The subjects underwent continuous
1434 monitoring over several days, during which seizures were recorded following the tapering of anti-
1435 epileptic medications. EEG signals were acquired using the international 10–20 system and originally
1436 sampled at 256 Hz. In our setting, we adopt 16 channels commonly used in prior work (Yang
1437 et al., 2023; Wang et al., 2025), resample all signals to 200 Hz, and segment them into 10-second
1438 non-overlapping windows, yielding 326,993 labeled samples across seizure and non-seizure classes.
1439 We follow a subject-wise split: subjects 1–19 for training, 20–21 for validation, and 22–23 for testing.
1440 Notably, this dataset is highly imbalanced, with seizure events constituting only a small fraction of
1441 the total samples, posing significant challenges for model training and evaluation.

1442 **Motor Imagery Classification.** The **SHU-MI** dataset (Goldberger et al., 2000) is designed for
1443 binary motor imagery classification, where participants are instructed to imagine movements of either
1444 the *left or right hand*. EEG signals were recorded from 25 subjects using a 32-channel setup at an
1445 original sampling rate of 250 Hz. To ensure consistency with the pre-training setting, all signals are
1446 resampled to 200 Hz and segmented into 4-second non-overlapping windows, resulting in 11,988
1447 labeled samples. A subject-wise split is applied for fair model evaluation like existing baselines
1448 (Wang et al., 2025), with subjects 1–15 used for training, 16–20 for validation, and 21–25 for testing.
1449 This dataset supports the development of BCI systems that decode motor intentions from brain
1450 activity without actual movement.

1451 **Event Type Classification.** The **TUEV** dataset (Obeid & Picone, 2016) is a clinically annotated
1452 EEG corpus used for multi-class event type classification. It includes six event categories: *spike*
1453 and *sharp wave (SPSW)*, *generalized periodic epileptiform discharges (GPED)*, *periodic lateralized*
1454 *epileptiform discharges (PLED)*, *eye movements (EYEM)*, *artifacts (ARTF)*, and *background activity*
1455 (*BCKG*). EEG signals were originally recorded at 256 Hz using 23 channels. In line with prior work
1456 (Wang et al., 2025), we preprocess the data by selecting 16 bipolar montage channels based on the
1457 international 10–20 system. The signals are band-pass filtered between 0.3–75 Hz to suppress low-
1458 and high-frequency noise, and a 60 Hz notch filter is applied to eliminate power line interference. All

1458 recordings are resampled to 200 Hz and segmented into 5-second windows, yielding 112,491 labeled
1459 samples. We follow the official train-test split and further divide the training subjects into training
1460 and validation sets in an 8:2 ratio, consistent with established benchmarks.
1461

1462 **Abnormal Detection.** The **TUAB** dataset (Obeid & Picone, 2016) is employed for binary abnormal
1463 EEG detection, where each EEG recording is labeled as either *normal* or *abnormal* based on clinical
1464 interpretation. Originally recorded at 256 Hz using 23 channels, the dataset provides large-scale
1465 EEG recordings suitable for evaluating diagnostic models. To ensure fair comparison with prior
1466 work (Wang et al., 2025), we follow a similar preprocessing protocol. Specifically, we select 16
1467 bipolar montage channels following the international 10–20 system, apply band-pass filtering between
1468 0.3–75 Hz to eliminate low- and high-frequency artifacts, and remove 60 Hz power line interference
1469 using a notch filter. The EEG signals are then resampled to 200 Hz and segmented into 10-second
1470 windows, resulting in 409,455 labeled samples. We follow the official train-test split and further
1471 divide the training set into training and validation subsets using an 8:2 subject-wise ratio, consistent
1472 with existing benchmarks.
1473

H BASELINES AND METRICS DESCRIPTION

H.1 METRICS

1477 To comprehensively evaluate our model, we compare it with a set of strong baselines commonly used
1478 in EEG analysis. These baselines are evaluated using metrics tailored for class-imbalanced scenarios,
1479 which are prevalent in EEG datasets. The metrics include:
1480

- 1481 • **Balanced Accuracy**, which averages the recall across all classes and is particularly suitable
1482 for imbalanced multi-class classification tasks.
- 1483 • **AUROC** and **AUC-PR**, which assess the performance of binary classifiers under different
1484 thresholds. While AUROC measures the trade-off between sensitivity and specificity,
1485 AUC-PR focuses on precision-recall trade-offs, especially informative under severe class
1486 imbalance.
- 1487 • **Cohen’s Kappa**, which quantifies inter-class agreement beyond chance and is employed as
1488 the primary metric for multi-class classification.
- 1489 • **Weighted F1 Score**, which combines precision and recall while adjusting for class support,
1490 ensuring fair performance measurement across imbalanced datasets.

1491 For model selection and comparison, AUROC is used as the main evaluation metric for binary
1492 classification tasks, and Cohen’s Kappa is used for multi-class scenarios.
1493

H.2 BASELINES

1496 We compare our CODEBRAIN model against a comprehensive set of baseline models [that include](#)
1497 [widely used task-specific models](#), as well as publicly available EEG foundation models.
1498

EEGNet (Lawhern et al., 2018): EEGNet is a compact convolutional neural network specifically
1499 designed for EEG-based BCI tasks. It adopts depthwise-separable convolutions to disentangle
1500 temporal filtering and spatial pattern learning, enabling efficient parameter usage while preserving
1501 discriminative EEG features.

EEGConformer (Song et al., 2022): EEGConformer integrates convolutional front-ends with
1503 Transformer blocks to jointly capture local temporal dynamics and longer-range dependencies.
1504 Its convolution modules extract short-term EEG patterns, while the attention mechanism models
1505 cross-channel and cross-time interactions.

ContraWR (Yang et al., 2021): ContraWR is a self-supervised representation learning framework
1508 that uses contrastive learning with a weakly-supervised relational task. By contrasting EEG segments
1509 from the same versus different contexts, the model learns invariant temporal representations without
1510 relying on explicit labels.

ST-Transformer (Song et al., 2021): ST-Transformer applies Transformer attention to EEG by
1511 factorizing spatial and temporal modeling. It processes EEG as a structured sequence across both

1512 dimensions, where attention layers capture inter-channel relationships as well as time-varying depen-
1513 dencies.

1514 We also compare CODEBRAIN against 5 publicly available EFM_s that have released pre-trained
1515 weights, covering a diverse set of pretraining strategies to evaluate the effectiveness of different
1516 foundation model designs and pretraining paradigms under comparable settings.

1517 **BENDR** (Kostas et al., 2021): We adopted **BENDR (Bert-inspired Neural Data Representations)** as
1518 our baseline model, as introduced by Kostas et al. BENDR is a pioneering deep learning architecture
1519 for Electroencephalography (EEG) data, leveraging transformers and a contrastive self-supervised
1520 learning task. This approach enables the model to learn meaningful representations from vast amounts
1521 of unlabeled EEG data.

1522 **BIOT** (Yang et al., 2023): **BIOT (Biosignal Transformer for Cross-data Learning in the Wild)** is
1523 a transformer-based architecture designed to handle cross-dataset EEG signal classification under
1524 domain shifts. It leverages a domain-invariant attention mechanism and contrastive representation
1525 learning to enhance generalization across different recording conditions and subject populations.

1526 **LaBraM**(Jiang et al., 2024): **LaBraM (Large Brain Model)** proposes a scalable transformer-based
1527 framework designed to learn generic EEG representations from large-scale brain signal datasets. By
1528 pretraining on a diverse corpus of EEG recordings, the model captures rich temporal and spatial
1529 features that transfer effectively to various downstream BCI tasks. The architecture incorporates
1530 efficient self-attention mechanisms and task-specific adapters to support flexible fine-tuning.

1531 **EEGPT** (Wang et al., 2024a): **EEGPT** employs a dual self-supervised learning strategy that combines
1532 masked autoencoding with spatial-temporal representation alignment, enhancing feature quality by
1533 focusing on high signal-to-noise ratio (SNR) representations rather than raw signals. The model’s hi-
1534 erarchical architecture decouples spatial and temporal processing, improving computational efficiency
1535 and adaptability to various brain-computer interface (BCI) applications.

1536 **CBraMod** (Wang et al., 2025): **CBraMod (Criss-Cross Brain Foundation Model)** is a transformer-
1537 based EEG foundation model that addresses the heterogeneous spatial and temporal dependencies
1538 inherent in EEG signals. It introduces a criss-cross transformer architecture comprising parallel
1539 spatial and temporal attention mechanisms, enabling separate yet simultaneous modeling of spatial
1540 and temporal relationships.

1541

1542 I HYPERPARAMETER SETTING

1543

1544 We provide detailed hyperparameter configurations for the two-stage pretraining of our CODEBRAIN
1545 model and the fine-tuning settings across ten downstream tasks.

1546

1547 I.1 PRETRAINING SETTINGS

1548

The pretraining process consists of two stages:

1549

- 1550 1. Training the TFDUAL-TOKENIZER
- 1551 2. Training the EEGSSM

1552

The hyperparameters used in each stage are summarized in Table 5 and Table 6, respectively.

1553

1554 I.2 PARAMETERS OF EEGSSM

1555

The model architecture parameters used in EEGSSM during pre-training are shown in Table 7.

1556

1557 I.3 FINE-TUNING SETTINGS ON DOWNSTREAM TASKS

1558

1559 The CODEBRAIN model is fine-tuned on ten downstream EEG classification tasks, each with task-
1560 specific hyperparameters. Following the general strategy adopted by prior EFM_s, we adopt a
1561 lightweight three-layer MLP as the probe head for all downstream tasks and fine-tune the entire model
1562 end-to-end. Table 8 lists the fine-tuning configurations including learning rate, weight decay, dropout

1566
1567
1568
1569
1570
1571
1572
1573
1574
1575
1576
1577
1578
1579
1580
1581
1582
1583
1584
1585
1586
1587
1588
1589
1590
1591
1592
1593
1594
1595
1596
1597
1598
1599
1600
1601
1602
1603
1604
1605
1606
1607
1608
1609
1610
1611
1612
1613
1614
1615
1616
1617
1618
1619

Table 5: Hyperparameters for TFDUAL-TOKENIZER.

Hyperparameters	Values
TFConv	
Input channels	$\{1, 8, 4\}$
Output channels	$\{8, 4, 4\}$
Kernel size	$\{(1, 15), (1, 3), (1, 3)\}$
Stride	$\{(1, 8), (1, 1), (1, 1)\}$
Padding	$\{(0, 7), (0, 1), (0, 1)\}$
Transformer encoder layers	12
Transformer decoder layers	3
Hidden size	200
MLP size	800
Attention head number	8
Temporal Codebook size	4096×32
Frequency Codebook size	4096×32
Codebook initialization	Random init + L^2 normalization
Batch size	256
Peak learning rate	1e-4
Minimal learning rate	1e-5
Learning rate scheduler	Cosine
Optimizer	AdamW
Adam β	(0.9, 0.99)
Weight decay	1e-4
Warm-up steps	5
Total epochs	20
Data stride	200
Contrastive temperature (τ)	0.5

1595
1596
1597
1598
1599
1600
1601
1602
1603
1604
1605
1606
1607
1608
1609
1610
1611
1612
1613
1614
1615
1616
1617
1618
1619

Table 6: Hyperparameters of Pre-training.

Hyperparameters	Values
Epochs	10
Batch size	256
Dropout	0.1
Optimizer	Adam
Learning rate	1e-4
Adam β	(0.9, 0.999)
Adam ϵ	1e-8
Weight decay	5e-3
Scheduler	CosineAnnealingLR
Minimal learning rate	1e-5
Clipping gradient norm	5

rate, and batch size for each task. For sleep staging tasks, due to their strong temporal structure, we follow prior work (Wang et al., 2024a; 2025) and insert an additional Transformer encoder on top of the projection head to jointly model the sequence of 20 consecutive EEG segments. This enables the model to capture inter-epoch transitions critical to sleep stage classification.

J ADDITIONAL EVALUATION ON OTHER BCI TASKS

We report the performance of CODEBRAIN on four additional EEG datasets not included in the main text, covering diverse domains of sleep staging, motor imagery, event detection, and abnormality

Table 7: Configuration of EEGSSM	
Parameters	Values
Input size	200
Hidden dimension	200
Output size	200
Number of layers	8
Max sequence length	570
SGConv state	64
SGConv bidirectional	True
Layer normalization	True
Sliding window attention length	1s

Table 8: Fine-tuning Hyperparameters for Downstream Tasks.

Dataset	Learning Rate	Weight Decay	Dropout	Batch Size
FACED	5e-5	5e-4	0.1	16
SEED-V	5e-5	1e-2	0.1	64
ISRUC_S1	1e-4	1e-1	0.2	48
ISRUC_S3	1e-4	1e-1	0.2	48
BCIC2020-T3	5e-5	5e-2	0.1	32
Mental Arithmetic	3e-5	1e-3	0.1	32
CHB-MIT	3e-5	1e-2	0.4	64
SHU-MI	5e-5	5e-3	0.3	64
TUEV	2e-5	5e-4	0.3	64
TUAB	1e-5	5e-5	0.4	512

classification in Tables 9 to 12. These allow us to assess the cross-domain generalization ability of our pretrained model beyond the main text.

We note that both TUAB and TUEV originate from the TUH EEG corpus (Obeid & Picone, 2016), which overlaps with our pretraining source (TUEG). To avoid overfitting to this distribution and promote generalization, we stop pretraining at epoch 10 as discussed in Section E.2. While this may limit gains on TUH datasets compared to previous EFM, such as CBraMod (trained for 40 epochs in the same pretraining dataset) (Wang et al., 2025), CODEBRAIN still achieves superior or competitive results.

ISRUC_S1 As shown in Table 9, CODEBRAIN achieves state-of-the-art performance on ISRUC_S1 in terms of Cohen’s Kappa (0.7476) and Weighted F1 (0.8020), slightly surpassing CBraMod (Wang et al., 2025) by +0.34 and +0.09 points, respectively. Its Balanced Accuracy of 0.7835 is also competitive, trailing the best result by only -0.30. These results highlight the model’s ability to capture temporal dependencies and learn discriminative representations for 5-class sleep staging under a cross-subject setting.

SHU-MI As shown in Table 10, CODEBRAIN achieves the best overall performance on SHU-MI across all three metrics. It obtains an AUROC of 0.7124 and an AUC-PR of 0.7166, slightly improving over the previous best by +1.36 and +0.27 points, respectively. For Balanced Accuracy, it reaches 0.6431 (+0.61), with notably lower variance. These results underscore its strong generalization to motor imagery decoding under a cross-subject protocol.

TUEV As shown in Table 11, CODEBRAIN achieves the highest Cohen’s Kappa (0.6912, an improvement of +0.0140 over the best baseline (Wang et al., 2025)) and Weighted F1 (0.8362) on TUEV. Although its Balanced Accuracy is lower than CBraMod (Wang et al., 2025), we attribute this to reduced sensitivity on the rare *SPSW* class. Since TUEV shares distributional overlap with our pretraining source (TUEG), we stop pretraining at epoch 10 to prevent overfitting, unlike CBraMod’s 40-epoch training as discussed in subsection E.2. We also report LaBraM’s results based on its original

1674

1675

Table 9: Performance Comparison on the ISURC_S1 (5-Class) dataset.

Methods	Cohen’s Kappa	Weighted F1	Balanced Accuracy
EEGNet	0.7040 ± 0.0173	0.7513 ± 0.0124	0.7154 ± 0.0121
EEGConformer	0.7143 ± 0.0162	0.7634 ± 0.0151	0.7400 ± 0.0133
ContraWR	0.7178 ± 0.0156	0.7610 ± 0.0137	0.7402 ± 0.0126
ST-Transformer	0.7013 ± 0.0352	0.7681 ± 0.0175	0.7381 ± 0.0205
BENDRKostas et al. (2021)	0.6956 ± 0.0053	0.7569 ± 0.0049	0.7401 ± 0.0056
BIOTYang et al. (2023)	0.7192 ± 0.0231	0.7790 ± 0.0146	0.7527 ± 0.0121
LaBraMJiang et al. (2024)	0.7231 ± 0.0182	0.7810 ± 0.0133	0.7633 ± 0.0102
EEGPTWang et al. (2024a)	0.2223 ± 0.0227	0.3111 ± 0.0110	0.4012 ± 0.0177
CBraModWang et al. (2025)	0.7442 ± 0.0152	0.8011 ± 0.0099	0.7865 ± 0.0110
CodeBrain	0.7476 ± 0.0040	0.8020 ± 0.0018	0.7835 ± 0.0033

1689

1690

Table 10: Performance Comparison on the SHU-MI (2-Class) dataset.

Methods	AUROC	AUC-PR	Balanced Accuracy
EEGNet	0.6283 ± 0.0152	0.6311 ± 0.0142	0.5889 ± 0.0177
EEGConformer	0.6351 ± 0.0101	0.6370 ± 0.0093	0.5900 ± 0.0107
ContraWR	0.6273 ± 0.0113	0.6315 ± 0.0105	0.5873 ± 0.0128
ST-Transformer	0.6431 ± 0.0111	0.6394 ± 0.0122	0.5992 ± 0.0206
BENDRKostas et al. (2021)	0.5863 ± 0.0280	0.5853 ± 0.0268	0.5573 ± 0.0227
BIOTYang et al. (2023)	0.6609 ± 0.0127	0.6770 ± 0.0119	0.6179 ± 0.0183
LaBraMJiang et al. (2024)	0.6604 ± 0.0091	0.6761 ± 0.0083	0.6166 ± 0.0192
EEGPTWang et al. (2024a)	0.6241 ± 0.0071	0.6266 ± 0.0133	0.5778 ± 0.0162
CBraModWang et al. (2025)	0.6988 ± 0.0068	0.7139 ± 0.0088	0.6370 ± 0.0151
CodeBrain	0.7124 ± 0.0050	0.7166 ± 0.0106	0.6431 ± 0.0066

1705

1706

23-channel setting (Jiang et al., 2024), while CODEBRAIN follows the 16-channel configuration used in CBraMod. Similarly, EEGPT (Wang et al., 2024a) does not adopt a linear fine-tuning protocol but applies two convolutional layers before entering the foundation model, followed by an MLP head. While such architectural choices may enhance performance, we follow their respective fine-tuning settings. In addition, following the experimental setup of CBraMod, we also report the results of experiments conducted by removing all TUEV and TUAB samples from the TUEG dataset. It can be seen that although our model’s performance slightly declined on TUEV, it still surpassed other baselines. In such cases, CODEBRAIN still outperforming both LaBraM and EEGPT under their own fine-tuning settings clearly demonstrates the robustness of our approach.

1716

1717

TUAB As shown in Table 12, CODEBRAIN achieves the highest Balanced Accuracy (0.8294) on TUAB, slightly outperforming CBraMod (Wang et al., 2025). Similar to TUEV, TUAB is part of the TUH EEG corpus family (Obeid & Picone, 2016) and thus closely aligned with our pretraining source (TUEG). As discussed in subsection E.2, we adopt an early stopping strategy at epoch 10 to mitigate overfitting to this distribution, which may partly account for the slightly lower AUROC and AUC-PR compared to CBraMod, trained for 40 epochs on the same dataset. While LaBraM leverages a 23-channel montage (Jiang et al., 2024) and EEGPT (Wang et al., 2024a) employs two convolutional layers before the foundation model, we retain their respective fine-tuning protocols for comparison. In addition, the impact of duplicate data in the pre-training set on our model is smaller on the TUAB dataset, and in some experiments it can even surpass situations without leaking. This may be due to the larger size of the TUAB dataset. Despite these potentially stronger configurations, CODEBRAIN still exceeds both models under their own settings, highlighting its strong and consistent generalization.

1728

1729

Table 11: Performance Comparison on the TUEV (6-Class) dataset.

Methods	Cohen’s Kappa	Weighted F1	Balanced Accuracy
EEGNet	0.3577 ± 0.0155	0.6539 ± 0.0120	0.3876 ± 0.0143
EEGConformer	0.3967 ± 0.0195	0.6983 ± 0.0152	0.4074 ± 0.0164
ContraWR	0.3912 ± 0.0237	0.6893 ± 0.0136	0.4384 ± 0.0349
ST-Transformer	0.3765 ± 0.0306	0.6823 ± 0.0190	0.3984 ± 0.0228
BENDRKostas et al. (2021)	0.4271 ± 0.0238	0.6755 ± 0.0216	0.4363 ± 0.0245
BIOTYang et al. (2023)	0.5273 ± 0.0249	0.7492 ± 0.0082	0.5281 ± 0.0225
LaBraMJiang et al. (2024)	0.6637 ± 0.0093	0.8312 ± 0.0052	0.6409 ± 0.0065
EEGPTWang et al. (2024a)	0.6351 ± 0.0134	0.8187 ± 0.0063	0.6232 ± 0.0114
CBraModWang et al. (2025)	0.6772 ± 0.0096	0.8342 ± 0.0064	0.6671 ± 0.0107
CodeBrain (Excluding)	0.6838 ± 0.0291	0.8293 ± 0.0163	0.6375 ± 0.0182
CodeBrain	0.6912 ± 0.0101	0.8362 ± 0.0048	0.6428 ± 0.0062

1745

1746

Table 12: Performance Comparison on the TUAB (2-Class) dataset.

Methods	Balanced Accuracy	AUC-PR	AUROC
EEGNet	0.7642 ± 0.0036	0.8299 ± 0.0043	0.8412 ± 0.0031
EEGConformer	0.7758 ± 0.0049	0.8427 ± 0.0054	0.8445 ± 0.0038
ContraWR	0.7746 ± 0.0041	0.8421 ± 0.0104	0.8456 ± 0.0074
ST-Transformer	0.7966 ± 0.0023	0.8521 ± 0.0026	0.8707 ± 0.0019
BENDRKostas et al. (2021)	0.7714 ± 0.0248	0.8412 ± 0.0215	0.8426 ± 0.0237
BIOTYang et al. (2023)	0.7959 ± 0.0057	0.8792 ± 0.0023	0.8815 ± 0.0043
LaBraMJiang et al. (2024)	0.8140 ± 0.0019	0.8965 ± 0.0016	0.9022 ± 0.0009
EEGPTWang et al. (2024a)	0.8038 ± 0.0040	0.8891 ± 0.0018	0.8811 ± 0.0015
CBraModWang et al. (2025)	0.8289 ± 0.0022	0.9258 ± 0.0008	0.9227 ± 0.0011
CodeBrain (Excluding)	0.8288 ± 0.0064	0.9061 ± 0.0039	0.9012 ± 0.0020
CodeBrain	0.8294 ± 0.0013	0.9100 ± 0.0006	0.9030 ± 0.0009

1763

1764

K ABLATION ON DESIGN CHOICES

1765

1766

K.1 ABLATION ON MASK RATIO

1767

We conduct an ablation study to investigate the effect of the mask ratio in the EEGSSM pretraining framework. As shown in Tables 13–15 and Figure 16, downstream performance consistently exhibits a U-shaped trend with respect to the masking ratio across all three datasets: FACED, SEED-V, and ISRUC-S3. Moderate masking (e.g., ratios around 0.4–0.6) leads to optimal performance, whereas excessively low (e.g., 0.1) or high (e.g., 0.9) ratios degrade generalization.

1773

1774

1775

1776

1777

1778

1779

1780

1781

To further illustrate this pattern, we visualize the training loss curves across different mask ratios in Figure 17. Interestingly, higher mask ratios result in slower convergence and higher final training loss, which is expected due to the increased difficulty of the reconstruction task. In contrast, lower mask ratios lead to faster and smoother loss reduction, but do not necessarily yield better downstream performance. This observation suggests a possible *optimization-vs-generalization trade-off*: easier pretext tasks (low mask ratio) are more optimizable but may encourage the model to learn shortcut solutions with limited generalizability, while overly difficult tasks (high mask ratio) may hinder effective representation learning due to insufficient learning signal. Moderate masking strikes a balance by being sufficiently challenging to promote abstraction, while still being learnable, thereby facilitating better generalization across downstream tasks.

1782
1783
1784
1785 Table 13: Performance of CODEBRAIN on FACED Dataset under Different Mask Ratios.
1786
1787

Mask Ratio	Cohen's Kappa	Weighted F1	Balanced Accuracy
0.1	0.5184 \pm 0.0039	0.5746 \pm 0.0158	0.5692 \pm 0.0064
0.2	0.5239 \pm 0.0036	0.5834 \pm 0.0071	0.5821 \pm 0.0040
0.3	0.5327 \pm 0.0100	0.5859 \pm 0.0036	0.5836 \pm 0.0076
0.4	0.5391 \pm 0.0045	0.5938 \pm 0.0057	0.5904 \pm 0.0058
0.5	0.5406 \pm 0.0084	0.5953 \pm 0.0113	0.5941 \pm 0.0098
0.6	0.5295 \pm 0.0075	0.5822 \pm 0.0090	0.5793 \pm 0.0112
0.7	0.5242 \pm 0.0077	0.5800 \pm 0.0065	0.5744 \pm 0.0096
0.8	0.5157 \pm 0.0065	0.5564 \pm 0.0067	0.5528 \pm 0.0040
0.9	0.5034 \pm 0.0078	0.5457 \pm 0.0084	0.5451 \pm 0.0114

1798
1799
1800
1801
1802
1803 Table 14: Performance of CODEBRAIN on SEED-V Dataset under Different Mask Ratios.
1804
1805

Mask Ratio	Cohen's Kappa	Weighted F1	Balanced Accuracy
0.1	0.2523 \pm 0.0051	0.4081 \pm 0.0030	0.3968 \pm 0.0031
0.2	0.2633 \pm 0.0033	0.4137 \pm 0.0027	0.4071 \pm 0.0035
0.3	0.2703 \pm 0.0043	0.4200 \pm 0.0048	0.4121 \pm 0.0041
0.4	0.2734 \pm 0.0042	0.4244 \pm 0.0029	0.4142 \pm 0.0055
0.5	0.2735 \pm 0.0032	0.4235 \pm 0.0022	0.4137 \pm 0.0023
0.6	0.2699 \pm 0.0041	0.4207 \pm 0.0059	0.4106 \pm 0.0048
0.7	0.2642 \pm 0.0045	0.4158 \pm 0.0033	0.4091 \pm 0.0040
0.8	0.2603 \pm 0.0031	0.4116 \pm 0.0041	0.4009 \pm 0.0025
0.9	0.2534 \pm 0.0036	0.4085 \pm 0.0024	0.3993 \pm 0.0055

1816
1817
1818
1819
1820
1821
1822 Table 15: Performance of CODEBRAIN on ISRUC_S3 Dataset under Different Mask Ratios.
1823

Mask Ratio	Cohen's Kappa	Weighted F1	Balanced Accuracy
0.1	0.7252 \pm 0.0069	0.7865 \pm 0.0039	0.7686 \pm 0.0072
0.2	0.7403 \pm 0.0023	0.7982 \pm 0.0026	0.7752 \pm 0.0032
0.3	0.7501 \pm 0.0057	0.8013 \pm 0.0062	0.7766 \pm 0.0020
0.4	0.7608 \pm 0.0060	0.8168 \pm 0.0078	0.7846 \pm 0.0062
0.5	0.7671 \pm 0.0091	0.8202 \pm 0.0071	0.7856 \pm 0.0031
0.6	0.7661 \pm 0.0068	0.8219 \pm 0.0052	0.7826 \pm 0.0076
0.7	0.7577 \pm 0.0068	0.8161 \pm 0.0040	0.7782 \pm 0.0061
0.8	0.7471 \pm 0.0031	0.8090 \pm 0.0041	0.7658 \pm 0.0025
0.9	0.7504 \pm 0.0078	0.8125 \pm 0.0063	0.7668 \pm 0.0065

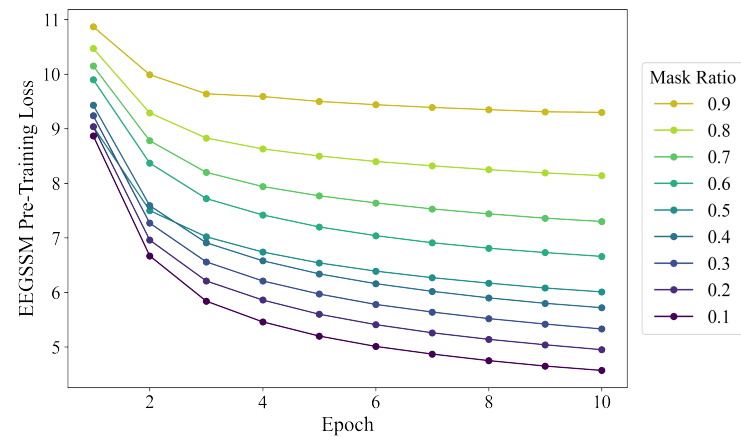
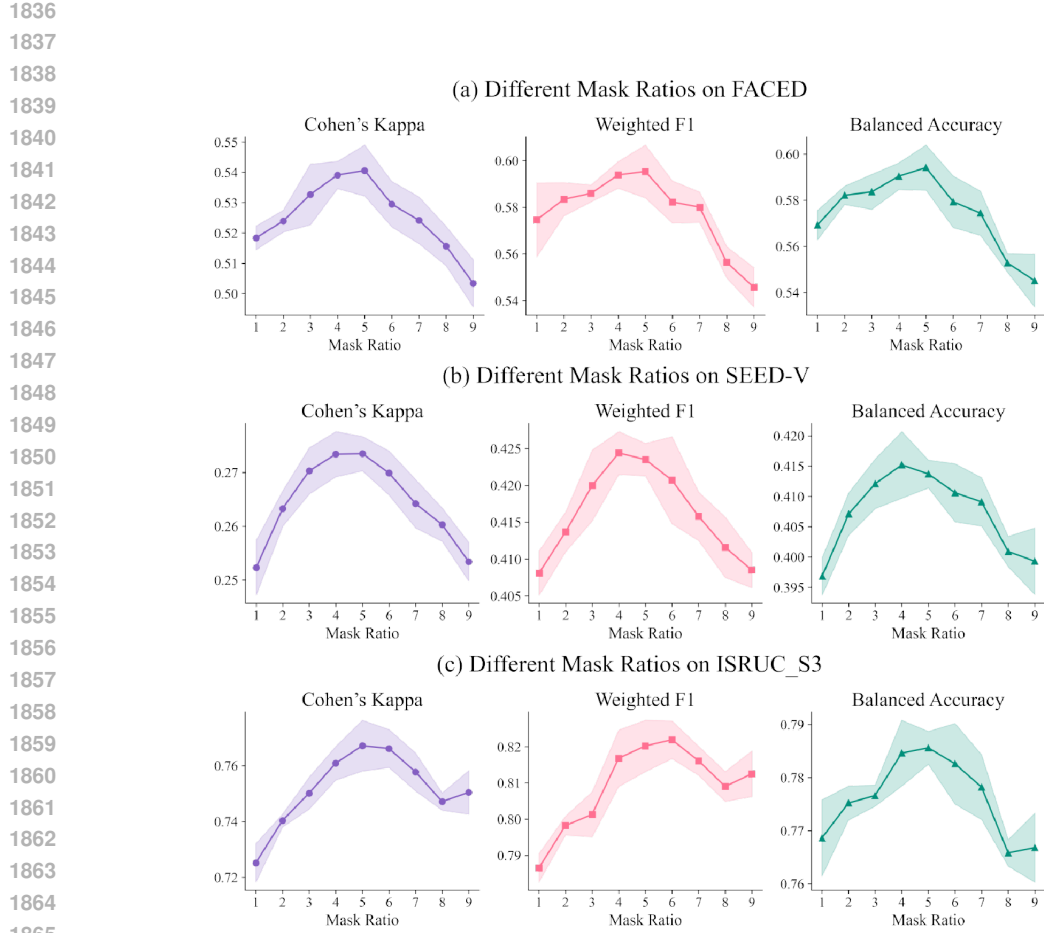


Figure 17: EEGSSM Pre-Training Loss Curve for Different Mask Ratios.

1890
1891

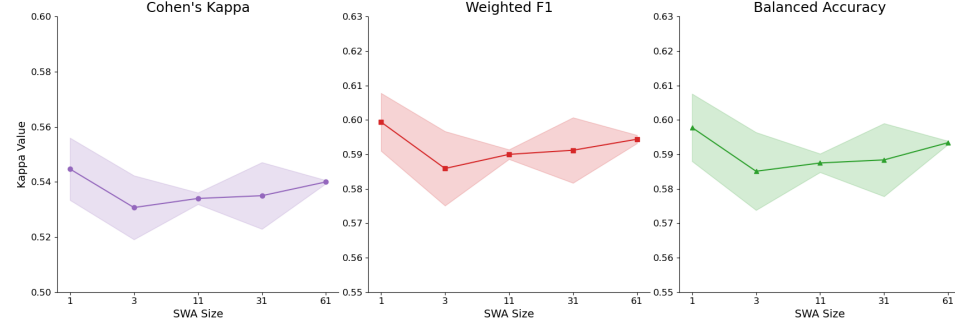
K.2 ABLATION ON SWA WINDOW SIZE

1892

We conduct an ablation study to investigate the effect of the SWA window size in the EEGSSM framework. The window size of SWA means the length of the segment observed by the attention mechanism in the SWA mechanism. Usually, the window size of SWA is an odd number because the model generally focuses not only on a single segment but also needs to observe features in adjacent segments. Therefore, its size is usually $2n + 1$, where n represents the length of SWA. As shown in Figure 18 and Figure 19, SWA window size = 1 achieved the best performance on both datasets among the 5 SWA window sizes. With the increase of the SWA window size, the SWA is close to self-attention. Therefore, as the SWA window size increases, the model's performance actually improves because more data will be involved in the attention calculation. When the SWA window size is 1, it is a special case where SWA only calculates for one second. This is equivalent to the model performing attention mechanism calculations within one second. Overall, SWA can help the model achieve a certain performance improvement.

1903

1904



1905

1906

1907

1908

1909

1910

1911

1912

1913

1914

1915

1916

Figure 18: Performance of different SWA window sizes on the FACED dataset.

1917

1918

1919

1920

1921

1922

1923

1924

1925

1926

1927

1928

1929

1930

1931

1932

1933

Figure 19: Performance of different SWA window sizes on the SEED-V dataset.

K.3 ABLATION ON CODEBOOK SIZE

1934

1935

1936

1937

1938

The size of the codebook is an important parameter; a codebook that is too large may lead to unstable training, while a codebook size that is too small may result in mixed information. Ideally, the codebook should maintain a small amount of unused codes but not be 0. We tested several combinations of different time-domain and frequency-domain codebook sizes to observe their unused codes during Tokenizer training.

1939

1940

1941

1942

1943

Table 16 shows the unused temporal codes and unused frequency codes under different codebook size combinations. When both the Temporal codebook size and Frequency codebook size are set to 2048, the unused frequency code is 0, indicating that there are duplicate frequency codes in the current codebook. When choosing a codebook size of 8192, the unused temporal codes reached 3401 and the unused frequency codes reached 1260, indicating that a large number of codes in the completed training codebook were not used. We ultimately selected 4096 for both. Although the frequency

1944 domain often yields richer representations, enlarging its codebook may increase reliance on it, so
 1945 we kept temporal and frequency codebooks equal. Considering capacity and utilization, 4096–4096
 1946 offers the best trade-off.

1947

1948

1949 Table 16: Temporal and frequency codebook statistics

1950 Temporal Codebook Size	1951 Frequency Codebook Size	1952 Unused Temporal Codes	1953 Unused Frequency Codes
1951 2048	1951 2048	1952 12	1953 0
1952 2048	1952 4096	1953 116	1954 0
1953 4096	1953 4096	1954 225	1955 165
1954 4096	1954 8192	1955 321	1956 931
1955 8192	1956 8192	1957 3401	1958 1260

1955

1956

1957 K.4 ABLATION ON PATCH SIZE

1958

1959 The size of the patch window is also an important adjustable parameter, which affects temporal
 1960 resolutions and masking strategies. To explore the impact of patch window size on the model, we
 1961 used window sizes ranging from 0.5s to 5s for complete two-stage pre-training and full-parameter
 1962 fine-tuning. Note that for some datasets where the patch size is larger than the channel length, such as
 1963 SEED-V, we pad the portion exceeding the available data to match the patch size in this experiment.

1964

1965 Table 17 and Table 18 show the performance of our method with different patch sizes on the SEED-V
 1966 dataset and ISRUC_3 dataset. Notably, in SEED-V, patch lengths longer than 1s require heavy
 1967 padding, causing large performance drops; in ISRUC_S3, the shortest 0.5s patches achieve the worst
 1968 performance, likely because they fragment key waveforms in sleep staging (e.g., Spindle ≥ 0.5 s).
 1969 From these results, the 1s setting is supported by two key considerations:

1970

1971 **Broad compatibility with downstream task.** 1s is a divisor of most downstream sequence lengths
 1972 (1–30s), minimizing padding and ensuring transferability. For example, on the SEED-V dataset,
 1973 if the patch size chosen by the model is greater than 1s, some methods (such as padding) need to
 1974 be adopted to enable model training. These methods may usually impair the model’s performance
 1975 because they introduce additional noise or increase computational load. EEG datasets with durations
 1976 less than 1 second are relatively rare, as most datasets have at least 1 second of data. If the data does
 1977 not exactly match the whole seconds, the cost of processing such a dataset is also relatively small.
 1978 Prior EEG foundation models (e.g., LaBram (Jiang et al., 2024), CBraMod (Wang et al., 2025)) also
 1979 adopt 1s patches for this reason.

1980

1981 **Semantic integrity.** Choosing a 1s patch length preserves the natural structure of EEG waveforms and
 1982 prevents semantic fragmentation. Many physiologically meaningful EEG events have characteristic
 1983 durations: for example, K-complexes are typically around 1s, spindles last 0.5–2s, and event-related
 1984 potentials such as P300 occur in the range of 0.3–0.6s. If patches are shorter than these characteristic
 1985 scales, the temporal branch of the TFDual-Tokenizer may only capture partial fragments of these
 1986 waveforms, leading to loss of semantic context.

1987

1988

1989

1990

1991

1992

1993

1994

1995

1996 K.5 ABLATION ON SGCONV KERNEL PARAMETERS

1998

1999 To justify the choice of the SGConv decay coefficient, we conduct a sensitivity analysis on three
 2000 representative downstream datasets (FACED, SEED-V, ISRUC_S3). The results are shown in Table 19

1998

1999

Table 18: Performance on ISRUC_3 with different patch sizes

Patch Length	Cohen’s Kappa	Weighted F1	Balanced Accuracy
0.5s	0.7405 \pm 0.0102	0.7950 \pm 0.0097	0.7420 \pm 0.0081
1s	0.7671\pm0.0091	0.8202\pm0.0071	0.7856\pm0.0031
2s	0.7592 \pm 0.0079	0.8113 \pm 0.0081	0.7753 \pm 0.0087
5s	0.7601 \pm 0.0075	0.8096 \pm 0.0074	0.7791 \pm 0.0096

2000

2001

2002

2003

2004

2005

2006

2007

2008

Table 19: Sensitivity analysis of the SGConv decay coefficient α across three downstream datasets.

SEED-V	Cohen’s Kappa	Weighted F1	Balanced Accuracy
$\alpha = 0.5$ (default)	0.2735 \pm 0.0032	0.4235 \pm 0.0022	0.4137 \pm 0.0023
$\alpha = 0.1$	0.2629 \pm 0.0017	0.4159 \pm 0.0006	0.4044 \pm 0.0017
$\alpha = 0.9$	0.2318 \pm 0.0074	0.3851 \pm 0.0141	0.3819 \pm 0.0046
$\alpha = 2.0$	0.2332 \pm 0.0077	0.3851 \pm 0.0090	0.3809 \pm 0.0069
FACED	Cohen’s Kappa	Weighted F1	Balanced Accuracy
$\alpha = 0.5$ (default)	0.5406 \pm 0.0084	0.5953 \pm 0.0113	0.5941 \pm 0.0090
$\alpha = 0.1$	0.5295 \pm 0.0080	0.5853 \pm 0.0074	0.5839 \pm 0.0069
$\alpha = 0.9$	0.4681 \pm 0.0069	0.5270 \pm 0.0065	0.5314 \pm 0.0050
$\alpha = 2.0$	0.4782 \pm 0.0037	0.5282 \pm 0.0068	0.5360 \pm 0.0035
ISRUC_S3	Cohen’s Kappa	Weighted F1	Balanced Accuracy
$\alpha = 0.5$ (default)	0.7671 \pm 0.0091	0.8202 \pm 0.0071	0.7856 \pm 0.0031
$\alpha = 0.1$	0.7132 \pm 0.0646	0.7834 \pm 0.0523	0.7575 \pm 0.0621
$\alpha = 0.9$	0.6073 \pm 0.0230	0.6966 \pm 0.0176	0.6564 \pm 0.0058
$\alpha = 2.0$	0.5600 \pm 0.0492	0.6572 \pm 0.0430	0.6227 \pm 0.0427

2025

2026

2027

The decay parameter α controls how rapidly spatial kernel weights diminish with topological distance and, therefore, plays a central role in balancing locality preservation and kernel sparsification.

2028

2029

Across all datasets, $\alpha = 0.5$ consistently yields the highest performance. Larger values (e.g., $\alpha = 0.9$) moderately weaken spatial locality, while very small values (e.g., $\alpha = 0.1$) oversparsify the kernel and markedly reduce accuracy. Increasing α towards and beyond 1 (e.g., $\alpha = 2.0$) weakens the decay and assigns relatively larger weights to distant sub-kernels, which harms spatial locality and leads to clear performance drops, especially on ISRUC_S3. In addition, excessively large decay coefficients may amplify gradients during backpropagation and introduce training instability. For these reasons, we recommend α to ≤ 1 and adopt $\alpha = 0.5$ as a stable and well-performing default.

2030

2031

2032

2033

2034

2035

2036

2037

2038

K.6 ABLATION ON SUBBAND

2039

To better understand the frequency dependencies encoded by CODEBRAIN, we conduct a systematic subband ablation study by masking each of the five canonical EEG frequency ranges: δ (0.5–4 Hz), θ (4–8 Hz), α (8–13 Hz), β (13–30 Hz), and γ (>30 Hz). Unlike random dropout, this setting allows us to examine how the model allocates representational importance across physiologically meaningful frequency components. Experiments are performed on both the emotion recognition dataset (SEED-V) and the sleep-staging dataset (ISRUC_S3), covering two distinct neurophysiological tasks.

2040

2041

2042

2043

2044

2045

2046

2047

2048

2049

K.6.1 SEED-V (62 CHANNELS): SUBBAND CONTRIBUTIONS IN EMOTION RECOGNITION

Several key findings could be observed in this experiments:

2052

2053

Table 20: Subband ablation results on the SEED-V dataset.

2054

Removed Band	Cohen’s Kappa	Weighted F1	Balanced Accuracy
None	0.2735 \pm 0.0032	0.4235 \pm 0.0022	0.4137 \pm 0.0023
δ	0.0297 \pm 0.0027	0.2075 \pm 0.0105	0.2201 \pm 0.0004
θ	0.0142 \pm 0.0050	0.1780 \pm 0.0176	0.2098 \pm 0.0039
α	0.0082 \pm 0.0070	0.1306 \pm 0.0536	0.2058 \pm 0.0049
β	0.0442 \pm 0.0120	0.2377 \pm 0.0068	0.2360 \pm 0.0095
γ	0.1372 \pm 0.0081	0.3141 \pm 0.0086	0.3092 \pm 0.0044

2061

2062

- **Dominance of low-frequency structure.** Removing δ , θ , or α bands produces near-collapse of performance, indicating that emotional states are primarily encoded in slow and mid-range oscillations. This matches prior affective neuroscience findings showing that emotional arousal and valence strongly modulate rhythms below 13 Hz.
- **Residual robustness at higher frequencies.** Ablating β and especially γ reduces performance but does not catastrophically impair decoding. This suggests that CODEBRAIN leverages high-frequency activity as complementary contextual cues rather than primary discriminative features.
- **Contrast with raw-signal models.** Compared with prior end-to-end CNN/RNN models, the degradation patterns reveal that our decoupled tokenizer and cross-scale encoder preserve structured frequency dependencies rather than relying disproportionately on one frequency range.

2075

2076

These observations highlight that the learned frequency representation is aligned with known emotional knowledge while still maintaining robustness across a broad range of frequencies.

2077

2078

2079

2080

K.6.2 ISRUC_S3 (6 CHANNELS): SUBBAND CONTRIBUTIONS IN SLEEP STAGING

2081

2082

Table 21: Subband ablation results on the ISRUC_S3 dataset.

2083

Removed Band	Cohen’s Kappa	Weighted F1	Balanced Accuracy
None	0.7671 \pm 0.0091	0.8202 \pm 0.0071	0.7856 \pm 0.0031
δ	0.0225 \pm 0.0391	0.1751 \pm 0.0843	0.2043 \pm 0.0237
θ	0.0728 \pm 0.0557	0.1386 \pm 0.0341	0.2812 \pm 0.0749
α	0.1048 \pm 0.0221	0.1762 \pm 0.0186	0.3226 \pm 0.0293
β	0.2131 \pm 0.0660	0.2867 \pm 0.1185	0.3835 \pm 0.0446
γ	0.3618 \pm 0.0012	0.4831 \pm 0.0291	0.4764 \pm 0.0082

2090

2091

Results on ISRUC_S3 sleep staging dataset reveal a qualitatively different frequency profile from SEED-V:

2092

2093

- **Critical dependence on δ and θ .** Removing slow-wave components almost eliminates information, consistent with their central role in NREM transitions and slow oscillations during deep sleep.
- **Higher-frequency bands remain more robust.** Masking β and γ still reduces performance but to a lesser extent, reflecting the fact that spindle- or arousal-related faster bursts are less dominant in the 6-channel ISRUC montage.
- **Physiology-specific feature reliance.** The frequency sensitivity patterns differ from SEED-V, demonstrating that CODEBRAIN adapts its feature allocation depending on task demands rather than relying on a fixed frequency prior.

2094

2095

2096

2097

2098

2099

2100

2101

2102

2103

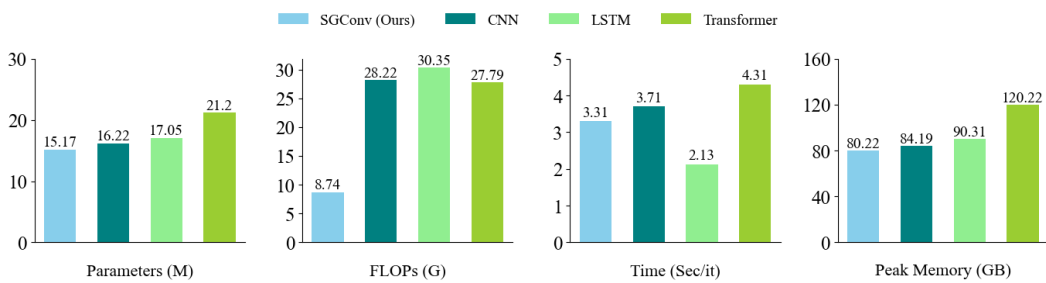
2104

2105

The subband ablation results across two very different datasets show that CODEBRAIN could capture frequency structure, leveraging low-frequency dynamics for both emotion and sleep tasks while maintaining robustness to higher-band perturbations.

2106 L BACKBONE EFFICIENCY COMPARISON

2108 To evaluate the computational efficiency of our proposed SGConv module, we conduct an ablation
 2109 study by replacing it with three common sequence modeling modules: CNN, LSTM, and Transformer
 2110 in EEGSSM block. We compare their model sizes, floating-point operations (FLOPs), and iteration
 2111 times, as shown in Figure 20. Specifically, the CNN variant uses a 3-layer depthwise separable
 2112 convolution block, while the LSTM and Transformer variants use a single layer of standard LSTM
 2113 and Transformer Encoder (implemented by Pytorch), respectively. In terms of parameter count,
 2114 SGConv contains 15.17M parameters, fewer than CNN (16.22M), LSTM (17.35M), and Transformer
 2115 (21.2M). For FLOPs, SGConv also achieves the lowest computational cost at 8.74G, compared to
 2116 Transformer’s 27.79G. Regarding iteration time, SGConv is slightly slower than Transformer and
 2117 CNN models in terms of training speed, but it outperforms the LSTM model. In summary, SGConv
 2118 effectively reduces the number of parameters while maintaining computational complexity, which
 2119 helps the model to be trained and inferred on smaller GPUs.



2130 Figure 20: Computational Overhead of Using Different Backbones in the EEGSSM Module.

2131
 2132 To further contextualize the computational efficiency of CODEBRAIN, we provide a comparison
 2133 against widely used EEG foundation-model baselines. Table 22 summarizes model parameters,
 2134 multiply-accumulate operations (MACs), and floating-point operations (FLOPs), offering stable
 2135 and hardware-agnostic metrics across architectures. Overall, CODEBRAIN achieves a favorable
 2136 balance between computational cost and representational capacity. Its FLOPs and MACs remain
 2137 substantially lower than large-scale models such as BENDR and EEGPT, while maintaining higher
 2138 parameter efficiency than CBraMod and LaBraM. Notably, CODEBRAIN occupies a middle ground
 2139 in model size—significantly smaller than EEGPT while offering richer representational power than
 2140 compact baselines like BIOT. This balanced compute–performance trade-off aligns with our design
 2141 goal of building an efficient yet high-capacity EEG foundation model suitable for both research and
 2142 deployment on modest hardware.

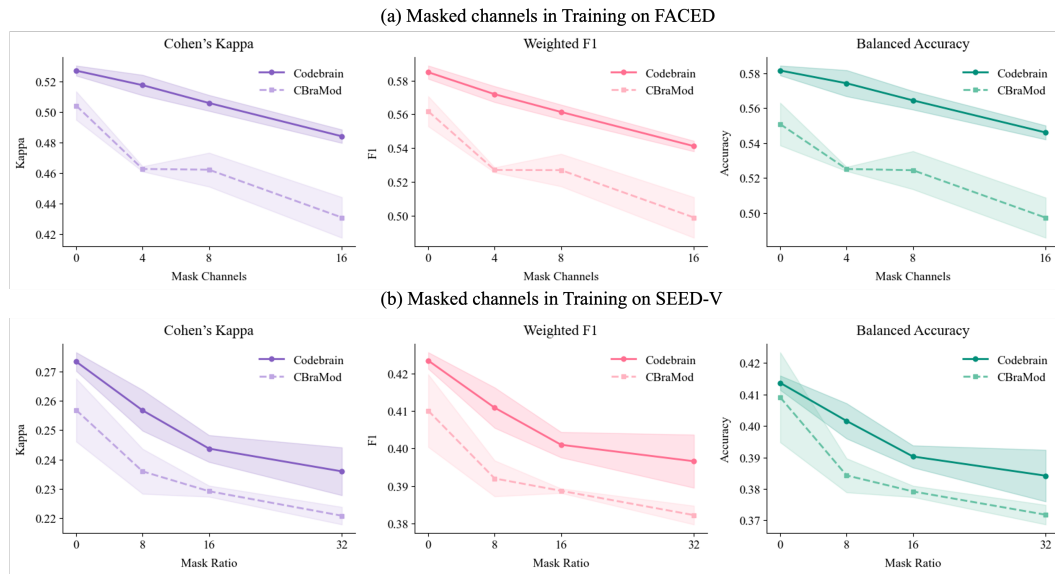
2143
 2144 Table 22: Compute comparison between CODEBRAIN and representative EEG foundation-model
 2145 baselines.

Model	MACs	Params	FLOPs
BENDR	12.51G	959.84M	25.02G
BIOT	0.255G	3.20M	0.510G
LaBraM	0.67G	6.02M	1.34G
CBraMod	0.64G	4.03M	1.29G
EEGPT	4.89G	25.24M	9.79G
CodeBrain	4.37G	15.17M	8.74G

2160 M MODEL ROBUSTNESS

2161 2162 2163 M.1 RANDOM CHANNEL DROPOUT

2164 In real-world scenarios, the collection of EEG often encounters situations where channels are missing,
 2165 especially when using machines from different manufacturers. To test the model's performance on
 2166 datasets with missing channel data, we randomly mask some channels in the training data for full
 2167 parameter fine-tuning. We selected the FACED and SEED-V datasets for experiments because they
 2168 represent short-sequence and long-sequence cases respectively, and their numbers of channels are
 2169 relatively complete.



2191 Figure 21: Performance after randomly masking different numbers of channels during the full
 2192 parameter fine-tuning stage.

2193 We evaluate the performance of the CodeBrain model and CBraMod model in scenarios with missing
 2194 channels. We conducted three different experiments, randomly masking 12.5%, 25%, and 50% of the
 2195 channels in each experiment, respectively. Figure 21 shows results of the experiment. It can be seen
 2196 that our CodeBrain model outperforms the CBraMod model in all channel masking scenarios. On the
 2197 FACED dataset, our model's performance after masking 25% of the channels is still close to that of
 2198 CBraMod without masking. The performance decline of the CBraMod model is also faster than that
 2199 of our model. This trend is even more pronounced on the SEED-V dataset. Through this experiment,
 2200 we can demonstrate that the channel robustness of CodeBrain is stronger than that of the CBraMod
 2201 model, retaining most of its performance even in cases of channel failure.

2202 2203 2204 2205 M.2 BRAIN-REGION CHANNEL DROPOUT

2206 While random channel masking simulates incidental electrode failures, it does not capture the struc-
 2207 tured spatial organization of the EEG montage. To provide a neuroscientifically meaningful robustness
 2208 evaluation, we conduct region-based masking on both the high-density SEED-V dataset (62 channels)
 2209 and the minimal-montage ISRUC_S3 dataset (6 channels). These experiments simulate clinically
 2210 relevant scenarios such as reference-electrode failures, lobe-specific dropout, and hemisphere-level
 2211 signal loss. We also compare CODEBRAIN with the strongest baseline, CBraMod.

2214
2215 **M.2.1 REGION-BASED ABLATIONS ON THE HIGH-DENSITY SEED-V DATASET (62**
2216 **CHANNELS)**

2217 We design nine anatomically meaningful masking patterns, including (1) reference/hemisphere fail-
2218 ures (midline-only, left-hemisphere masked, right-hemisphere masked), and (2) lobe-level dropout
2219 over occipital, frontal, temporal, central, frontocentral, and parietal regions. The results are summa-
2220 rized in Table 23.

2221
2222 **Table 23: Region-masking results on the SEED-V dataset (62 channels).**

2223

Mask Setting	Model	Cohen's Kappa	Weighted F1	Balanced Accuracy
Baseline (no mask)	CBraMod	0.2569 ± 0.0143	0.4101 ± 0.0108	0.4091 ± 0.0097
	CodeBrain(Ours)	0.2735 ± 0.0032	0.4235 ± 0.0022	0.4137 ± 0.0023
Only midline	CBraMod	0.0114 ± 0.0098	0.1740 ± 0.0121	0.2077 ± 0.0018
	CodeBrain(Ours)	0.0201 ± 0.0098	0.1610 ± 0.0087	0.2169 ± 0.0067
Left hemisphere	CBraMod	0.0672 ± 0.0260	0.2505 ± 0.0227	0.2541 ± 0.0226
	CodeBrain(Ours)	0.0956 ± 0.0030	0.2779 ± 0.0051	0.2750 ± 0.0030
Right hemisphere	CBraMod	0.0586 ± 0.0171	0.2500 ± 0.0214	0.2466 ± 0.0149
	CodeBrain(Ours)	0.0678 ± 0.0195	0.2540 ± 0.0066	0.2569 ± 0.0166
Occipital	CBraMod	0.1316 ± 0.0217	0.3066 ± 0.0167	0.3068 ± 0.0174
	CodeBrain(Ours)	0.2258 ± 0.0067	0.3851 ± 0.0040	0.3818 ± 0.0090
Frontal	CBraMod	0.0632 ± 0.0222	0.2486 ± 0.0177	0.2491 ± 0.0189
	CodeBrain(Ours)	0.1255 ± 0.0090	0.3025 ± 0.0080	0.2976 ± 0.0046
Temporal	CBraMod	0.1571 ± 0.0284	0.3309 ± 0.0222	0.3265 ± 0.0227
	CodeBrain(Ours)	0.2311 ± 0.0008	0.3922 ± 0.0010	0.3824 ± 0.0004
Central	CBraMod	0.1562 ± 0.0419	0.3305 ± 0.0336	0.3247 ± 0.0321
	CodeBrain(Ours)	0.2410 ± 0.0078	0.3997 ± 0.0067	0.3894 ± 0.0055
Frontocentral	CBraMod	0.1304 ± 0.0304	0.3077 ± 0.0263	0.3039 ± 0.0244
	CodeBrain(Ours)	0.1254 ± 0.0090	0.3025 ± 0.0080	0.2976 ± 0.0047
Parietal	CBraMod	0.1571 ± 0.0284	0.3309 ± 0.0222	0.3265 ± 0.0227
	CodeBrain(Ours)	0.2311 ± 0.0008	0.3922 ± 0.0010	0.3824 ± 0.0004

2248
2249 Across nearly all masking conditions, CODEBRAIN maintains stronger performance than CBraMod,
2250 particularly under lobe-level dropout (occipital, temporal, central), suggesting that its spatial-temporal
2251 modeling is less reliant on any single anatomical region. The severe degradation under midline-only
2252 signals further highlights the importance of distributed multi-lobe information in emotion-related
2253 EEG.

2254
2255
2256
2257 **M.2.2 REGION-BASED ABLATIONS ON THE MINIMAL-MONTAGE ISRUC_S3 DATASET (6**
2258 **CHANNELS)**

2259 To test robustness under extreme spatial sparsity, we perform structured region masking on the
2260 6-channel A1/A2-referenced ISRUC_S3 montage. We evaluate reference-electrode failures (masking
2261 A1 or A2) and lobe-specific removal (frontal, central, occipital). Results are shown in Table 24.

2262 Even under this sparse spatial setup, CODEBRAIN consistently maintains higher performance than
2263 CBraMod across all mask types. This indicates that the learned representations are robust to structured
2264 regional dropout and remain stable even when half or more channels are removed.

2265 Across both high-density and minimal-montage datasets, region-based ablation demonstrates that
2266 CODEBRAIN preserves strong predictive performance under structured channel dropout, highlighting
2267 its spatial robustness and reliable modeling of cross-regional EEG dependencies.

2268

2269

Table 24: Region-masking results on the ISRUC_S3 dataset (6 channels).

2270

2271

2272

2273

2274

2275

2276

2277

2278

2279

2280

2281

2282

2283

2284

2285

2286

2287

2288

M.3 NON-STATIONARY ROBUSTNESS

2289

EEG signals are inherently non-stationary, with gradual fluctuations caused by electrode impedance changes, autonomic modulation, motion artifacts, and slow drift in sensor baselines. To examine how well the learned representations tolerate such structured temporal drift, we introduce a simple but effective perturbation: a linear baseline shift. This perturbation exaggerates slow-varying non-stationarity beyond what naturally appears in the data, providing a controlled stress test of robustness. We evaluate both SEED-V (emotion recognition) and ISRUC_S3 (sleep staging), comparing CODEBRAIN with the strongest baseline, CBraMod. Results are summarized in Table ??.

2290

2291

2292

2293

2294

2295

2296

2297

2298

2299

Table 25: Non-stationary Robustness under linear baseline shift on SEED-V and ISRUC_S3.

2300

2301

2302

2303

2304

2305

2306

2307

2308

2309

2310

2311

2312

2313

2314

2315

2316

2317

2318

2319

2320

2321

SEED-V

Setting	Model	Cohen’s Kappa	Weighted F1	Balanced Accuracy
Reference (no shift)	CodeBrain	0.2735 \pm 0.0032	0.4235 \pm 0.0022	0.4137 \pm 0.0023
	CBraMod	0.2569 \pm 0.0143	0.4101 \pm 0.0108	0.4091 \pm 0.0097
Linear baseline shift	CodeBrain	0.2170 \pm 0.0345	0.3799 \pm 0.0276	0.3706 \pm 0.0259
	CBraMod	0.2027 \pm 0.0147	0.3658 \pm 0.0136	0.3628 \pm 0.0111

ISRUC_S3

Setting	Model	Cohen’s Kappa	Weighted F1	Balanced Accuracy
Reference (no shift)	CodeBrain	0.7671 \pm 0.0091	0.8202 \pm 0.0071	0.7856 \pm 0.0031
	CBraMod	0.7407 \pm 0.0251	0.8056 \pm 0.0219	0.7844 \pm 0.0126
Linear baseline shift	CodeBrain	0.4762 \pm 0.0835	0.5914 \pm 0.0668	0.5617 \pm 0.0630
	CBraMod	0.4242 \pm 0.0068	0.5478 \pm 0.0087	0.5268 \pm 0.0085

This controlled non-stationarity stress test reveals several consistent patterns. Moderate linear drift introduces clear performance degradation across both datasets, as expected for models trained under largely stationary conditions. The effect is especially pronounced on ISRUC_S3, where the limited channel count amplifies the impact of baseline shifts. Despite this, CODEBRAIN retains a larger proportion of its original performance than CBraMod, suggesting that its decoupled time-frequency tokenizer and multi-scale encoder yield more stable representations under slow global waveform drift. We also observe task-dependent differences in sensitivity: emotion recognition is disproportionately affected in low-frequency components, whereas sleep staging exhibits a more uniform degradation across metrics, reflecting the different spectral structures these tasks rely on. Overall, the results

2322 indicate that CODEBRAIN maintains stronger robustness to non-stationary perturbations, making it
2323 suitable for real-world settings where gradual baseline drift and electrode instability are unavoidable.
2324

2325 N DETAILED RESULTS ON SCALING LAWS

2326 We provide the detailed scaling law results for both data and model size across three representative
2327 EEG datasets (FACED, SEED-V, and ISRUC_S3), covering three evaluation metrics. For brevity,
2328 only Cohen’s kappa scores are included in the main text, while full results are provided in this section.
2329 Prior work (Wang et al., 2025; Jiang et al., 2024) has explored the effect of scaling EEG foundation
2330 models using 1 to 1000 hours of pretraining data. We extend this analysis in two key dimensions:
2331

- 2333 1. Scaling the pretraining data volume from 1k up to 9k hours.
- 2334 2. Investigating model scaling by varying the depth of the EEGSSM encoder from 3 layers
2335 (3.86M parameters) to 24 layers (146.75M parameters) and the hidden size from 128 to 384.

2336 N.1 SCALING LAWS WITH RESPECT TO TRAINING DATA VOLUME

2337 We examine how the volume of pretraining data influences the downstream performance of CODE-
2338 BRAIN. Specifically, we scale the pretraining duration from 1k to 9k hours and evaluate the resulting
2339 models on three downstream datasets: FACED, SEED-V, and ISRUC_S3. Detailed quantitative
2340 results across three evaluation metrics (Cohen’s kappa, weighted F1 score, and balanced accuracy)
2341 are presented in Tables 26, 27, and 28, respectively. As shown in Figure 22, increasing the amount
2342 of pretraining data generally leads to consistent improvements across all datasets and metrics. On
2343 FACED and ISRUC_S3, performance gains are steady throughout the entire range up to 9k hours,
2344 while on SEED-V, the trend is more modest and plateaus after 5k hours. These results highlight the
2345 importance of large-scale data for representation learning in EEG and suggest that further scaling
2346 may continue to yield performance benefits.
2347

2348
2349
2350 Table 26: Training Data Scaling Laws of CODEBRAIN on FACED Dataset.

2351 Training Data	2352 Cohen’s Kappa	2353 Weighted F1	2354 Balanced Accuracy
2353 1000 Hours	2354 0.5014 ± 0.0107	2355 0.5462 ± 0.0146	2356 0.5452 ± 0.0163
2354 2000 Hours	2355 0.5133 ± 0.0068	2356 0.5540 ± 0.0120	2357 0.5521 ± 0.0133
2355 3000 Hours	2356 0.5189 ± 0.0086	2357 0.5688 ± 0.0104	2358 0.5687 ± 0.0083
2356 4000 Hours	2357 0.5208 ± 0.0032	2358 0.5741 ± 0.0041	2359 0.5713 ± 0.0024
2357 5000 Hours	2358 0.5171 ± 0.0040	2359 0.5692 ± 0.0131	2360 0.5661 ± 0.0105
2358 6000 Hours	2359 0.5273 ± 0.0085	2360 0.5803 ± 0.0064	2361 0.5764 ± 0.0069
2359 7000 Hours	2360 0.5328 ± 0.0116	2361 0.5854 ± 0.0082	2362 0.5809 ± 0.0097
2360 8000 Hours	2361 0.5336 ± 0.0082	2362 0.5875 ± 0.0071	2363 0.5835 ± 0.0072
2361 9000 Hours	2362 0.5406 ± 0.0084	2363 0.5953 ± 0.0113	2364 0.5941 ± 0.0098

2365 In addition, we visualize the pretraining optimization behavior across different data scales in Figure 23.
2366 As expected, larger pretraining data consistently lead to lower training loss, indicating more effective
2367 representation learning. Notably, the convergence curves become progressively smoother and more
2368 stable as training data volume increases, suggesting improved optimization stability in large-scale
2369 regimes. While smaller training data volumes (e.g., 1k–3k hours) show relatively high starting
2370 loss and slower convergence, larger training data volumes (6k–9k hours) reach lower final losses
2371 and exhibit diminishing returns, aligning with trends observed in downstream performance. These
2372 findings provide further empirical support for the scalability of EEG foundation models and reinforce
2373 the role of large data in enhancing both optimization and generalization.

2374 N.2 SCALING LAWS WITH RESPECT TO MODEL SIZE

2375 We further investigate how model parameters affect downstream performance by scaling the number
2376 of layers in the EEGSSM encoder from 3 to 8, resulting in parameter counts ranging from 6.82M
2377 to 15.17M. Detailed results across the FACED, SEED-V, and ISRUC_S3 datasets are provided in

2376

2377

Table 27: Training Data Scaling Laws of CODEBRAIN on SEED-V Dataset.

2378

2379

Training Data	Cohen's Kappa	Weighted F1	Balanced Accuracy
1000 Hours	0.2584 ± 0.0044	0.3946 ± 0.0063	0.3799 ± 0.0096
2000 Hours	0.2648 ± 0.0062	0.4042 ± 0.0091	0.3961 ± 0.0084
3000 Hours	0.2689 ± 0.0055	0.4117 ± 0.0075	0.4028 ± 0.0082
4000 Hours	0.2672 ± 0.0043	0.4121 ± 0.0054	0.4022 ± 0.0049
5000 Hours	0.2678 ± 0.0069	0.4120 ± 0.0084	0.4026 ± 0.0067
6000 Hours	0.2669 ± 0.0031	0.4113 ± 0.0067	0.4030 ± 0.0102
7000 Hours	0.2686 ± 0.0043	0.4129 ± 0.0052	0.4027 ± 0.0048
8000 Hours	0.2703 ± 0.0049	0.4165 ± 0.0034	0.4094 ± 0.0054
9000 Hours	0.2735 ± 0.0032	0.4235 ± 0.0022	0.4137 ± 0.0023

2380

2381

2382

2383

2384

2385

2386

2387

2388

2389

2390

2391

2392

Table 28: Training Data Scaling Laws of CODEBRAIN on the ISRUC_S3 Dataset.

2393

Training Data	Cohen's Kappa	Weighted F1	Balanced Accuracy
1000 Hours	0.7340 ± 0.0187	0.7826 ± 0.0154	0.7505 ± 0.0192
2000 Hours	0.7347 ± 0.0051	0.7869 ± 0.0075	0.7524 ± 0.0032
3000 Hours	0.7540 ± 0.0106	0.8012 ± 0.0093	0.7694 ± 0.0089
4000 Hours	0.7590 ± 0.0042	0.8108 ± 0.0074	0.7753 ± 0.0065
5000 Hours	0.7610 ± 0.0058	0.8124 ± 0.0102	0.7794 ± 0.0086
6000 Hours	0.7681 ± 0.0125	0.8190 ± 0.0100	0.7856 ± 0.0089
7000 Hours	0.7648 ± 0.0079	0.8170 ± 0.0076	0.7845 ± 0.0076
8000 Hours	0.7668 ± 0.0121	0.8182 ± 0.0109	0.7851 ± 0.0116
9000 Hours	0.7671 ± 0.0091	0.8202 ± 0.0071	0.7856 ± 0.0031

2404

2405

Tables 29, 30, and 31, respectively. To visualize the trend more clearly, Figure 24 presents the performance curves as model size increases. Across all three datasets and evaluation metrics, we observe a consistent performance gain as the model size increases. The improvements are particularly pronounced on the FACED and ISRUC_S3 datasets, where all three metrics show steady growth up to the largest model. In contrast, performance on SEED-V improves more modestly and begins to plateau beyond 13.5M parameters. These results suggest that increasing model capacity can enhance generalization ability, especially for datasets with richer structure or more complex temporal dynamics, while also indicating that optimal scaling may be task-dependent.

2413

2414

2415

Table 29: Model Size Scaling Laws of CODEBRAIN on the FACED Dataset.

2416

2417

Layer	Hidden size	Params	Cohen's Kappa	Weighted F1	Balanced Accuracy
3	128	3.86M	0.4786 ± 0.0131	0.5231 ± 0.0164	0.5287 ± 0.0207
3	200	6.82M	0.4818 ± 0.0165	0.5362 ± 0.0113	0.5317 ± 0.0182
4	200	8.49M	0.4988 ± 0.0082	0.5506 ± 0.0091	0.5497 ± 0.0084
5	200	10.16M	0.5096 ± 0.0049	0.5686 ± 0.0104	0.5642 ± 0.0067
6	200	11.83M	0.5244 ± 0.0113	0.5705 ± 0.0085	0.5778 ± 0.0095
7	200	13.50M	0.5314 ± 0.0069	0.5872 ± 0.0080	0.5846 ± 0.0067
8	200	15.17M	0.5406 ± 0.0084	0.5953 ± 0.0113	0.5941 ± 0.0098
12	256	33.15M	0.5478 ± 0.0013	0.5912 ± 0.0031	0.5901 ± 0.0128
24	384	146.75M	0.5503 ± 0.0120	0.5964 ± 0.0178	0.5985 ± 0.0233

2428

2429

To better understand the optimization behavior during pretraining, we plot the training loss curves for different model sizes in Figure 25. As expected, larger models consistently achieve lower final

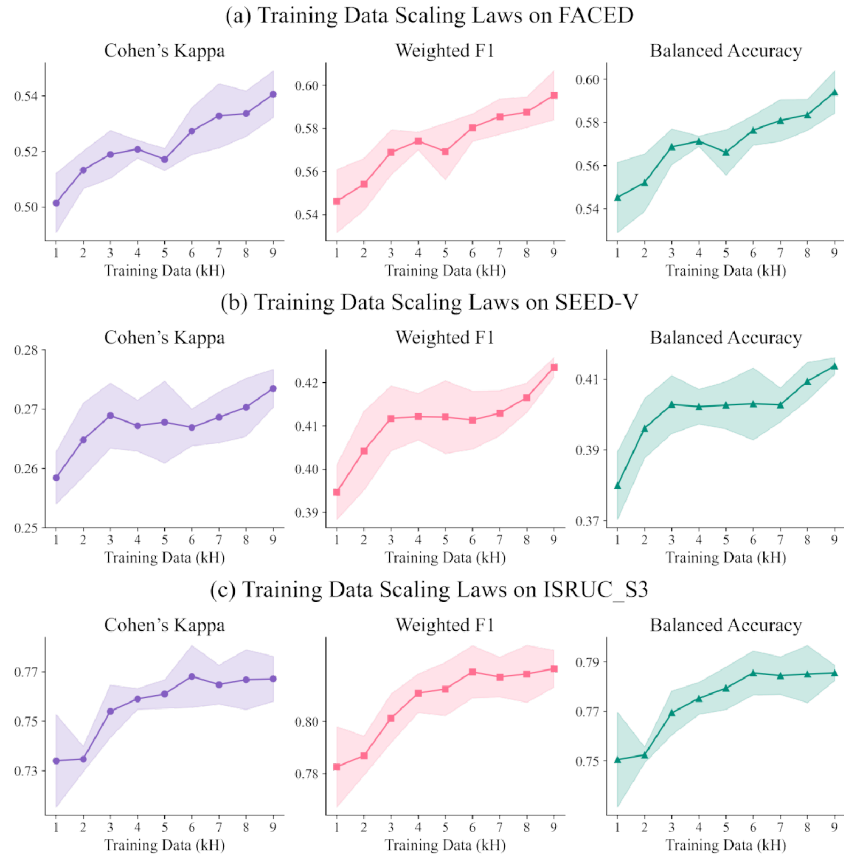


Figure 22: Training Data Scaling Laws on FACED, SEED-V, and ISRUC_S3.

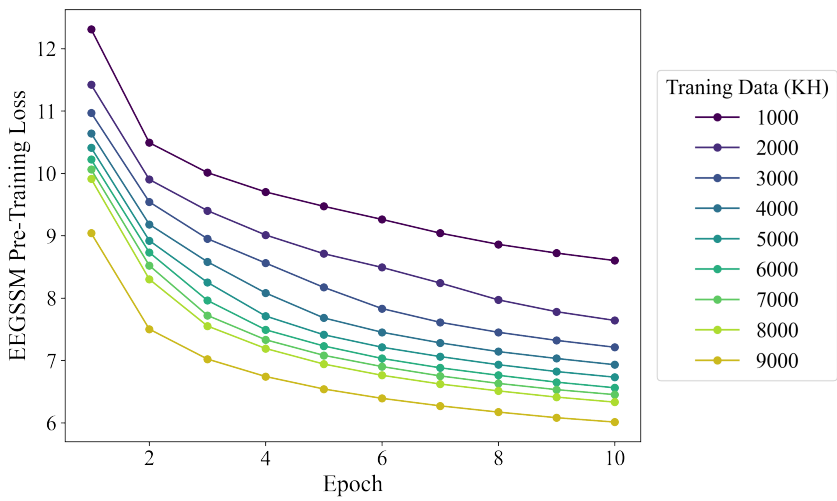


Figure 23: EEGSSM Pre-Training Loss Curve for Different Training Data Volume.

2480 training loss, indicating stronger capacity to fit the pretraining objective. The loss reduction is
 2481 particularly evident when increasing from 3 to 6 layers, while the gain starts to saturate beyond 7
 2482 layers. Even when increased to 24 layers, the reduction in pre-training loss brought by more than
 2483 100M parameters is not significant. This trend mirrors the downstream performance in Figure 24 and
 Tables 29–31, suggesting that both optimization efficiency and generalization benefit from increased

2484

2485

Table 30: Model Size Scaling Laws of CODEBRAIN on the SEED-V Dataset.

2486

2487

Layer	Hidden size	Params	Cohen’s Kappa	Weighted F1	Balanced Accuracy
3	128	3.86M	0.2576±0.0047	0.3969±0.0042	0.3896±0.0027
3	200	6.82M	0.2609±0.0078	0.4004±0.0112	0.3956±0.0098
4	200	8.49M	0.2638±0.0080	0.4108±0.0091	0.4030±0.0121
5	200	10.16M	0.2645±0.0102	0.4127±0.0158	0.4013±0.0084
6	200	11.83M	0.2663±0.0056	0.4202±0.0068	0.4079±0.0055
7	200	13.50M	0.2724±0.0057	0.4211±0.0060	0.4120±0.0086
8	200	15.17M	0.2735±0.0032	0.4235±0.0022	0.4137±0.0023
12	256	33.15M	0.2807±0.0029	0.4317±0.0036	0.4182±0.0028
24	384	146.75M	0.2831±0.0033	0.4342±0.0030	0.4216±0.0031

2498

2499

2500

Table 31: Model Size Scaling Laws of CODEBRAIN on the ISRUC_S3 Dataset.

2501

Layer	Hidden size	Params(M)	Cohen’s Kappa	Weighted F1	Balanced Accuracy
3	128	3.86M	0.7434±0.0087	0.7813±0.0107	0.7493±0.0058
3	200	6.82M	0.7456±0.0083	0.7862±0.0104	0.7514±0.0084
4	200	8.49M	0.7486±0.0014	0.7942±0.0040	0.7604±0.0035
5	200	10.16M	0.7516±0.0025	0.7985±0.0056	0.7639±0.0079
6	200	11.83M	0.7570±0.0082	0.8064±0.0068	0.7734±0.0061
7	200	13.50M	0.7620±0.0045	0.8153±0.0091	0.7824±0.0100
8	200	15.17M	0.7671±0.0091	0.8202±0.0071	0.7856±0.0031
12	256	33.15M	0.7753±0.0113	0.8316±0.0074	0.7940±0.0061
24	384	146.75M	0.7791±0.0108	0.8352±0.0072	0.8008±0.0040

2512

2513

model size—though with diminishing returns as parameter count grows. These results reinforce the scalability of EEGSSM and underscore the importance of balancing capacity with task-specific requirements.

2514

2515

Our results demonstrate consistent improvements in downstream performance as both data volume and model capacity increase, suggesting that EEG foundation models may continue to benefit from further scaling, similar to trends observed in vision and language domains.

2516

2517

2518

2519 N.3 COMPUTATIONAL ANALYSIS ACROSS SCALES.

2520

2521

2522

2523 Complementing the scaling analyses on model size and data size presented in the previous subsections, we further examine how computational cost scales with architectural capacity. This provides a detailed breakdown of parameters, FLOPs, throughput, and GPU memory usage across all CodeBrain model configurations, allowing a holistic view of the efficiency capacity.

2524

2525

2526

2527

2528

2529 Table 32 shows a smooth increase in parameters, FLOPs, and memory consumption as model depth 2530 and hidden size grow. Notably, throughput decreases sub-linearly with scale, demonstrating that the 2531 architecture maintains high computational efficiency even at larger capacities.

2532

2533

2534

2535

2536

2537

2538 Lightweight variants (3-6 layers) offer high throughput (3.5-5 samples/s) and low memory usage 2539 (< 8 GB), suitable for real-time or resource-constrained EEG applications. Mid-sized models (8-12 2540 layers) provide an excellent balance between performance and efficiency, which aligns with where 2541 the accuracy scaling curve begins to saturate. The largest configuration (24 layers, 146M parameters) 2542 substantially increases capacity and FLOPs, corresponding to the upper regime of diminishing returns 2543 observed in the model-size scaling law. We therefore select the 8-layer configuration as the main 2544 model used in our experiments after balancing performance and efficiency.

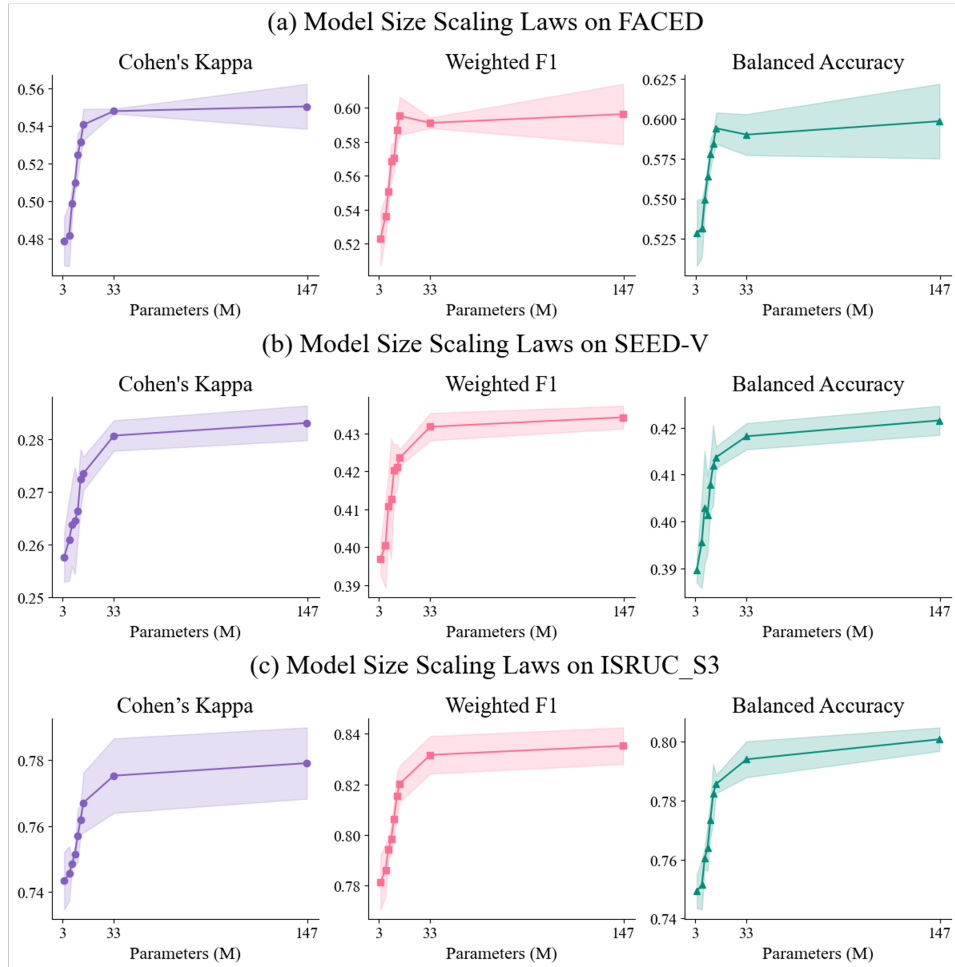


Figure 24: Model Size Scaling Laws on FACED, SEED-V, and ISRUC_S3.

Table 32: Computational analysis across different model scales..

Layer	Hidden Size	Params	FLOPs	Throughput	GPU Memory
3	128	3.96M	1.7G	4.90	4.87
3	200	6.82M	3.35G	4.62	5.63
4	200	8.49M	4.43G	3.77	6.48
5	200	10.16M	5.51G	3.67	7.33
6	200	11.83M	6.58G	3.52	8.10
7	200	13.50M	7.66G	2.94	8.95
8	200	15.17M	8.74G	2.78	9.79
12	256	34.38M	19.04G	1.84	15.41
24	384	146.75M	72.99G	1.47	38.43

Overall, these results show that CodeBrain follows predictable computational scaling behavior and offers flexible operating points for various deployment budgets.

2592
2593
2594
2595
2596
2597
2598
2599
2600
2601
2602
2603
2604
2605
2606
2607
2608
2609
2610
2611
2612
2613
2614
2615
2616
2617
2618
2619
2620
2621
2622
2623
2624
2625
2626
2627
2628
2629
2630
2631
2632
2633
2634
2635
2636
2637
2638
2639
2640
2641
2642
2643
2644
2645

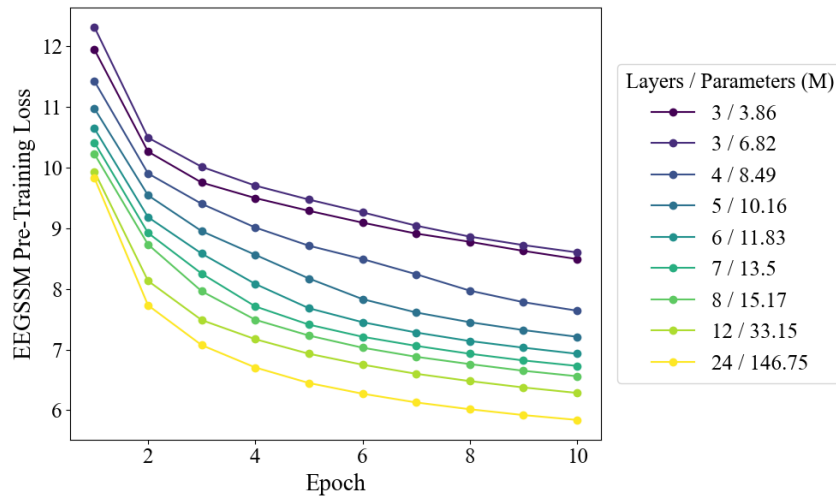


Figure 25: EEGSSM Pre-Training Loss Curve for Different Model Size.

2646 O LOW-RESOURCE COMPARISON WITH EXISTING METHODS

2649 Table 33: Comparison under data-limited settings on the FACED dataset (9-class).

2651 Methods	2652 Cohen’s Kappa	2653 Weighted F1	2654 Balanced Accuracy
<i>2655 Linear Probing</i>			
2656 LaBraM (lp)	0.3026 ± 0.0121	0.3789 ± 0.0154	0.3812 ± 0.0148
2657 CBraMod (lp)	0.3378 ± 0.0139	0.4123 ± 0.0117	0.4146 ± 0.0123
2658 CodeBrain (lp)	0.3587 ± 0.0136	0.4311 ± 0.0109	0.4327 ± 0.0127
<i>2659 10% Few-Shot</i>			
2660 LaBraM (10%)	0.1358 ± 0.0163	0.2247 ± 0.0196	0.2265 ± 0.0174
2661 CBraMod (10%)	0.1632 ± 0.0156	0.2595 ± 0.0138	0.2604 ± 0.0148
2662 CodeBrain (10%)	0.1716 ± 0.0101	0.2599 ± 0.0104	0.2654 ± 0.0093
<i>2663 30% Few-Shot</i>			
2664 BIOT (30%)	0.2573 ± 0.0346	0.3501 ± 0.0341	0.3428 ± 0.0329
2665 LaBraM (30%)	0.2672 ± 0.0371	0.3548 ± 0.0325	0.3513 ± 0.0315
2666 CBraMod (30%)	0.3239 ± 0.0265	0.4056 ± 0.0256	0.4035 ± 0.0233
2667 CodeBrain (30%)	0.3356 ± 0.0253	0.4114 ± 0.0225	0.4104 ± 0.0281
<i>2668 BIOT (full)</i>			
2669 LaBraM (full)	0.4476 ± 0.0254	0.5136 ± 0.0112	0.5118 ± 0.0118
2670 CBraMod (full)	0.4698 ± 0.0102	0.5288 ± 0.0188	0.5273 ± 0.0107
2671 CodeBrain (full)	0.5041 ± 0.0122	0.5618 ± 0.0093	0.5509 ± 0.0089
2672	0.5406 ± 0.0084	0.5953 ± 0.0113	0.5941 ± 0.0098

2673 Table 34: Comparison under data-limited settings on the SEED-V dataset (5-class).

2676 Methods	2677 Cohen’s Kappa	2678 Weighted F1	2679 Balanced Accuracy
<i>2680 Linear Probing</i>			
2681 LaBraM (lp)	0.1941 ± 0.0184	0.3457 ± 0.0135	0.3413 ± 0.0144
2682 CBraMod (lp)	0.2239 ± 0.0053	0.3823 ± 0.0041	0.3791 ± 0.0050
2683 CodeBrain (lp)	0.2302 ± 0.0166	0.3889 ± 0.0154	0.3829 ± 0.0136
<i>2684 10% Few-Shot</i>			
2685 LaBraM (10%)	0.0302 ± 0.0065	0.2194 ± 0.0079	0.2228 ± 0.0091
2686 CBraMod (10%)	0.0174 ± 0.0029	0.2071 ± 0.0125	0.2127 ± 0.0023
2687 CodeBrain (10%)	0.1690 ± 0.0170	0.3410 ± 0.0133	0.3331 ± 0.0138
<i>2688 30% Few-Shot</i>			
2689 BIOT (30%)	0.1775 ± 0.0425	0.3492 ± 0.0416	0.3505 ± 0.0375
2690 LaBraM (30%)	0.2044 ± 0.0384	0.3700 ± 0.0321	0.3686 ± 0.0305
2691 CBraMod (30%)	0.2291 ± 0.0246	0.3886 ± 0.0255	0.3877 ± 0.0236
2692 CodeBrain (30%)	0.2376 ± 0.0284	0.3943 ± 0.0259	0.3902 ± 0.0271
<i>2693 BIOT (full)</i>			
2694 LaBraM (full)	0.2261 ± 0.0262	0.3856 ± 0.0203	0.3837 ± 0.0187
2695 CBraMod (full)	0.2386 ± 0.0209	0.3974 ± 0.0111	0.3976 ± 0.0138
2696 CodeBrain (full)	0.2569 ± 0.0143	0.4101 ± 0.0108	0.4091 ± 0.0097
2697	0.2735 ± 0.0032	0.4235 ± 0.0022	0.4137 ± 0.0023

2698 To evaluate model performance under constrained conditions, we examine three transfer settings:
2699 30% few-shot, 10% few-shot, and linear probing. The 30% and 10% settings reflect data-limited

2700 conditions, where only a small portion of labeled target data is available for adaptation. In contrast,
2701 linear probing represents a compute-limited condition where the backbone is frozen, and only a
2702 single linear layer is trained. Results for both the FACED (9-class) and SEED-V (5-class) datasets
2703 are reported in Tables 33 and 34.

2704 Across all three settings and both datasets, CodeBrain consistently achieves the best performance
2705 among the evaluated methods, demonstrating stronger data efficiency and reliable transfer behavior
2706 under limited supervision. We also observe that few-shot performance is generally lower than linear
2707 probing, which is expected because full fine-tuning with very limited labeled data tends to be more
2708 sensitive to overfitting and distribution shift, whereas linear probing offers a more stable evaluation
2709 by freezing the backbone and relying only on the pretrained representations. This also confirms that
2710 the pretrained representations learned by CodeBrain already contain meaningful structure. Full-data
2711 results are also included for reference.

2712 While CodeBrain remains superior to prior EFM s in all limited-data and compute-limited conditions,
2713 all models exhibit notable performance drops compared to full fine-tuning, which is expected. EEG
2714 signals inherently exhibit extremely low signal-to-noise ratios and substantial domain shift across
2715 subjects, devices, montages, and recording setups. Under such conditions, a small number of labeled
2716 samples is often insufficient to fully adapt pretrained representations to the target distribution, making
2717 low-resource EEG transfer a challenging but important research problem. Systematic evaluations in
2718 these settings (both few-shot and linear probing) therefore remain underexplored in the literature, and
2719 our study provides an initial step toward addressing this gap.

2720 2721 2722 P LIMITATIONS AND FUTURE WORK

2723 Our work presents promising results but also highlights several limitations that offer directions for
2724 future exploration.

2725 First, the interpretability analyses in this paper focus on *representation-level* structure learned during
2726 pretraining. As this paper centers on developing a foundation model, our focus is mainly placed on
2727 understanding the representation space learned during pretraining. Future work may incorporate
2728 *decision-level* interpretability during finetuning, for example by exploring sparse codebook selection,
2729 task-guided gating mechanisms, or disentangling how temporal and frequency codes contribute to
2730 class-specific predictions.

2731 Second, our model and experiments focus on only *scalp EEG* data. Extending the proposed framework
2732 to modalities with richer frequency content, such as intracranial EEG (iEEG), electrocorticography
2733 (ECoG), or stereo-EEG (sEEG), offers an opportunity to study how the model behaves under
2734 substantially different signal characteristics.

2735 These directions offer promising directions toward building more general and more interpretable
2736 brain foundation models that operate across signal modalities and provide both meaningful insights.

2737 Q CODE ACCESS

2738 The code has been made publicly available via an anonymous GitHub repository:
2739 <https://anonymous.4open.science/r/CodeBrain-D7E6>

2740 R USE OF LLM

2741 In preparing this manuscript, we made use of large language models (LLMs) such as ChatGPT,
2742 Gemini, and Deepseek for auxiliary writing support. Specifically, LLMs were employed in three
2743 ways:

2744 (i) Polishing the English writing style, including grammar correction and improving fluency;
2745 (ii) Assisting with LaTeX formatting and typesetting to ensure consistent presentation of mathematical
2746 equations, tables, and figures.

2754 All core technical content, theoretical results, and experimental findings were designed, implemented,
2755 and validated by the authors. LLM usage was restricted to language refinement and formatting
2756 assistance, without influencing the originality or validity of the scientific contributions.
2757

2758

2759

2760

2761

2762

2763

2764

2765

2766

2767

2768

2769

2770

2771

2772

2773

2774

2775

2776

2777

2778

2779

2780

2781

2782

2783

2784

2785

2786

2787

2788

2789

2790

2791

2792

2793

2794

2795

2796

2797

2798

2799

2800

2801

2802

2803

2804

2805

2806

2807